ISSN 2708-6437(Online)
2708-6429(Print)

Journal of Engineering Advancements

Editor-in-Chief:
Prof. Dr. Mohammad Mashud

Volume 03 Issue 03

SciEn

Published by:
SciEn Publishing Group

Journal of Engineering Advancements
Apt. # 6 C-D, House # 191
Road # 12/A, Dhanmondi R/A
Dhaka-1209, Bangladesh
Email: jea@scienpg.com Website: www.scienpg.com/jea/

SciEn
Published in: September 2022
Published by: SciEn Publishing Group
Price: Each Issue BDT 200.00 (US$ 15) **ISSN:** 2708-6437 (Online) 2708-6429 (Print)

Journal of Engineering Advancements
Apt. # 6 C-D, House # 191
Road # 12/A, Dhanmondi R/A
Dhaka-1209, Bangladesh
Email: jea@scienpg.com Website: www.scienpg.com/jea/

SciEn
Published in: September 2022
Published by: SciEn Publishing Group
Price: Each Issue BDT 200.00 (US$ 15) **ISSN:** 2708-6437 (Online) 2708-6429 (Print)

Journal of Engineering Advancements

Volume 03, Issue 03 September 2022

CONTENTS

Original Articles

Journal of Engineering Advancements

Published by: SciEn Publishing Group

Apt. # 6 C-D, House # 191, Road # 12/A
Dhanmondi, Dhaka-1209, Bangladesh
Email Address: jea@scienpg.com

www.scienpg.com/jea/

This page is left intentionally blank

SciEn
Journal of Engineering Advancements Vol. 03(03) 2022, pp 72-75 https://doi.org/10.38032/jea.2022.03.001

The Design of a Superstate NZIM-Antenna Array for WLAN Application

A. Khairy[1], Islam Mohammed[1], Mohamed I. Ahmed[2] and M. M. Elsherbini[1,3,]*

[1]Department of Electrical Engineering, The Egyptian Academy for Engineering and Advanced Technology (EAEAT), Egypt
[2]Department of Microstrip, Electronic Research Institute, Egypt
[3]Shoubra Faculty of Engineering, Benha University, Egypt

Received: May 28, 2022, Revised: July 07, 2022, Accepted: July 14, 2022, Available Online: August 10, 2022

ABSTRACT

With the development of telecommunications and its applications, the design of compact antennas with high performance has become a great necessity. Among the important requirements is a high gain. In this article, a microstrip patch antenna using near zero-index metamaterial (NZIM) is proposed. This prototype is designed with the designing parameters of a rectangular microstrip patch antenna. The substrate material is FR-4. Simulation results show that this antenna operates at 5.8 GHz for a wireless local area network (WLAN). The proposed single antenna element achieves side-lobe suppression better than -13 dB. The 4×4 proposed antenna array is designed using 16 single elements and a T-shaped power divider to split power for each element. By covering a single-layer NZIM coating with a 4×4 array over a microstrip antenna, a gain enhancement of 14 dB is achieved in comparison with the single element. Over the operating band, the antenna prototype demonstrates steady radiation patterns. These characteristics are in good agreement with the simulations, rendering the antenna a good candidate for 5G applications. These antennas are designed, optimized, and simulated using CSTMWS2020.

Keywords: Antenna Array, Microstrip Antenna, CST, NZIM, Gain, Side Lobes Level.

1 Introduction

Microstrip or patch antennas are becoming increasingly useful because they can be printed directly onto a circuit board and have a low profile and low cost. High speed, broadband, and high capacity in or outside WLANs are becoming increasingly common nowadays, so it's worth getting acquainted with some of the difficulties of wireless design that must be addressed and overcome. Because of their advantages, microstrip antennas are an excellent choice for wireless local area network (WLAN) applications [1]. Despite these drawbacks, like a lower gain, narrow bandwidth, and large ohmic losses in the feed structure of arrays. The microstrip patch antennas can be adapted for use in new high-speed broadband WLAN systems as well as other applications like PCS, Bluetooth, RFID, and so on. The purpose of this paper is to use a near-zero-index metamaterial as a single- or double-layer superstrate hung above a microstrip patch antenna operating at 5.8 GHz for gain enhancement. The metamaterial layer superstrate is composed of a periodic arrangement of Jerusalem cross-unit cells and has the properties of a homogeneous medium with a refractive index close to zero [2]-[4]. This metamaterial characteristic enables the collection of radiated waves from the antenna and collimates them in the direction of the superstrate normal [5]. Many metamaterial-based patch antennas have been built and thoroughly explored in recent years. Moreover, near zero-index of refraction metamaterials have been widely studied to enhance antenna performance [6]. Due to their ability to control the radiation pattern and the convergence energy, near-zero-index metamaterials can be used to improve the gains of the antennas.

2 Antenna Design

The single element of the antenna is designed using an FR4 substrate with a relative permittivity of 4.3 and a thickness of 1.57 mm to operate at 5.8 GHz, achieving -10 dB, 300 MHz bandwidth. The single element has an overall realized gain of 3.58 dB. A single layer NZIM with 43 cells is covered over a microstrip antenna at a height of 4.62 mm operating at 5.8 GHz with broadband characteristics to improve its performance. As a result, a gain enhancement of 14 dB is achieved for the antenna.

2.1 Antenna Structure

A microstrip antenna is an antenna that is primarily a two-dimensional flat structure, as shown in Fig. 1. In its most basic form, it employs a one-half wavelength long conducting "patch," with the metal surface acting as a resonator, similar to half-wave dipole antennas. It is frequently constructed simply by mounting or constructing an appropriately dimensioned metal sheet or surface on an insulating dielectric substrate, such as a printed circuit board. The opposite side of the PC board substrate is also cladded and so forms a ground plane, or another conductive surface is added on the other side of the dielectric [7]. The dimensions of the rectangular microstrip patch antenna are shown in Table 1. The substrate material is FR-4 with a relative permittivity of 4.3 and a thickness of 1.6 mm. The following equations are used for microstrip antenna design [8].

$$w = \frac{c}{2f_r}\sqrt{\frac{2}{\varepsilon_r + 1}} \tag{1}$$

$$\varepsilon_{r_{eff}} = \frac{\varepsilon_r + 1}{2} + \frac{\varepsilon_r - 1}{2}\left(1 + 12\frac{h}{w}\right)^{\frac{-1}{2}} \tag{2}$$

$$\Delta L = 0.412h\frac{(\varepsilon_{r_{eff}} + 0.3)(\frac{w}{h} + 0.264)}{(\varepsilon_{r_{eff}} - 0.258)(\frac{w}{h} + 0.8)} \tag{3}$$

*Corresponding Author Email Address: m.moustafa@eaeat-academy.edu.eg Published by: SciEn Publishing Group

$$Re = \frac{\rho V d}{\mu} \quad (4)$$

$$L = \frac{c}{2f_r\sqrt{\varepsilon_{r_{eff}}}} - 2\Delta L \quad (5)$$

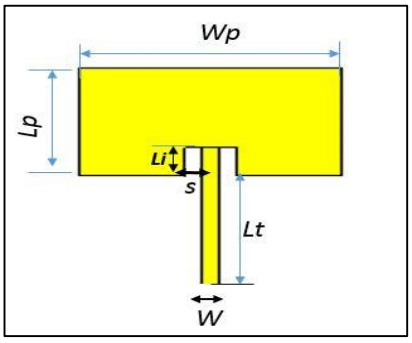

Fig. 1 Microstrip Structure.

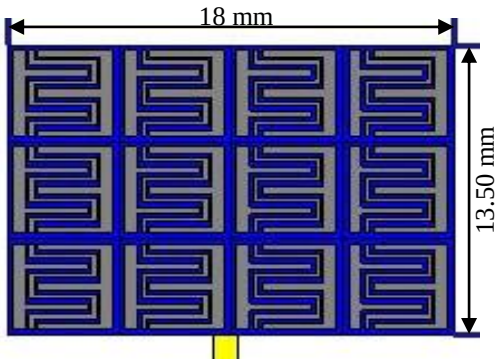

(a)

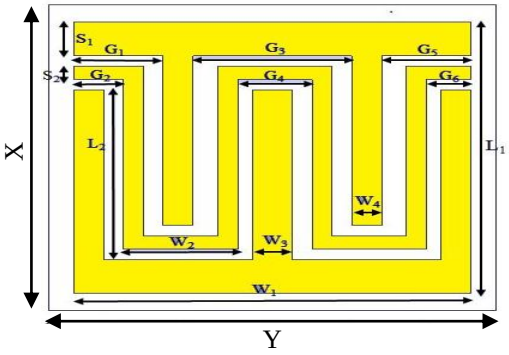

(b)

Fig. 2 NZIM Structure. (a) The geometry of unit cell (b) The schematic diagram of NZIM unit cell.

Table 1 Microstrip Antenna Parameters.

Parameter	Value
Lp	15
Wp	15
Wf	3
Lt	17
S	1

2.2 NZIM Unit Cell Design

Metamaterials are synthetic structures with electromagnetic properties which are not present in natural materials. Since their initial experimental realization, metamaterials have been utilized to increase the performance of different microwave devices, particularly antennas. Researchers have recently proposed various metamaterial-resonator-based techniques for achieving multiband, multi-polarized, and band-notched ultra-wideband antenna features [9]-[10]. Fig. 2 shows an NZIM structure for a unit cell with a width of 18 mm, a length of 13.50 mm, and a distance of 4.62mm from the patch. The full dimensions of NZIM are illustrated in Table 2. The frequency range corresponding to near-zero refractive index can be this factor is easily modifiable by adjusting these variables [11].

Table 2 NZIM Parameters

X	Y	W1	W2	W3	W4	L1	L2
4.5 mm	4.5 mm	4 mm	11.5 mm	0.4 mm	0.3 mm	4 mm	2.5 mm
G1	G2	G3	G4	G5	G6	S1	S2
1 mm	0.5 mm	1.6 mm	0.75 mm	1 mm	0.5 mm	0.5 mm	0.2 mm

2.3 Antenna Array Design

The schematic diagram of the proposed antenna array with NZIM superstrate is shown in Fig. 3. The 4 x 4 array is designed using 16 single elements and a T-shaped power divider to split power for each element. The antenna array elements are separated by λ/2 to avoid mutual coupling between each element. The proposed array is designed to increase the realized gain. The realized gain is increased by using the array to 14 dB.

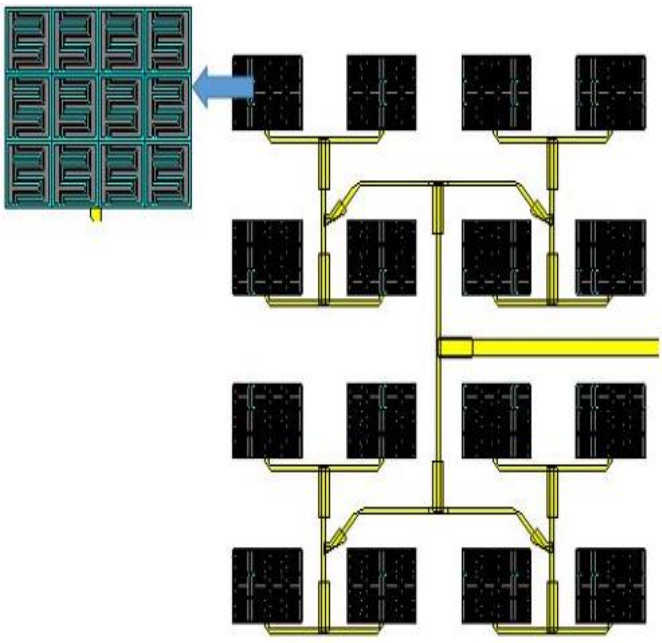

Fig. 3 The proposed antenna array with NZIM Superstrate.

3 Results and Discussion

In CSTMWS2020, the NZIM is designed using an FR4 substrate with a relative permittivity of 4.3 and a thickness of 1.57 mm. The unit cell NZIM is simulated with PEC and PMC border conditions. The PEC and PMC boundary conditions are constructed in such a way that an electric field exists along the y-

axis and a wave propagates along the z-axis. The effective medium parameters are derived from the scattering parameters. The extracted permittivity, permeability, and refractive index are presented in Fig. 4, Fig. 5, and Fig. 6 respectively.

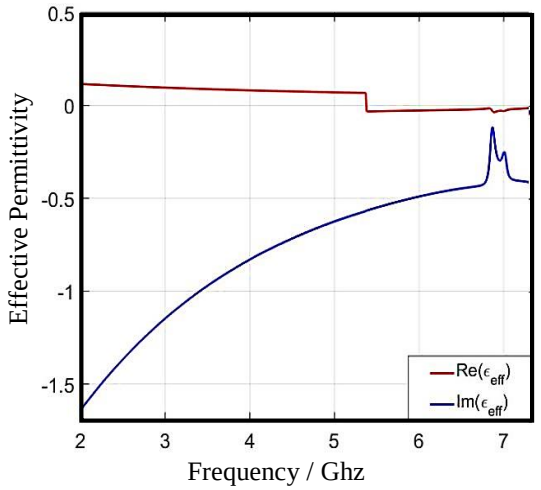

Fig. 4 NZIM Permittivity.

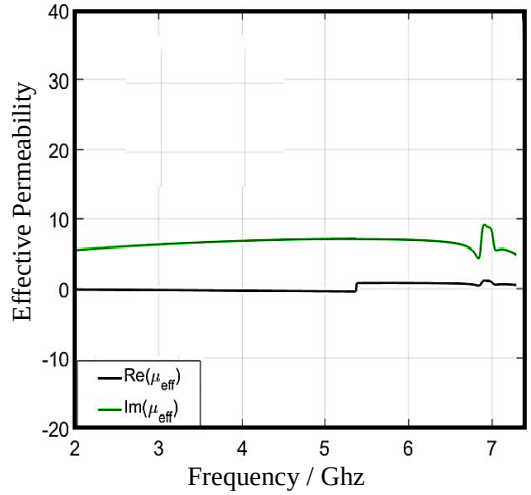

Fig. 5 NZIM Permeability.

The Fig. 4, the effective permittivity is extracted from the S12 parameter of the NZIM unit cell. The value of relative permittivity is near zero. Fig. 5 shows the real and imagine effective permeability of NZIM is near zero.

Fig. 6 shows the value of the refractive index is near zero at operating frequency, which leads to an increase in the overall realized gain of the antenna. The NZIM collimates the radiated beam of the antenna. Fig. 7 shows the variation of S11 of the patch antenna with frequency for a single element and the 4 × 4 arrays without NZIM.

In Fig. 7, the reflection coefficient shows the return loss due to the mismatch in impedance of the fed line and antenna. So, the lower value of the reflection coefficient is preferred, and -10 dB is the standard value for calculating impedance bandwidth. The proposed single-element design has a return loss of –48.8 dB. The variation of S11 of the patch antenna with frequency for a single element and the 4 × 4 arrays without NZIM has a return loss of -40 dB with the resonance at 5.8GHz with a bandwidth of 300 MHz for a single element. However, the bandwidth is 1 GHz for the antenna array illustrated.

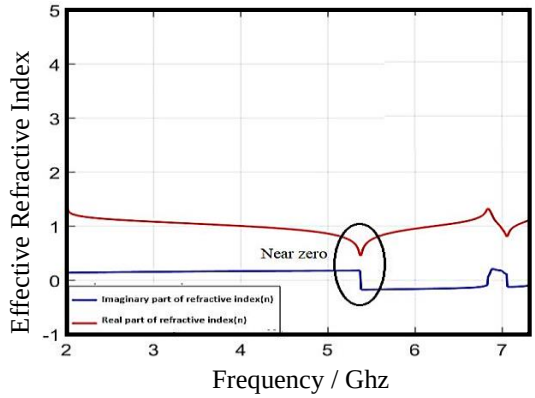

Fig. 6 Extracted real and imaginary parts of the refractive index for the proposed NZIM unit cell.

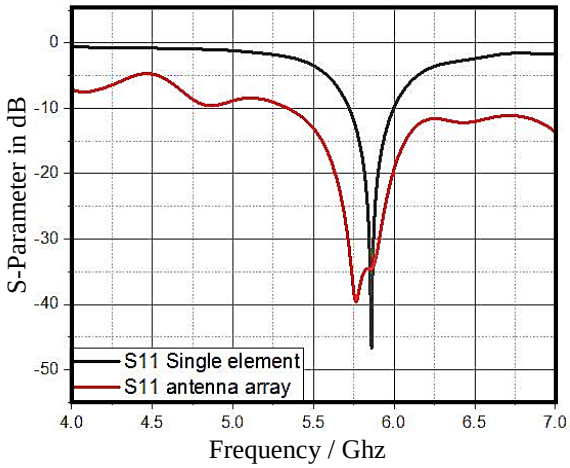

Fig. 7 The reflection coefficient of single element and antenna array.

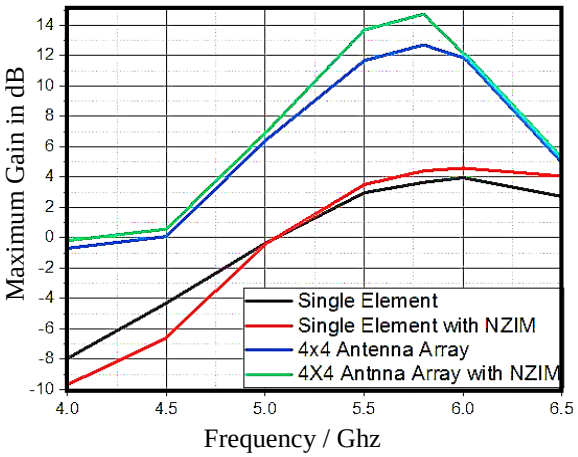

Fig. 8 High gain patch antenna with and without the NZIM superstrate.

The single-element design provides a gain of 3.7 dBi without NZIM and 4.41 dBi with NZIM at two resonating frequencies. The 4×4 array without NZIM increased the gain by 12 dBi, and the overall realized gain for the array with NZIM was enhanced to 14.22 dBi. The single element side lobe level without NZIM is -12.15 dB and the single element with NZIM achieves a -13.2 dB side lobe level. The 4×4 antenna array without NZIM side lobe level is 8.95 dB, and the 4×4 antenna array with NZIM is -9.4 dB, as illustrated in Fig. 8.

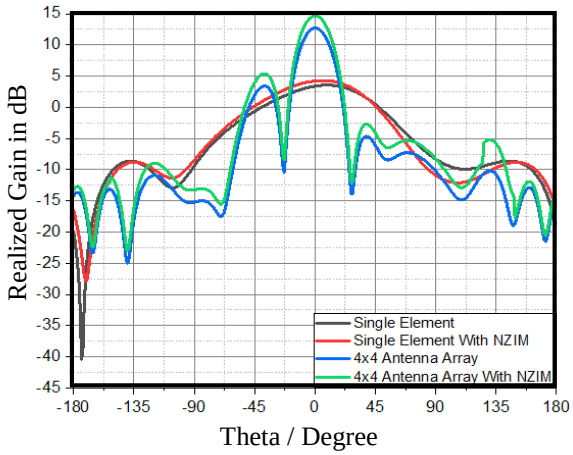

Fig. 9 The realized gain at operating frequency 5.8 GHz is simulated at constant phi = 90^o versus theta.

Fig. 9 shows that the single element side lobe level without NZIM is -12.15 dB and a single element with NZIM achieves a -13.2 dB side lobe level. The 4×4 antenna array without NZIM side lobe level is 8.95 dB, and the 4×4 antenna array achieves with NZIM -9.4 dB, and the overall realized gain for the array is 14 dB.

4 Conclusion

The MS- arrays are the best way to design low-profile antennas with high-performance parameters like gain and directivity, mutual coupling between elements of the array, and low side lobes. The necessity of high gain and protection from path loss will be necessary considering the expansion of modern technology in WLAN systems. This paper proposed a microstrip patch antenna to operate at a resonant frequency of 5.8 GHz. Moreover, it has also been deduced that numerous parameters of the antenna model have been the radiation pattern and antenna gain of the proposed antenna are studied and presented. Simulations using CSTMWS2020 verify several advantages, such as high antenna gain, stable radiation pattern, and good SLLs in both E- and H-planes. The proposed antenna is designed to operate for WLAN applications with high gain to cover the huge demand for data transferring rates with high performance. The NZIM unit cell increased the gain by increasing the directivity of the antenna. The 4×4 antenna array achieved an overall realized gain of 14 dB approximately by using the NZIM superstrate technique. The side lobe level is reduced to below -13 dB. All elements are designed using FR4 substrate to reduce the cost of implementation and fabrication because WLAN applications are commercial.

References

[1] Acıkaya, F.C. and Yıldırım, B.S., 2021. A dual-band microstrip patch antenna for 2.45/5-GHz WLAN applications. *AEU-International Journal of Electronics and Communications*, *141*, p.153957.

[2] Wang, J.J., Gong, L.L., Sun, Y.X., Zhu, Z.P. and Zhang, Y.R., 2014. High-gain composite microstrip patch antenna with the near-zero-refractive-index metamaterial. *Optik*, *125*(21), pp.6491-6495.

[3] Bouzouad, M., Chaker, S.M., Bensafielddine, D. and Laamari, E.M., 2015. Gain enhancement with near-zero-index metamaterial superstrate. *Applied Physics A*, *121*(3), pp.1075-1080.

[4] Kumar, R., Kumar, M., Chohan, J.S. and Kumar, S., 2022. Overview on metamaterial: History, types and applications. *Materials Today: Proceedings*, *56*, pp.3016-3024.

[5] Yu, K., Li, Y. and Liu, X.L., 2017, July. A high gain patch antenna using near zero-index metamaterial coating. In *2017 IEEE International Symposium on Antennas and Propagation & USNC/URSI National Radio Science Meeting* (pp. 2175-2176). IEEE.

[6] Jiang, Z.H., Wu, Q., Brocker, D.E., Sieber, P.E. and Werner, D.H., 2013. A low-profile high-gain substrate-integrated waveguide slot antenna enabled by an ultrathin anisotropic zero-index metamaterial coating. *IEEE Transactions on Antennas and Propagation*, *62*(3), pp.1173-1184.

[7] Ding, Z., Zhang, D. and Ma, C., 2020. A Study of a Microstrip Patch Antenna With a Drilled Through-Holes Array Structure Based on the Line Source Analysis Method. *Frontiers in Physics*, *8*, p.290.

[8] Yoshimura, Y., 1972. A microstripline slot antenna (short papers). IEEE Transactions on Microwave Theory and Techniques, 20(11), pp.760-762.

[9] Suthar, H., Sarkar, D., Saurav, K. and Srivastava, K.V., 2015, February. Gain enhancement of microstrip patch antenna using near-zero index metamaterial (NZIM) lens. In *2015 Twenty First National Conference on Communications (NCC)* (pp. 1-6). IEEE.

[10] Cheng, C., Lu, Y., Zhang, D., Ruan, F. and Li, G., 2020. Gain enhancement of terahertz patch antennas by coating epsilon-near-zero metamaterials. *Superlattices and Microstructures*, *139*, p.106390.

[11] Chen, X., Grzegorczyk, T.M., Wu, B.I., Pacheco Jr, J. and Kong, J.A., 2004. Robust method to retrieve the constitutive effective parameters of metamaterials. *Physical review E*, *70*(1), p.016608.

SciEn
Journal of Engineering Advancements Vol. 03(03) 2022, pp 76-90 https://doi.org/10.38032/jea.2022.03.002

A Remote Sensing-Based Approach to Identifying Spatio-Temporal Changes in Coastal Morphology in Bhola District, Bangladesh

Sharmin Sultana Toa[1] *and Al Artat Bin Ali*[2,*]

[1]Department of Environmental Science, Shaikh Burhanuddin Post Graduate College, Dhaka, Bangladesh
[2]Department of Geography and Environment, University of Dhaka, Bangladesh

Received: June 02, 2022, Revised: August 31, 2022, Accepted: August 31, 2022, Available Online: September 08, 2022

ABSTRACT

Bhola, the largest island of Bangladesh located at the estuarine mouth bar of the Bay of Bengal is very dynamic and unique in nature due to its physiographical configurations and is experienced severe morphological i.e. erosion- accretion changes. Of late, monitoring of coastal morphology and changes in shoreline trend analysis has conveniently been done through the integration of remote sensing satellite imageries and GIS techniques. The present study is an endeavor to detect and analyze the morphological changes on Bhola Island. Multi-temporal satellite images are the main data sources to attain the objectives through the integration of RS and GIS. The study concludes from the recent 42 years (1974- 2016) satellite data that- the Island is in the losing phase since 1974. The erosion processes are still active along the eastern and northeastern parts of Bhola Island due to the direct influence of the Meghna Estuary on the land by the steep bank slope, high tidal water pressure, and loose bank materials. Erosion is the burning issue on Bhola Island and due to this a large number of people are landless every year. On another side, accretion is being operated in a large part surrounding the Island increasingly in the southern part due to backwash sediment deposition by channel and estuary with the favor of a gentle topographic slope along the bank.

Keywords: Coastal Morphology, Shoreline Change, GIS, Remote Sensing, Erosion, Accretion, Sediment Deposition.

1 Introduction

Bangladesh, located in the tropics between 20°34' and 26°38' north latitude and 88°01' and 92°41' east longitude, shares its borders with India to the west, north, and northeast and with Myanmar to the south-east. With its extensive coastline, the Bay of Bengal serves as the defining feature of Bangladesh's southern border. The Ganges, the Brahmaputra, and the Meghna, together referred to as the GBM, are the three primary rivers that flow into Bangladesh from India. Within Bangladesh, these rivers meet up and eventually empty into the Bay of Bengal by a single outfall. Around 2.4 billion tons of silt are carried into the Bay of Bengal each year by the Ganges-Brahmaputra River (GBM) [1]. These sediments influence the dynamic processes that take place in the bay, leading to accretion in certain regions and erosion in others. There is a possibility that the buildup of silt in inner rivers is caused in part by the heavy sediment load from GBM as well as the strong tidal flow that prevents debris from flowing directly into the Bay of Bengal.

The ecology and ecosystem of Bangladesh are of a diverse nature due to its placement along the narrowest funnel-shaped and shallowest stretch of the Bay of Bengal in the south and the Himalayan ranges [2]. As a result of its geographic location and high population density, the country is particularly vulnerable to natural and man-made calamities. Nearly a quarter of Bangladesh's 24-billion-person population lives along the country's seashore. These areas are important to many of our coastal countries because they represent the interface between marine and terrestrial ecosystems. Delineation and monitoring of coastal changes are crucial for effective management. This includes hazard zoning, erosion-accretion investigations and analysis and modeling of coastal morpho-dynamics in addition to the more traditional coastal research. Change detection applications have grown more dependent on the integration of GIS and remote sensing data in recent years. Change detection is the process of finding differences in the condition of an object or phenomenon by multiple observations [4]. Widespread use of remote sensing technology for identifying spatio-temporal changes in the environment via satellite photography holds the promise of frequent map updates. Remote sensing data may be used to assess coastal processes such as erosion-accretion and shoreline changes. The ability of GIS to detect the spatial link between quality and temporal changes within an area over time is the primary benefit of this tool. For this reason, an accurate and dynamic monitoring of the changing coastline and delta zone is essential for obtaining a better knowledge of how the surface system of the Earth reacts to human activities. [5]

1.1 Problem Statement

Coastal zones across the globe are vulnerable regions that demand special consideration due to heightened natural and human-caused disruptions [6]. Bhola is home to a wide range of ecosystems and a wealth of promising coastal resources. The estuary and tidal influences of the Bay of Bengal have had a significant impact on the morphology of the island throughout time. It has decreased in size from 6,400 km^2 in 1960 to 3,400 km^2 now. Bhola has lost a total of 3,000 km^2 [7] because of this. It has only taken a few decades for many households and commercially vital areas on the island Bhola like Daulatkhan and Mirzakalu to be entirely eroded. Bhola might be gone in the next 40 years if the current pace of erosion continues [7].

*Corresponding Author Email Address: artat.ruhan@du.ac.bd Published by: SciEn Publishing Group

Sediment discharges from the combined flow of the Ganges, Brahmaputra, and Upper Meghna Rivers, which flow into the Meghna Estuary in Bangladesh, occur at an annual rate of more than one billion tons. This kind of shoreline movement is only seen in this part of the world [8]. Bhola Island, a portion of the Meghna Estuary, exhibits a cycle of erosion and accretion. It is possible that both natural and human forces are responsible for the erosion and accretion of Bhola Island. Physical variables that might affect the Meghna estuary include the flow of water from the upstream Ganges-Brahmaputra–Meghna Rivers, sediment load, tide, wave, water current, etc. Furthermore, human activity contributes to shoreline change. In terms of coastline morphology and erosion-accretion on this island, there is a direct association. These findings will help scientists better understand the island's morphological variations, as well as their connections. Multi-temporal and multi-resolution satellite images are the key data sources for emphasizing goals via the integration of Remote Sensing and Geographic Information System techniques.

1.2 Literature Review

When it comes to the effects of global warming, Bangladesh is among the most affected. The southernmost portion of Bangladesh is bordered by the Bay of Bengal. It stretches through around 710 kilometers and passes through 19 of the country's 64 districts. Among these 19 districts, only 12 have a shoreline or lower estuary [3]. Coastal zones are the areas where land and sea meet. Deltaic (Ganges delta), estuarine (Meghna estuary), and intra-deltaic landforms make up the majority of the coastal zone of Bangladesh (Chittagong coastal plain belt) [9]. About 100 km^2 of land is damaged every year by rivers, and 1300 km^2 of land that was once used for farming is now used for something else [10].

Bangladesh is especially vulnerable to rising sea levels because it is a coastal country with a lot of people and a flat landscape with wide and narrow ridges and valleys [11]. If the sea level goes up by 10cm, 25cm, or 1m by 2020, 2050, or 2100, respectively, it will affect 2%, 4%, and 17.5% of all land mass [12]. Ten percent of the country is less than one meter above the mean sea level (MSL), and a third of the country is affected by tides [13]. Every year, the sea level goes up 1 centimeter in Bangladesh [14]. If the sea level rises 1.5 meters along the coast of Bangladesh by 2030, it will affect 22,000 km^2 (16% of the total land area) and 17 million people, which is 15% of the total population [15]. Based on gauge data from 1985 to 2000, it has been shown that the MSL is rising at a rate of 3.15 mm/year, which is much faster than the current global average sea level rise of 2 mm/year [16]. Both the World Bank's projection of an increase in sea level of one meter and the UNEP's prediction of a rise in sea level of one and a half meters might potentially have an impact on about the same number of people, which is around 17 million. The char area prevents flooding in inland regions that might otherwise be caused by high tides. In addition to this, it contributes to the expansion of the land along the mainland. When all the chars are gone, the mainland will erode swiftly, causing Bangladesh's land area to diminish every year. If char areas break apart, the tidal surge will have a significant impact on the mainland [17].

The morphology of the Meghna Estuary is undergoing profound changes at a breakneck pace. [18]. The ecology of the Meghna Estuary is one of a kind, characterized by a continuous cycle of land development and erosion. The high flow of major rivers, enormous sediment loads, powerful tidal forces, wind actions, waves, cyclonic storm surges, and estuarine circulation are all factors that contribute to this phenomenon. The way in which these hydrodynamic forces interact with one another and how they operate together determines the form of the Meghna Estuary and the islands that are located within it [19].

The Ganges Brahmaputra Meghna (GBM) river system contains a massive amount of sediment in its stream. During the monsoon, the GBM system moves about 1.7 billion tons of silts per year, which makes the river very rough. This happens when riverbanks are slowly worn away by erosion [5]. The Meghna estuary is not a good place for people to live because it is prone to cyclones and storm surges [18]. The only time they lost land was from 1989 to 1999, when they lost about 81 km^2. About 769 km^2 of new land has been added to this area [20]. A natural process called accretion is making new chars along most of Bangladesh's 710 km of coastline [21]. The system of the Ganges, Brahmaputra, and Meghna rivers would create about 200 km^2 of new land every year in the Meghna Estuary and might create new char land outside the estuary [20]. The Centre for Environment and Geographic Information Services (CEGIS) says that Bangladesh's land area has grown by 20 km^2 (12.5 square miles) every year and that this growth could add up to more than 1000 km^2 in the next 50 years [22]. Most of the 230 km^2 of erosion on Bhola Island was caused by the changing flow of the Meghna channel [23].

Near the point where the Meghna River empties into the sea is an island known as Bhola. The location of Bhola Island indicates that the Meghna estuary and the tides of the Bay of Bengal have a significant impact on the island's form and the water around it. Since the year 1700, river and sea processes have been at work on this island, which was considerably smaller than it is today and has been changing as a result. While the Meghna estuary's large sediment channels contribute to the soil, the area is also being eroded by the enormous tidal surges that occur there. It is believed that the size and form of Bhola island have altered since the year 1960 as a direct consequence of the rise in sea level and the subsequent erosion of land [24]. The biggest problem in Bhola is that the river is eroding a lot of lands. Every year, 500 to 1,000 hectares of land are lost, along with the homes and means of survival of many people and water management equipment. On the shore of Bhola, scientists have measured erosion rates of up to 120 meters per year [25]. Bhola Island is the "ground zero" of climate change, and its residents are the first people in the world to have been forced to relocate as a direct result of the effects of climate change. Since 1995, increased wave energy and increasing water levels have eroded away almost half of the island [26].

1.3 Research Objectives

1. To detect and measure the coastal area (erosion-accretion) changes in Bhola Island from 1974 to 2016 using geospatial data.
2. To assess the trend of historical change by digital image processing and GIS techniques for quantification.
3. To identify the probable reason for the morphological change.

1.4 Hypothesis and Assumptions

Since 1960, it is likely that the shape and size of Bhola Island have changed because the sea level has been rising and the land around it has been eroding [24]. Due to changes in the island's shape, its shorelines and banks are eroding badly, and in a few places, new land is being added. As a result, the island loses more

land every year than it gains. The erosion and growth of the island are both very much affected by both natural and human factors. People in the area had been in trouble for a long time because of the channel's fast erosion. The rate of reclamation is lower than the rate of attrition, which means that a lot of land area is lost every year.

2 Study Area

Bhola is an administrative district in southwest Bangladesh that includes Bhola Island. Its coordinates are between 21°54' and 22°52' North and 90°34' and 91°01' East. It is in the Barisal Division and is surrounded by the Lakshmipur and Barisal Districts to the north, the Bay of Bengal to the south, the lower Meghna and Shahabzpur Channel to the east, and the Patuakhali District and the Tetulia River to the west. The name of the island used to be "Dakhin Shahbazpur." According to BBS, the Bhola district covers about 3,659.21 km^2, making it the largest island in Bangladesh. The island is about 90 kilometers long and 20 kilometers wide, and its shape is almost an arc from north to south. Since 1700 [24], both river and sea processes have been happening on this island, which used to be much smaller than it is now. The area under investigation includes seven Upazilas: Bhola Sadar, Daulatkhan, Burhanuddin, Char Fasson, Lalmohon, Tazumuddin, and Monpura (See Fig. 1). The island was given the name "Queen Island of Bangladesh" by the government of Bangladesh to promote its tourism industry.

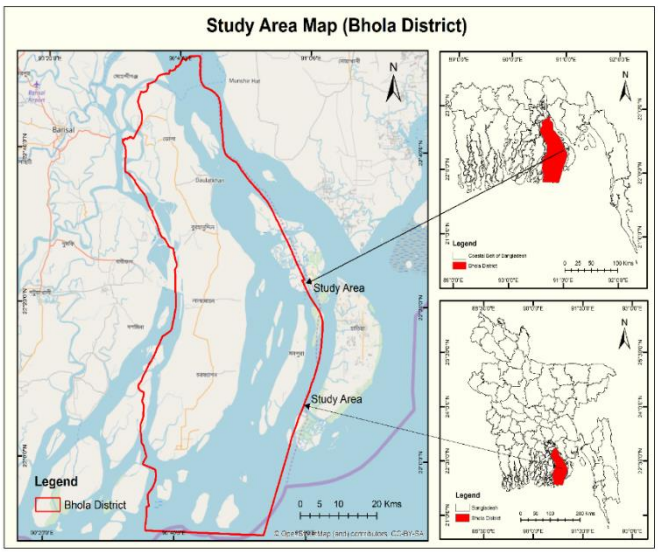

Fig. 1 Study Area Map (Bhola District, Bangladesh)

3 Materials and Methods

3.1 Satellite Data

Landsat satellite images from 1974 to 2016 were collected from the USGS-Glovis and Earth Explorer websites for this investigation. Cloud cover, scene visibility, satellite picture quality, and the availability of MSS, TM, ETM, and OLI-TIRS sensor satellite data were considered while selecting the images. In addition, all images were captured during the dry season (December through April) to avoid seasonal impacts (Appendix B: Table B1).

3.2 Image Processing

All images used in this research are USGS level-1 products, referred to as the World Geodetic System 1984 (WGS84) datum, in GeoTiff format, and projected using the Universal Transverse Mercator coordinate system (zone UTM 46 North). In this work, the McFeeters' normalized difference water index (NDWI), Xu's modified normalized difference water index (MNDWI), and land water mask (LWM) were utilized to identify changes in the coastline. The Landsat Thematic Mapper (TM) and Enhanced Thematic Mapper Plus (ETM+) sensors collect data and store it as a digital number (DN) ranging from 0 to 255. McFeeters's NDWI and Xu's NDWI need physical units, such as at-sensor radiance or top-of-atmosphere (TOA) reflectance, rather than the raw quantized calibrated pixel value (DN) [27].

3.3 Converting to TOA Reflectance

TOA reflectance can be obtained from the quantized calibrated pixel value [28] :

$$P_\lambda=\pi^* L_\lambda*d^2/ ESUN_\lambda*Cos\theta_s$$

L_λ can be obtained from the quantized calibrated pixel value [28] :

$$L_\lambda = ((LMAX_\lambda- LMIN_\lambda)/(Qcalmax- Qcalmin))*(Qcal-Qcalmin)+ LMIN_\lambda$$

where,

$LMAX_\lambda$ is the maximum spectral at-sensor radiance scaled to Qcalmax [W/(m^2.sr.µm)], $LMIN_\lambda$ is the minimum spectral at-sensor radiance scaled to Qcalmin [W/(m^2.sr.µm)], Qcalmax is the maximum quantized calibrated pixel value corresponding to $LMAX_\lambda$ [DN], Qcalmin is the minimum quantized calibrated pixel value corresponding to $LMIN_\lambda$.

The Equations parameters may be retrieved from the header files of the ALI, TM, ETM+, and OLI datasets [27].

3.4 Image Classification/ Image Index

Classification of images is used to extract the required image attributes. Common approaches for extracting water bodies and mapping coastlines include the classification of general features. Nevertheless, the general classification approach assumes that the pixel is pure. When numerous characteristics are available inside a single pixel, the accuracy of such classification systems will rely on the landscape's complexity and the completeness of a lengthy training period [29]. In addition, the majority of these methods rely heavily on human skill and regional knowledge. Because water bodies, such as floods, tides, and storm surges, may move rapidly [30], they will encounter obstacles when attempting to execute a quick and repeatable extraction of water-body information. The spectral water index is a popular tool for identifying the boundary between water and land. Normalized difference water indices (NDWIs) computed from several band combinations (green, near-infrared (NIR), or shortwave-infrared (SWIR)) have been effectively implemented in land-water mapping. In reality, when Advanced Land Imager (ALI) data are utilized, additional NDWIs will become accessible, since the ALI sensor gives one green band (Band 4), two NIR bands (Bands 6 and 7), and three SWIR bands (Bands 8, 9, and 10). Therefore, choosing the best band or combination of bands is crucial when mapping Land-Water using ALI data [27]. Spectral water index methods, such as McFeeters's NDWI [31], which is calculated from one green-band image and one NIR-band image, and Xu's NDWI or MNDWI [32], which is calculated from one green-band image and one SWIR-band image, can extract water body information more precisely, quickly, and easily than general feature classification methods. In addition, McFeeters' NDWI and Xu's MNDWI have been effectively used to remotely sensed data to extract water information [26],[32]-[36]. Therefore, McFeeters' NDWI and Xu's MNDWI were utilized as

the principal tools for this study on mapping coast lines using TM, ETM+, and OLI remotely sensed images. The NDWI of McFeeters forms two models, whereas the NDWI of Xu creates three models. The MSS image has been categorized using the Land Water Mask (LWM) index since the MSS sensor has just four bands (Band 6, Band 7, Band 8, and Band 9).

3.4.1 Normalized Difference Water Index (NDWI)

The Normalized Difference Water Index (NDWI) is produced from the same fundamentals as the Normalized Difference Vegetation Index (NDVI) (NDVI). In an NDVI (comparison of differences between two bands, red and near-infrared (NIR)), the presence of terrestrial plant and soil characteristics is accentuated while the presence of open water features is muted due to the various ways these features reflect these wavelengths [31]. Calculating the NDVI index is as follows:

NDVI= (ρNIR – ρRed) / (ρNIR +ρ Red)

If the equation is inverted and the green band is utilized in place of the red band, the result would likewise be inverted, with vegetation suppression and open water enhancement [31]. The formula for an NDWI is:

NDWI= (ρGreen – ρNIR) / (ρGreen + ρNIR)

Where, ρGreen and ρNIR represent the green and NIR reflectances, respectively. This equation yields positive values for aquatic features, whereas soil and terrestrial vegetation have zero or negative values [31]. McFeeters's NDWI is intended to (1) increase the reflectance of a water body by employing green wavelengths, (2) decrease the poor NIR reflectance of water bodies, and (3) make use of the high NIR reflectance of plant and soil characteristics [37]. As a consequence, the background (vegetation and soil characteristics) information in McFeeters' NDWI images will be limited and the water body information will be increased [27]. Consequently, the water bodies may be recognized by applying a threshold to McFeeters' NDWI images.

3.4.2 Modified Normalized Difference Water Index (MNDWI)

McFeeters's NDWI can increase information about water bodies and limit information about vegetation and soil characteristics, but it cannot discriminate entirely between water bodies and built-up features [27]. To solve this issue, Xu's NDWI or MNDWI (Xu, 2006) was created; it is defined as:

MNDWI= *(ρGreen – ρSWIR) / (ρGreen + ρSWIR)*

Where, ρSWIR is the reflectance in the SWIR band.

The NDWI developed by Xu may increase open-water features while suppressing and even deleting built-up features, vegetation, and soil features. The indices employed in the current investigation are reported in Appendix B: Table B2 for the best possible outcome.

3.5 Image Threshold

In order to identify changes in the coastline on a picture, the threshold between sea and land must be set. In this part, classification techniques for water-land lines were done. The setting of a threshold is a crucial step in determining McFeeters' or Xu's NDWIs. The threshold values for McFeeters' and Xu's NDWIs were set to zero [31][32], however, threshold change in certain circumstances may result in a more precise delineation of water bodies [38]. Therefore, dynamic or variation thresholds are required to recognize water body information [39] when various areas or phases of remote sensing data are utilized. The maximum between-class variance technique (Otsu method) is an example of a dynamic threshold approach [40]. In this work, the Otsu approach was employed to establish the separation threshold between water bodies and background characteristics.

Now, if it is assumed that the NDWI/MNDWI pixels range from $-1 \leq a < b \leq 1$

Using the Otsu method, the pixels can be divided into two classes: a non-water class ranging from [*a*, ..., *t*] and a water class ranging from [*t*, …, *b*], where *t* is the threshold value [27]. The between-class variance of the non-water class and water class can be obtained by:

$\sigma^2 = W_{nw}\sigma^2_{nw} + W_w\sigma^2_w$

Where, σ is the between-class variance of the non-water class and the water class; σ^2 is the variance of the non-water class; σ^2 is the variance of the water class; is the weighting of the non-water class, and is the weighting of the water class. The W_x is given by:

$$Wx = \sum_{a}^{b} P(i)$$

where, P (i) is the class probability; the total number of pixels in the image is divided by the number of pixels in the class.

Using equations, the Otsu technique determines the threshold based on the highest between-class variation of background variables (e.g., vegetation, soil, etc.) and water body features [27]. The larger the variance, the greater the contrast between the backdrop and water characteristics. Consequently, enhancing the variation between water body characteristics and background characteristics reduces the likelihood of misclassification. When the NDWI/MNDWI image has a significant between-class variation, a spectral water index model is better appropriate for enhancing and extracting water bodies.

4 Coastal Morphological Change Detection

The coastal morphology of Bangladesh experiences significant changes due to erosion and accretion. The coastline morphology change can be analyzed from two aspects: the change of coastline i.e. shoreline length and area, and the change of coastline types i.e. erosion-accretion [41]. All the shorelines are overlaid concurrently, and a baseline is manually established in the area. This baseline serves as a reference point for subsequent phases [42].

4.1 Images Interpretation and Coastal Morphology Change Analysis

4.1.1 Changes in Coastal Morphology from 1974 to 1980

The overall length of Bhola Island's coastline increased from 224.406 km in 1974 to 228.3 km in 1980. In 1974, the area of Bhola District was around 1846.75 km^2; by 1980, it had decreased to 1814.74 km^2. The overall area of Bhola Island expanded, although erosion processes were significant in the neighboring land areas (Appendix B: Table B3).

From 1974 to 1980, the satellite image reveals that the coastline expanded by 73.54 kilometers. The erosion and accretion were about 118.67 km^2 and 86.66 km^2 respectively, resulting in a net land loss of 32.01 km^2. On Bhola Island, the net loss was 55.35 km^2 (Appendix B: Table B4).

In the northern, northeastern, and western regions of Bhola Sadar Upazila, erosion processes were active. In the northern bend of Bhola Sadar Upazila in 1974, satellite imagery revealed

the formation of char areas that vanished in 1980. In the northwestern bend, accretion was effective.

Due to Meghna River's direct effect, the eastern portion of Daulatkhan upazilla was severely degraded. In the northeastern portion of this Upazila, Char land was also produced. In Burhanuddin upazila accretion and erosion both processes were prominent in the time series of 1974-1980. Erosion was active along the shoreline and there also formed char land surrounding the bank of Tetulia River. In the northern tip of Tazumuddin Upazila erosion process was at a higher rate than in the other areas of Bhola District. Erosion was active along the shoreline and Char land which formed previously may disappear.

Southern bend of Charfasson upazilla was dominated by the erosional process. In the southern portion of Bhola Island, where a massive tidal current and a steep slope of the coastline (bank) were the most likely sources of erosion from 1974 to 1980, erosion was likely to have occurred (Appendix A: Fig. A1). This time period's satellite images reveal that erosion was effective in a portion of the southwestern and southern regions (Char Kukri Mukri, Dhal Char, and Char Sakuchi). Accretion also occurred in the northern portion of Char khukri-Mukri, Dhal Char, and their environs as a result of natural sediment deposition brought by the water of Shahbajpur canal, which is part of the Meghna estuary.

There was also accretion of land in the eastern part Manpura Island from 1974 to 1980 timespan that was dispersed from Bhola Island but included in Bhola administrative boundary (Appendix A: Fig. A1). Erosion process was also dynamic in the shoreline. The erosion processes were more effectively severe than accretion which resulted in the loss of about an overall 32.01 km^2 land area and 55.35 km^2 area from Bhola Island to become eroded. The rates of total erosion and accretion were 19.78 km^2 and 14.6 km^2 respectively.

4.1.2 Changes in Coastal Morphology from 1980 to 1990

In 1980 Bhola District had an area of about 1814.74 km^2 and the shoreline was 580.56 km which became respectively 1880.33 km^2 and 699.53 km in 1990. According to the table (Appendix B: Table B5), the accretion process was dynamic in this timespan.

The shoreline increased by 118.97 kilometers between 1980 and 1990, according to statistics on shoreline and area change. The Bhola mainland shoreline grew by 10.68 kilometers. During this time period, total erosion and accretion were approximately 109.52 km^2 and 211.56 km^2, respectively. Thus, the net increase in land area was about 68.26 km^2 (Appendix B: Table B6).

From 1980 to 1990 time period, erosion processes were active in both the eastern and western parts of Bhola Sadar, Daulatkhan, western Burhanuddin, and the eastern side of Tazumuddin, where huge tidal pressure water from the Meghna estuary through the Shahbazpur Channel in the east and Tetulia river from the west of the bankline were the probable causes for erosion to happened (Appendix A: Fig. A2).

Within this time span accretion was also dynamic in a large part of northern Bhola Sadar, there were also formed new char in the Tetulia River through accretion. Accretion was prominent in Daulatkhan, Tazumuddin, Burhanuddin Upazila. Monpura Upazila and the southern part of Bhola Island were also accreted due to the natural sediment deposition of the Meghna estuary through Shahbazpur channel compensated for the big erosion in the Bhola Sadar, Daulatkhan, and Burhanuddin upazila. Surrounding the Bhola Island, especially in Char Fasson upazila, lots of char areas are created through accretion. The data from satellite images show that in this time period the island gained maximum sediment deposition (land area) which resulted in the formation of a new island (char) surrounding the Bhola Island (Appendix A: Fig. A2).

The erosion rate was 10.95 km^2 whereas the accretion rate was 21.15 km^2. In Bhola Island rate of erosion and accretion were 8.8 km^2 and 2 km^2 respectively. So erosion process was dominant in Bhola Island and the surrounding area was accreted due to sediment deposition. The erosion process was higher in Bhola Island due to the direct influence of the Meghna Estuary on the Bay of Bengal.

4.1.3 Changes in Coastal Morphology from 1990 to 1995

The total shoreline of Bhola Island was about 699.53 km in 1990 which became about 856.28 km in 1995. In 1990, the total land area of Bhola Island was 1880.33 km^2 and in 1995 it was 1974.98 km^2. In the Bhola mainland, the area was about 1447.43 km^2 in 1990 which became 1435.26 km^2 by losing 12.17 km^2 of land area (Appendix B: Table B7).

From 1990 to 1995, the total Shoreline change was 156.75 km. The erosion and accretion were about 97.28 km^2 and 155.17 km^2 respectively. Thus net gain of the land area was 57.89 km^2 and on the mainland, it was a net loss of about 12.17 km^2 (Appendix B: Table B8)

Erosion processes were active in northern and north-eastern (Bhola Sadar Upazila), eastern (Daulatkhan Upazila), eastern (Burhanuddin Upazila) eastern (Lalmohon and Tazumuddin Upazila) of the Bhola District, due to the Meghna estuary water in northern and north-eastern portion and steep slope of the shoreline (bank) of these areas were the probable causes for erosion to happen from 1990 to 1995 (Appendix A: Fig. A3). Char land were formed in the Tazumuddin and Daulatkhan Upazila along the Bhola Island which disappeared due to excessive erosion.

New char lands (accretion) evolved in the southern part of the Bhola district like Char Fasson Upazila and surrounding Monpura Island due to sediment deposition by the Shahbazpur Channel through Meghna Estuary (Appendix A: Fig. A3). There was also the formation of Char land in the northeastern bend of Bhola Island mainly in the Bhola Sadar Upazila and Daulatkhan Upazila.

During 1990-1995 in 5-year intervals, total erosion and accretion rate were about 19.46 km^2 and 31.03 km^2 respectively which represented the net gain rate was higher. On Bhola Island, the rate of erosion and accretion were 5.01 km^2 and 2.57 km^2. According to the statistics resulting from the satellite imageries, erosion was more dynamic in Bhola Island than accretion. The new island formed surrounding the Bhola Island which compensated for the net loss to gain of land area.

4.1.4 Changes in Coastal Morphology from 1995 to 2000

Appendix B: Table B9 shows that the total shoreline of Bhola Island was about 856.28 km in 1995 which has become about 914.58 km in 2000. The entire land area of Bhola Island was 1974.98 km^2 in 1995 and 1964.84 km^2 in 2000 (Appendix B: Table B9).

In the time period from 1995 to 2000, the total shoreline change was 58.3 km. On the mainland of Bhola, it was 11.79 km. The amount of erosion and accretion were about 140.98 km^2 and 131.40 km^2 respectively where the net loss was 9.58 km^2. In the Bhola Mainland erosion and accretion were 45.83 km^2 and 13.01 km^2 and the net loss was 32.82 km^2 (Appendix B: Table B10).

The satellite image results from 1995 to 2000 time period reveals that in Bhola Sadar Upazila erosion processes were active in the north-eastern, eastern, and south-western part. The Eastern part of Daulatkhan Upazila, Burhanuddin Upazila, Tazumuddin Upazila were highly erosion-prone. In the northeastern part of Bhola Island, many new islands (Char) were created which became fragmented due to erosion through the pressure of tidal water. Islands located in the southern Bhola Island including Char Kukri-mukri, Dhal Char, Char Nizam, char Sakuchi were eroded along its shoreline in the southern part.

From 1995 to 2000, accretion was active in the northern and western part of Bhola Sadar Upazila, eastern Daulatkhan, eastern and southern Tazumuddin, upper part and surroundings of Manpura Island due to sediment deposition by Meghna estuary (Appendix A: Fig. A4).

Bhola Island's morphology was approximately the same between 1995 to 2000-time span. On Bhola Island, the net loss was about 32.82 km^2 and the rate of erosion and accretion were about 9.16 km^2 and 2.60 km^2. The erosion rate was always higher than the attrition in Bhola Island due to the high tidal pressure of the Meghna Estuary. In Bhola District net loss was 9.58 km^2 whereas erosion and accretion rates were 28.19 km^2 and 26.28 km^2.

4.1.5 Changes in Coastal Morphology from 2000 to 2005

According to the Appendix B: Table B11 below from 2000 to 2005, the total land area of Bhola reduced from 1964.84 km^2 to 1921.22 km^2 whereas the mainland of Bhola reduced from about 1402.43 km^2 to 1370.18 km^2. The total shoreline was about 914.58 km which became 962.04 in 2005 (Appendix B: Table B11).

Total Shoreline change was about 47.46 km whereas in the Bhola mainland it was less in amount. According to the Satellite image from 2000 to 2005 timespan erosion and accretion were 134.22 km^2 and 90.60 km^2 respectively. On Bhola Island, it was 41.72 km^2 and 9.48 km^2. So a net loss of land area was active due to shoreline or bank line erosion. The total net loss was 43.62 km^2 (Appendix B: Table B12).

From 2000 to 2005 timespan erosion process was active in the northeastern and southwestern part of the Bhola Sadar, eastern and western Burhanuddin, and eastern Daulatkhan, both eastern and western Tazumuddin, eastern Lalmohon, northern Manpura, and some parts of Char Fasson Upazila. The Eastern part of Bhola Island was more vulnerable to erosion than the western part due to the direct influence of tidal pressure of Meghna Estuary and Shahbazpur Channel. The erosion process remained active during the monsoon period (Appendix A: Fig. A5).

Accretion was also active but in less intensity than erosion in this time span. The western part of Tazumuddin, the periphery area of Manpura Island, and the lower part of Char Fasson Upazila including Char Kukri-Mukri, Dhal char, Char Momtaz; accretion were dynamic in this area. In the northwestern part of Bhola Island, both accretion and erosion were active simultaneously. But in 2000 to 2005 timespan net loss of land area happened and there was a total 43.62 km^2 area which became lost where the amount of net loss was about 32.24 km^2 for Bhola Island. The total rate of erosion and accretion in this time period were about 26.84 km^2 and 18.12 km^2 respectively.

4.1.6 Changes in Coastal Morphology from 2005 to 2010

The total shoreline area of the mainland of Bhola Island was about 231.14 km in 2005 and it became 235.73 km in 2010. Total Bhola Island was about 1370.18 km^2 in 2005 and in 2010 it reduced to 1357.94 km^2. The mainland of the Bhola island area has also been eroded (Appendix B: Table B13).

The satellite image reveals that the shoreline increased by 147.3 kms between 2005 and 2010. The erosion and accretion throughout this time period were about 74.21 km^2 and 215.33 km^2, resulting in a net increase of 141.12 km^2 of land area. However, the Bhola mainland region had a net loss of 12.25 km^2 (Appendix B: Table B14).

According to the Satellite image data in the time period, 2005 to 2010 accretion was more dynamic than erosion. Erosion was active in northern and north-eastern Bhola Sadar, eastern Daulatkhan and Burhanuddin, north-eastern Lalmohon, the southern part of Char Fasson, and the northern tip of Monpura Island. The overall erosion rate was 5.05 km^2/year, whereas on Bhola Island it was 5.07 km^2/year (Appendix A: Fig. A6).

Conversely, accretion was noticeable in most of Bhola Island including the eastern part of Bhola Sadar, Daulatkhan, Tazumuddin, Manpura Upazila, the western part of BurhanUddin, Lalmohon, and the southern part of Char Fasson Upazila including Char Nizam, Char Kukri Mukri due to the sedimentation through the Meghna estuary which got hindrance to passes its channel to the Bay of Bengal. Sediment accumulated and aggregated alongside char lands which caused the addition of land.

There new Islands (chars) were created surrounding Bhola Island. The rate of accretion was about 43.66 km^2/year. The total net gain was 141.12 km^2 which was a vast area. Due to the accretion process total shoreline area also increased and it became 147.5 km. In Bhola Island, the rate of total erosion and accretion was 5.07 km^2/year and 2.62 km^2/year.

4.1.7 Changes in Coastal Morphology from 2010 to 2016

The total shoreline area of the mainland of Bhola Island was about 235.73 km in 2010 and it became 248.25 km in 2016. Bhola Island was about 2062.34 km^2 in 2010 and in 2016 it reduced to 2001.61 km^2. The total Shoreline was 1109.34 km^2 in 2010 which became 1117.99 km^2 in 2016 (Appendix B: Table B15).

From 2010 to 2016, the shoreline changed a total of 8.65 km. On the Bhola mainland, it was 12.52 km. The quantity of erosion and accretion was between 168.42 km^2 and 107.70 km^2, with a net loss of 60.72 km^2. The Bhola Main Island had 35.03 km^2 of erosion and 5.46 km^2 of accretion, for a net loss of 29.57 km^2 (Appendix B: Table B16).

During the year from 2010 to 2016 erosion was active in the northeastern part of Bhola Sadar. As a result, the land area formed in 2010 by the accretion process might be fragmented through erosion. The erosion process was prominent in eastern Tazumuddin, Daulatkhan, Burhanuddin, Manpura Island, and southeastern Lalmohon. Erosion also occurred in the eastern part of Tazumuddin in the Char area named Char Munshi, char Hazari. The additional area created in the 2005 to 2010 time period got fragmented due to erosion by the high tidal influence of Meghna Estuary.

Accretion was also active in a small portion of the erosion-prone area including the eastern and south-western parts of Bhola Sadar, and eastern Daulatkhan Upazila. Accretion has been placed in the southern part of Bhola Island including southern Char Fasson like Char Sakuchi, Dhal Char, the upper part of Char Kukri-mukri, and both the southeastern and western side of Manpura Island. Due to the direct influence of the Meghna

estuary, the transformation of the land area was more active in the eastern part of Bhola Island. (Appendix A: Fig. A7).

Rate of total erosion and accretion were about 33.68 km^2/year and 21.72 km^2/year which represented the dominance of the losing process. The total net loss in Bhola District was about 60.72 km^2 area. During the time period, 2010 to 2016 common land area was 1893.91 km^2. In Bhola Island, the rate of erosion and accretion were about 7 km^2/year and 1.09 km^2/year whereas the erosion rate is 6 times higher than accretion. In Bhola Island shoreline increased due to the creation of a bend area through the erosional process done by the estuary. The total net loss in Bhola Island was about 29.57 km^2 whereas the overall district lost about 60.72 km^2.

4.1.8 Changes in Coastal Morphology from 1974 to 2016

The final result from satellite image analysis (1974- 2016) revealed that the total shoreline of Bhola Island was about 507.017 km in 1974 which increased to about 1117.99 km in 2016 (Appendix B: Table B17).

In 1974, the total land area of Bhola Island was 1846.75 km^2 whereas in 2016 it increased to 2001.61 km^2 (Appendix B: Table B17). Total shoreline area and total land area increased over these 42 years of time span.

The data of change in shoreline and area of Bhola district from 1974 to 2016 concludes that the shoreline gain was 610.98 km in this time period. The erosion and accretion were about 343.30 km^2 and 498.15 km^2 respectively. Common land between 1974 to 2016 was 1503.46 km^2. Therefore, the net gain of the land area is about 154.85 km^2 from 1974 to 2016 (Appendix B: Table B18).

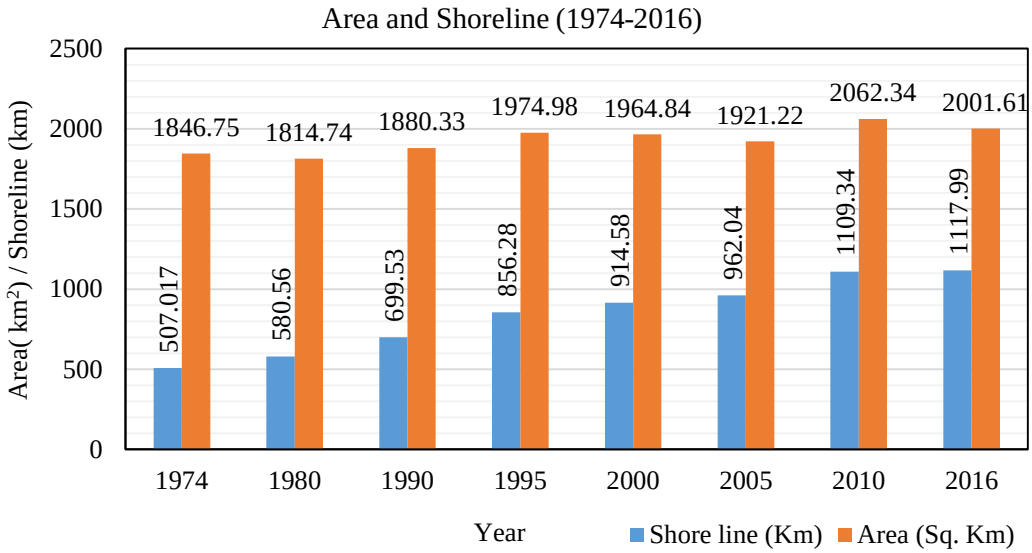

Fig. 2 Area and Shoreline Changes of Bhola District in 1974 and 2016

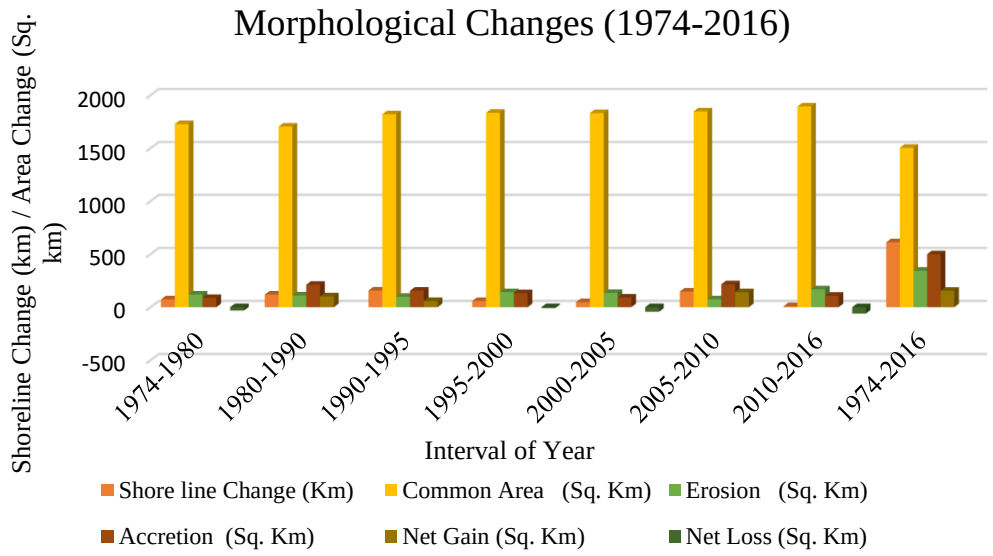

Fig. 3 Changes in Bankline/Shoreline and Area of Bhola District from 1974 to 2016

The composite or final result of the last 42 years from 1974 to 2016 (present time period) satellite image data concludes that substantial erosion processes were underway in the northern part of Bhola Sadar, eastern (Bhola Sadar, Daulatkhan, Lalmohon, Burhanuddin, Tazumuddin Upazila), southwestern (Char Fasson Upazila and Daulatkhan Upazila), and some of northern Monpura Island, where huge tidal pressure water from Meghna estuary and Bay of Bengal and steep slope of the shoreline (bank)

were the probable causes for erosion to operate in these erosion prone areas (Appendix A: Fig. A8). In the eastern portion of Bhola Island, intense erosion processes led to the loss of a wide area around the island.

In contrast, accretion was effective in a significant portion of the north-eastern region of Bhola Sadar (Char Munsi, Hazari), the northern region of Monpura Island, and the southern region of Char Fasson Upazila. In the southern part of Bhola Island, there was the accretion of the land area surrounding Char Kukri-mukri, Dhal Char, Char Nizam, etc. Addition of some new Char lands, surrounding the Bhola Island that was not authorized by the Government for its unstable condition. Some Char areas were not permanent and sank under water during the period of high tide. The accretion process likely happened as a result of the relatively mild slope of the bank, which permits natural silt deposition transported by water from the Shahbazpur canal and the Meghna estuary. This pattern of high accretion is not uniform throughout the coast, since major erosion has occurred on the western shore of the Meghna River estuary and along the northern sections of Manpura and Hatiya Islands, perhaps as a result of the influence of strong river currents. In addition, engineering activities, such as dam and dyke building, have restricted downstream water flows and sediment transport for deposition, but high tidal flows may aid sediment movement away from the shore.

The shoreline of Bhola District increased from 1974 to 2016 and it became 610.98km. Increasing of shoreline doesn't indicate the addition of land area to the island, the length is increasing due to the erosional process which creates a bend into the shoreline. The shoreline of Bhola Island increased at a rate of 14.54 km/year. From 1974 to 2016 in 42 years timespan, there were 1503.46 $km^{2\ of}$ common land areas.

The data from satellite images showed that in this time period the island gained 498.15 km^2 with the rate of 11.86 km^2/year of new land through natural sediment deposition resulting in the formation of a new island (char) in various parts of Bhola and loosed about 343.30 km^2 with the rate of 8.17 km^2/year due to erosion along the shoreline of eastern, southern, and some of south-western part of the island (Appendix A: Fig. A8). The net gain of land due to the predominant accretion process than erosion results in about 154.85 km^2 with the net gain rate of 3.7 km^2/ year area to be added. Primarily, physical e.g. geomorphic, hydrologic, etc. causes were responsible for erosion and accretion. Human effects had little impact on coastal morphology change. Due to the variable current conditions of the Shahbazpur canal and the Tutulia River, accretion is occurring in the northern and western portions of Bhola Island. The Tetulia River in the west erodes less than the Shahbazpur River in the east due to its slower flow rate. On the other side, in the eastern portion, substantial sediment erosion is occurring. If the cross dam project is implemented on the eastern part of the island, the sediments transported by the Meghna estuary may be stopped, which might lead to the development of a vast land area surrounding the offshore island.

5 Conclusion

Analysis of Landsat images taken at different times from 1974 to 2016 showed that Bhola Island seemed to have changed mostly in the erosional phase. There are many things that affect how the Bhola Island changes. Some of these are hydrologic (river discharge, sediment load, minimum dry period flow, and the amount of sediment moved), marine hydraulic (tides, sea level rise, storm surge, currents, and wave action), geomorphologic and geological, climatic, land use, and human activities (embankments, sand extraction, irrigation, etc.). It is clear that recent human actions have had a big effect on how the island has grown and changed. In general, the effects of human activity on a coastal island include things like artificial diversion, building embankments, making channels, dredging, and irrigation. But these things don't happen very much in the study area. But taking sand from the southeast side of Bhola Island has caused erosion in a small area there. Most of the changes to the island are happening at the bend of the shoreline, where the shore meets the river flow, where the bank is weak, where a bank side has fallen, and when a tidal surge hits (evidence of field visit). On Bhola Island, erosion is always happening, but it is most noticeable during the wet season. Bankline and shoreline erosion became a common problem on Bhola Island as a result.

References

[1] Holeman, J.N., 1968. The sediment yield of major rivers of the world. *Water Resources Research*, *4*(4), pp.737-747.

[2] Amin, S.M.N., 2008. Studies on coastal environments in Bangladesh. *Dhaka, Bangladesh: AH Development Publishing House*.

[3] Islam, M.S. and Salehin, F., 2013. Coastal Zone and Disaster Management in Bangladesh. *CRU, Dhaka*.

[4] Singh, A., 1989. Review article digital change detection techniques using remotely-sensed data. *International journal of remote sensing*, *10*(6), pp.989-1003. Wang X, Liu Y, Ling F, Liu Y, Fang F. Spatio-Temporal Change Detection of Ningbo Coastline Using Landsat Time-Series Images during 1976–2015. *ISPRS International Journal of Geo-Information*. 2017; 6(3):68. https://doi.org/10.3390/ijgi6030068

[5] Wang, X., Liu, Y., Ling, F., Liu, Y. and Fang, F., 2017. Spatio-temporal change detection of Ningbo coastline using Landsat time-series images during 1976–2015. *ISPRS International Journal of Geo-Information*, *6*(3), p.68.

[6] Shamsuddoha, M. and Chowdhury, R.K., 2007. Climate change impact and disaster vulnerabilities in the coastal areas of Bangladesh. *COAST Trust, Dhaka*, pp.40-48.

[7] Hussain, M.A., Tajima, Y., Gunasekara, K., Rana, S. and Hasan, R., 2014. Recent coastline changes at the eastern part of the Meghna Estuary using PALSAR and Landsat images. IOP Conf. *Ser. Earth Environ. Sci*, *20*(012047), pp.1755-1315.

[8] Khan, S.R., 1999. Geomorphic and Geological Characteristics of the Coastal Plains of Bangladesh, In proceeding of the international seminar on the *Quaternary Development and Coastal hydro-dynamics of Ganges delta in Bangladesh*, 20- 24 September, Dhaka.

[9] Alam, M.S. and Uddin, K., 2013. A study of morphological changes in the coastal areas and offshore islands of Bangladesh using remote sensing. *American Journal of Geographic Information System*, *2*(1), pp.15-18.

[10] Brammer, H.; Asaduzzaman M. and Sultana, P. Effects of Climate and Sea-level Changes on the Natural Resources of Bangladesh, *Briefing Document No. 3. Bangladesh Unnayan Parishad (BUP)*, Dhaka, 1993.

[11] World Bank. Bangladesh: Climate Change & Sustainable Development. *Report No. 21104 BD*, Dhaka, 2000.

[12] Sharmin, S., 2013. Climate change and its effect on coastal area of Bangladesh. *Asian Journal of Science and Technology*, *4*(12), pp.15-20.

[13] Frihy, O.E., 2003. The Nile delta-Alexandria coast: vulnerability to sea-level rise, consequences and adaptation. *Mitigation and Adaptation Strategies for Global Change*, *8*(2), pp.115-138.

[14] UNEP, 1989. Available online: (http://www.grida.no) (Accessed on 18 September 2018)

[15] Hazra, S., Ghosh, T., DasGupta, R. and Sen, G., 2002. Sea level and associated changes in the Sundarbans. *Science and Culture*, *68*(9/12), pp.309-321.

[16] Sarwar, G.M., 2005. *Impacts of sea level rise on the coastal zone of Bangladesh.* MSc Thesis, Lund University, Lund.

[17] Brammer, H., 2014. Bangladesh's dynamic coastal regions and sea-level rise. *Climate risk management*, *1*, pp.51-62.

[18] Alam, M.S. and Uddin, K., 2013. A study of morphological changes in the coastal areas and offshore islands of Bangladesh using remote sensing. *American Journal of Geographic Information System*, *2*(1), pp.15-18.

[19] Islam, M.A; Majlis, A.B.K and Rashid, M.B., 2012. *Changing Face of Bangladesh Coast.* Geological Survey of Bangladesh, Dhaka.

[20] Daily Star. Sandwip-Urir Char-Noakhali Cross Dam for Long-Term Food Security. April 26, 2008. Available online: (http://archive.thedailystar.net/newDesign/news-details.php?nid=33780) (Accessed on 27 June 2017).

[21] Moon Daily. Bangladesh gaining land, not losing: scientists. July 30, 2008. Available online:(https://www.moondaily.com/reports/Bangladesh_gaining_land_not_losing_scientists_999.html) (Accessed on 5 October 2018).

[22] Sanjay, C. and Sakhuja, V., 2015. Climate Change and the Bay of Bengal: Evolving Geographies of Fear and Hope. *ISEAS-Yusoflshak Institute*.

[23] Islam, M., Hossain, M. and Murshed, S., 2015. Assessment of coastal vulnerability due to sea level change at Bhola Island, Bangladesh: using geospatial techniques. *Journal of the Indian Society of Remote Sensing*, *43*(3), pp.625-637.

[24] Sarwar, M., Mahabub, G. and Woodroffe, C.D., 2013. Rates of shoreline change along the coast of Bangladesh. *Journal of Coastal Conservation*, *17*(3), pp.515-526.

[25] Aljazeera. The 'ground zero' of climate change: Bangladesh's Bhola Island succumbs to climate change displacing thousand. December 7, 2009. Available online: (https://www.aljazeera.com/focus/climatesos/2009/10/2009101011512667509.html) (Accessed on 15 December 2018).

[26] Li, W., Du, Z., Ling, F., Zhou, D., Wang, H., Gui, Y., Sun, B. and Zhang, X., 2013. A comparison of land surface water mapping using the normalized difference water index from TM, ETM+ and ALI. *Remote Sensing*, *5*(11), pp.5530-5549.

[27] Chander, G., Markham, B.L. and Helder, D.L., 2009. Summary of current radiometric calibration coefficients for Landsat MSS, TM, ETM+, and EO-1 ALI sensors. *Remote Sensing of Environment*, *113*(5), pp.893-903.

[28] Jiang, Z., Qi, J., Su, S., Zhang, Z. and Wu, J., 2012. Water body delineation using index composition and HIS transformation. *International Journal of Remote Sensing*, *33*(11), pp.3402-3421.

[29] Ouma, Y.O. and Tateishi, R., 2006. A water index for rapid mapping of shoreline changes of five East African Rift Valley lakes: an empirical analysis using Landsat TM and ETM+ data. *International Journal of Remote Sensing*, *27*(15), pp.3153-3181.

[30] McFeeters, S.K., 1996. The use of the Normalized Difference Water Index (NDWI) in the delineation of open water features. *International Journal of Remote Sensing*, *17*(7), pp.1425-1432.

[31] Xu, H., 2006. Modification of normalised difference water index (NDWI) to enhance open water features in remotely sensed imagery. *International Journal of Remote Sensing*, *27*(14), pp.3025-3033.

[32] Jain, S.K., Saraf, A.K., Goswami, A. and Ahmad, T., 2006. Flood inundation mapping using NOAA AVHRR data. *Water Resources Management*, *20*(6), pp.949-959.

[33] Lu, S., Wu, B., Yan, N. and Wang, H., 2011. Water body mapping method with HJ-1A/B satellite imagery. *International Journal of Applied Earth Observation and Geoinformation*, *13*(3), pp.428-434.

[34] Campos, J.C., Sillero, N. and Brito, J.C., 2012. Normalized difference water indexes have dissimilar performances in detecting seasonal and permanent water in the Sahara–Sahel transition zone. *Journal of Hydrology*, *464*, pp.438-446.

[35] Bai, J., Chen, X., Li, J., Yang, L. and Fang, H., 2011. Changes in the area of inland lakes in arid regions of central Asia during the past 30 years. *Environmental Monitoring and Assessment*, *178*(1), pp.247-256..

[36] Karsli, F., Guneroglu, A. and Dihkan, M., 2011. Spatio-temporal shoreline changes along the southern Black Sea coastal zone. *Journal of Applied Remote Sensing*, *5*(1), p.053545.

[37] Du, Z., Bin, L., Ling, F., Li, W., Tian, W., Wang, H., Gui, Y., Sun, B. and Zhang, X., 2012. Estimating surface water area changes using time-series Landsat data in the Qingjiang River Basin, China. *Journal of Applied Remote Sensing*, *6*(1), p.063609.

[38] Ji, L., Zhang, L. and Wylie, B., 2009. Analysis of dynamic thresholds for the normalized difference water index. *Photogrammetric Engineering & Remote Sensing*, *75*(11), pp.1307-1317.

[39] Otsu, N., 1979. A threshold selection method from gray-level histograms. *IEEE Transactions on Systems, Man, and Cybernetics*, *9*(1), pp.62-66.

[40] Sun, Q.B., Su, Y.Y., Ma, J. and Tan, M., 2011. Analysis of shoreline changes based on remote sensing in Changxing Island, Liaoning Province. *Marine Environmental Science*, *30*(3).

[41] Zeinali, S., Talebbeydokhti, N. and Dehghani, M., 2020. Spatiotemporal shoreline change in Boushehr Province coasts, Iran. *Journal of Oceanology and Limnology*, *38*(3), pp.707-721.

[42] Mikhailov, V.N. and Dotsenko, M.A., 2007. Processes of delta formation in the mouth area of the Ganges and Brahmaputra rivers. *Water Resources*, *34*(4), pp.385-400.

Appendix A

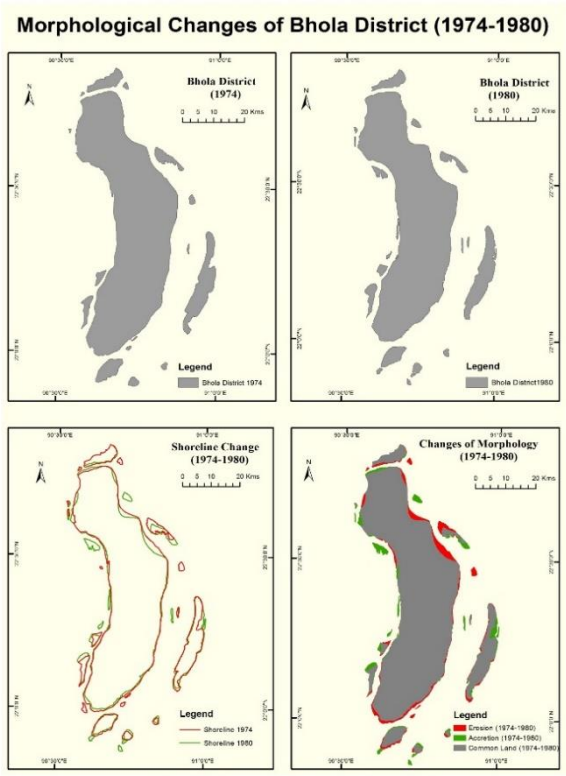

Fig. A1 Changes in Shoreline and Area of Bhola District in 1974 and 1980

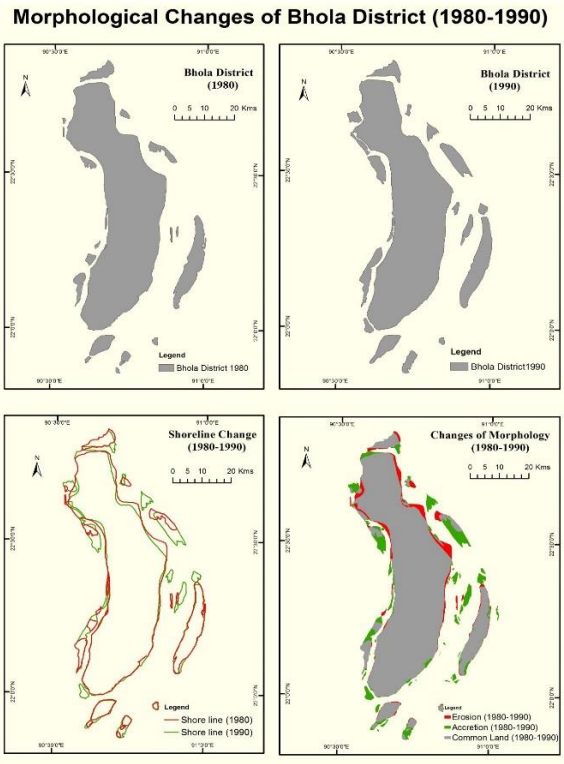

Fig. A2 Changes in Shoreline and Area of Bhola District in 1980 and 1990

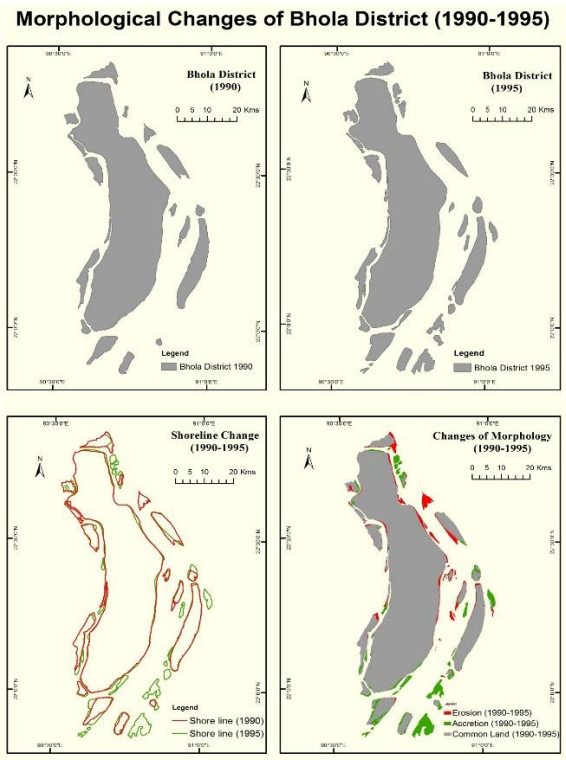

Fig. A3 Changes in Shoreline and Area of Bhola District in 1990 and 1995

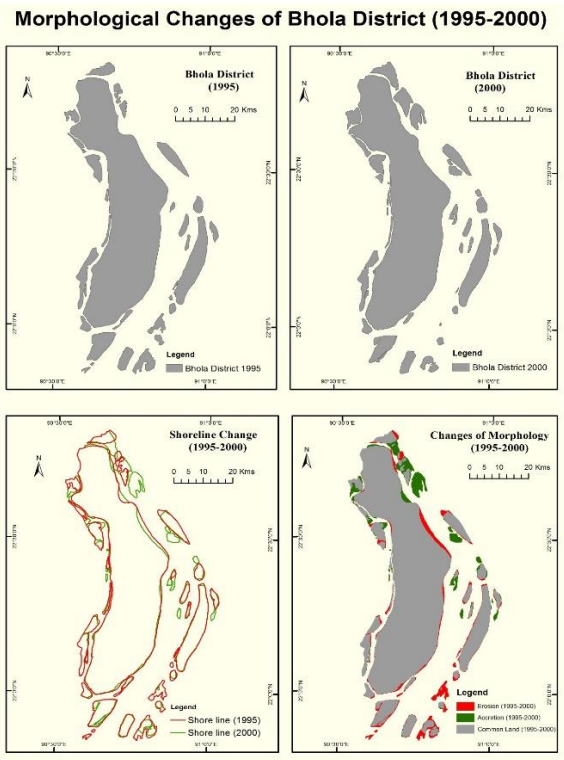

Fig. A4 Changes in Shoreline and Area of Bhola District in 1995 and 2000

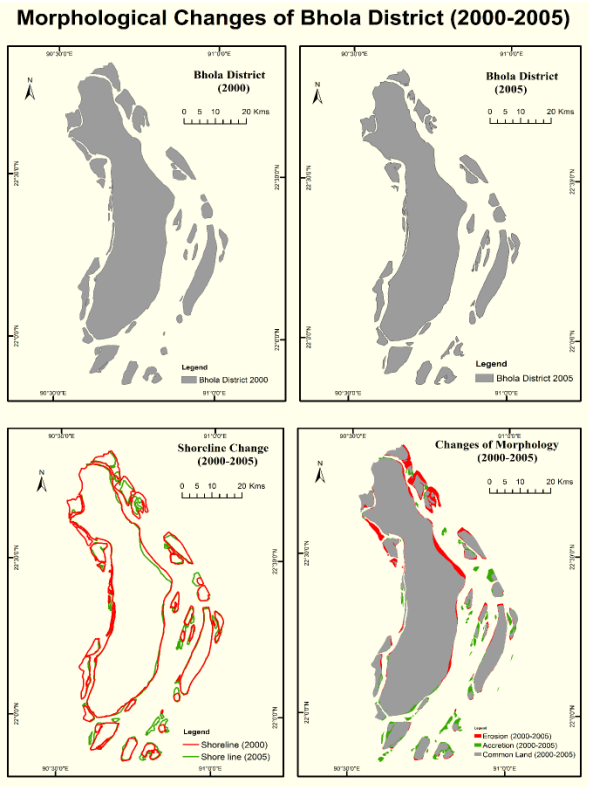

Fig. A5 Changes in Shoreline and Area of Bhola District in 2000 and 2005

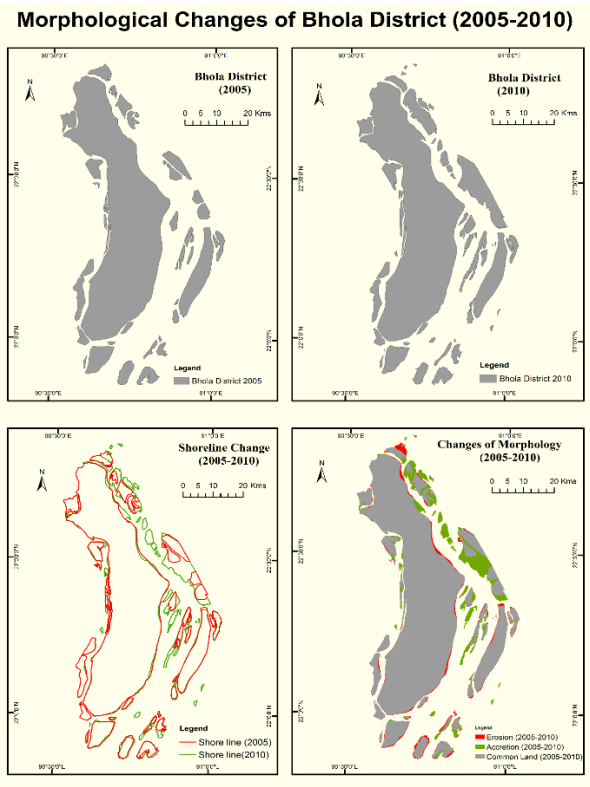

Fig. A6 Changes in Shoreline and Area of Bhola District in 2005 and 2010.

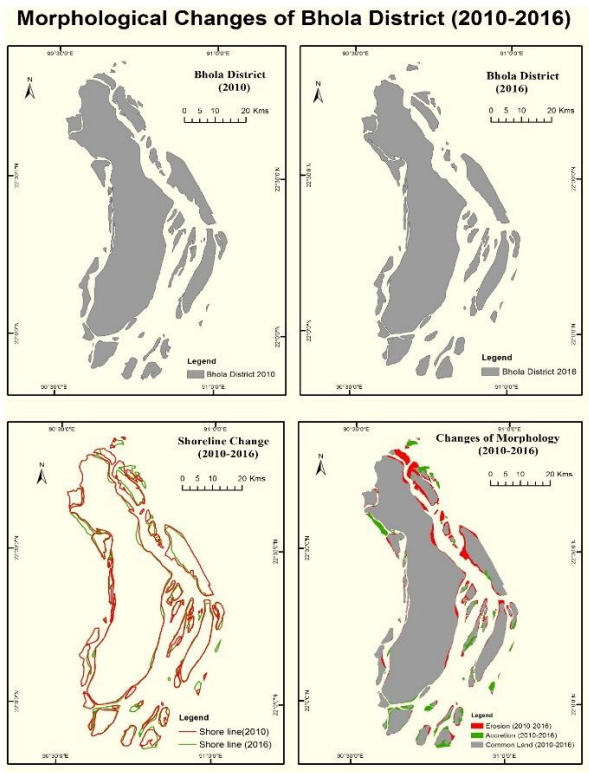

Fig. A7 Changes in Shoreline and Area of Bhola District in 2010 and 2016.

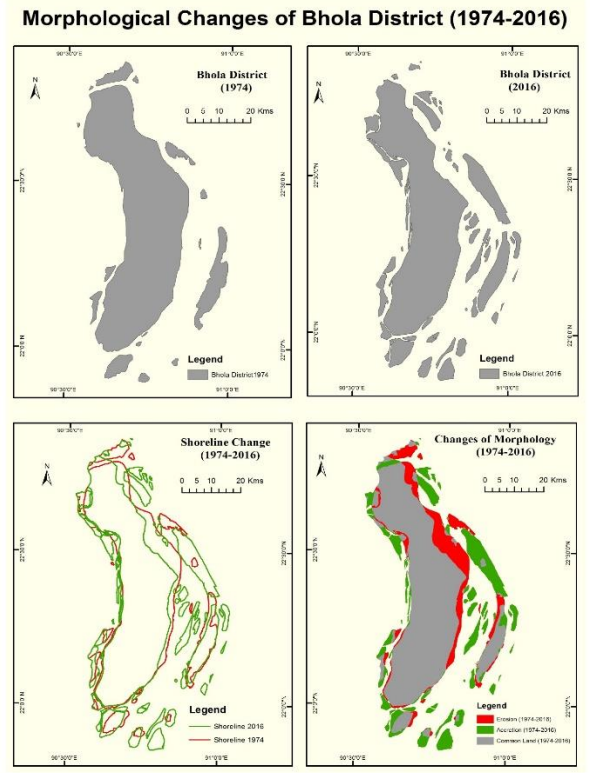

Fig. A8 Changes in Coastal Morphology of Bhola District from 1974 to 2016.

Appendix B

Table B1 Satellite imageries used in the study

Serial No	Satellite & Sensor	Acquisition Date	Path	Row	Spatial Resolution
1.	Landsat MSS	1974-01-10	147	044	60
2.	Landsat MSS	1980-01-15	147	044	60
3.	Landsat TM	1990-2-24	137	044	30
4.	Landsat TM	1995-01-21	137	044	30
5.	Landsat TM	2000-01-19	137	044	30
6.	Landsat TM	2005-01-19	137	044	30
7.	Landsat TM	2010-01-30	137	044	30
8.	Landsat OLI-TIRS	2016-01-15	136	044	30

Table B2 Image indices used in the study

Year	Sensor	Index	Formula
1974	MSS	NDWI	$\rho IR+(\rho Green+.0001)*100$
1980	MSS	NDWI	$\rho IR+(\rho Green+.0001)*100$
1990	TM	NDWI	$(\rho Green - \rho NIR) / (\rho Green + \rho NIR)$
1995	TM	NDWI	$(\rho Green - \rho NIR) / (\rho Green + \rho NIR)$
2000	TM	NDWI	$(\rho Green - \rho NIR) / (\rho Green + \rho NIR)$
2005	TM	NDWI	$(\rho Green - \rho NIR) / (\rho Green + \rho NIR)$
2010	TM	NDWI	$(\rho Green - \rho NIR) / (\rho Green + \rho NIR)$
2016	OLI	MNDWI	$(\rho Green - \rho SWIR) / (\rho Green + \rho SWIR)$

Table B3 Shoreline and Area of Bhola District in 1974 and 1980

Item/Year	1974	1980
Mainland Shore Line (km)	224.406	228.37
Total Shore Line (km)	507.017	580.56
Mainland Area (km^2)	1571.02	1515.68
Total Area (km^2)	1846.754	1814.74

Table B4 Change in Shoreline and Area of Bhola District in 1974 and 1980

Item/ Interval of Year	1974-1980
Total Shore line Change (km)	73.54
Mainland Shore line Change (km)	3.9
Total Common Area (km^2)	1728.08
Mainland (Common Area (km^2)	1500.06
Total Erosion (km^2)	118.67
Mainland Erosion (km^2)	70.96
Total Accretion (km^2)	86.66
Mainland Accretion (km^2)	15.61
Total Net Loss/Gain (km^2)	-32.01
Mainland Net Loss/Gain (km^2)	-55.35

Table B5 Shoreline and Area of Bhola District in 1980 and 1990

Item/Year	**1980**	**1990**
Mainland Shore Line (km)	228.37	239.05
Total Shore Line (km)	580.56	699.53
Mainland Area (km^2)	1515.68	1447.43
Total Area (km^2)	1814.74	1880.33

Table B6 Change in Shoreline and Area of Bhola District in 1980 and 1990

Item/ Interval of Year	1980-1990
Total Shore line Change (km)	118.97
Mainland Shore line Change (km)	10.68
Total Common Area (km^2)	1704.26
Mainland Common Area (km^2)	1427.33
Total Erosion (km^2)	109.52
Mainland Erosion (km^2)	88.35
Total Accretion (km^2)	211.56
Mainland Accretion (km^2)	20.09
Total Net Loss/Gain (km^2)	102.04
Mainland Net Loss/Gain (km^2)	68.26

Table B7 Shoreline and Area of Bhola District in 1990 and 1995

Item/Year	**1990**	**1995**
Mainland Shore Line (km)	239.05	222.83
Total Shore Line (km)	699.53	856.28
Mainland Area (km^2)	1447.43	1435.26
Total Area (km^2)	1880.33	1974.98

Table B8 Change in Shoreline and Area of Bhola District in 1990 and 1995

Item/ Interval of Year	1990-1995
Total Shore line Change (km)	+156.75
Mainland Shore line Change (km)	-16.17
Total Common Area (km^2)	1820.12
Mainland Common Area (km^2)	1422.37
Total Erosion (km^2)	97.28
Mainland Erosion (km^2)	25.05
Total Accretion (km^2)	155.17
Mainland Accretion (km^2)	12.88
Total Net Loss/Gain (km^2)	+57.89
Mainland Net Loss/Gain (km^2)	-12.17

Table B9 Shoreline and Area of Bhola District in 1995 and 2000

Item/Year	**1995**	**2000**
Mainland Shore Line (km)	222.83	234.62
Total Shore Line (km)	856.28	914.58
Mainland Area (km^2)	1435.26	1402.43
Total Area (km^2)	1974.98	1964.84

Table B10 Change in Shoreline and Area of Bhola District in 1995 and 2000

Item/ Interval of Year	1995-2000
Total Shore line Change (km)	+58.3
Mainland Shore line Change (km)	+11.79
Total Common Area (km^2)	1834.19
Mainland Common Area (km^2)	1389.42
Total Erosion (km^2)	140.98
Mainland Erosion (km^2)	45.83
Total Accretion (km^2)	131.40
Mainland Accretion (km^2)	13.01
Total Net Loss/Gain (km^2)	-9.58
Mainland Net Loss/Gain (km^2)	-32.82

Table B11 Shoreline and Area of Bhola District in 2000 and 2005

Item/Year	**2000**	**2005**
Mainland Shore Line (km)	234.62	231.14
Total Shore Line (km)	914.58	962.04
Mainland Area (km^2)	1402.43	1370.18
Total Area (km^2)	1964.84	1921.22

Table B12 Change in Shoreline and Area of Bhola District in 2000 and 2005

Item/ Interval of Year	2000-2005
Total Shore line Change (km)	+47.46
Mainland Shore line Change (km)	-3.48
Total Common Area (km^2)	1830.62
Mainland Common Area (km^2)	1360.71
Total Erosion (km^2)	134.22
Mainland Erosion (km^2)	41.72
Total Accretion (km^2)	90.60
Mainland Accretion (km^2)	9.48
Total Net Loss/Gain (km^2)	-43.62
Mainland Net Loss/Gain (km^2)	-32.24

Table B13 Shoreline and Area of Bhola District in 2005 and 2010

Item/Year	**2005**	**2010**
Mainland Shore Line (km)	231.14	235.73
Total Shore Line (km)	962.04	1109.34
Mainland Area (km^2)	1370.18	1357.94
Total Area (km^2)	1921.22	2062.34

Table B14 Change in Shoreline and Area of Bhola Island in 2005 and 2010

Item/ Interval of Year	2005-2010
Total Shore line Change (km)	+147.3
Mainland Shore line Change (km)	+4.59
Total Common Area (km^2)	1847.00
Mainland Common Area (km^2)	1344.83
Total Erosion (km^2)	74.21
Mainland Erosion (km^2)	25.35
Total Accretion (km^2)	215.33
Mainland Accretion (km^2)	13.10
Total Net Loss/Gain (km^2)	+141.12
Mainland Net Loss/Gain (km^2)	-12.25

Table B15 Shoreline and Area of Bhola Island in 2010 and 2016

Item/Year	**2010**	**2016**
Mainland Shore Line (km)	235.73	248.25
Total Shore Line (km)	1109.34	1117.99
Mainland Area (km^2)	1357.94	1328.36
Total Area (km^2)	2062.34	2001.61

Table B16 Change in Shoreline and Area of Bhola Island in 2010 and 2016

Item/ Interval of Year	2010-2016
Total Shore line Change (km)	+8.65
Mainland Shore line Change (km)	+12.52
Total Common Area (km^2)	1893.91
Mainland Common Area (km^2)	1322.90
Total Erosion (km^2)	168.42
Mainland Erosion (km^2)	35.03
Total Accretion (km^2)	107.70
Mainland Accretion (km^2)	5.46
Total Net Loss/Gain (km^2)	-60.72
Mainland Net Loss/Gain (km^2)	-29.57

Table B17 Shoreline and Area of Bhola Island in 1974 and 2016

Item/Year	Shore line (km)	Area (Sq. km)
1974	507.017	1846.75
1980	580.559	1814.74
1990	699.53	1880.33
1995	856.28	1974.98
2000	914.58	1964.84
2005	962.04	1921.22
2010	1109.34	2062.34
2016	1117.99	2001.61

Table B18 Change in Shoreline and Area of Bhola District in 1974 to 2016

Type/Interval of year	Shore line Change (km)	Common Area (Sq. km)	Erosion (Sq. km)	Accretion (Sq. km)	Net Loss/Gain (Sq. km)
1974-1980	+73.54	1728.08	118.67	86.66	-32.01
1980-1990	+118.97	1704.26	109.52	211.56	+102.04
1990-1995	+156.75	1820.12	97.28	155.17	+57.89
1995-2000	+58.3	1834.19	140.98	131.40	-9.58
2000-2005	+47.46	1830.62	134.22	90.60	-43.62
2005-2010	+147.3	1847.00	74.21	215.33	+141.12
2010-2016	+8.65	1893.91	168.42	107.70	-60.72
1974-2016	+610.98	1503.46	343.30	498.15	+154.85

SciEn
Journal of Engineering Advancements Vol. 03(03) 2022, pp 91-95 https://doi.org/10.38032/jea.2022.03.003

Characteristics of Ion Beam for Various Gases in a Spherical Plasma Focus Device

*M A Malek**

Physics Discipline, Khulna University, Khulna-9208, Bangladesh

Received: August 28, 2022, Revised: September 17, 2022, Accepted: September 18, 2022, Available Online: September 24, 2022

ABSTRACT

This study presents the computed ion beam properties (flux, fluence, and energy) of argon, neon, and nitrogen gases with pressure variation in the spherical plasma focus device, KPU200 SPF. Numerical experiments are performed using the Lee code (version: RADPFV5.16FIB) with the gases in the pressure range of 0.10 - 19 Torr. The electrode geometry has been obtained by applying the 'equivalent straightened electrode' technique. The computed results for each of the gases show that the ion beam properties increase with the increase in pressure until reach a peak value and then start to reduce with further pressure increase. The peak ion beam flux (ions m^{-2} s^{-1}), fluence (ions.m^{-2}), and energy (J) from heavier argon pinch plasma are found as 5.31×10^{27} at 2 Torr, 8.93×10^{20} at 3.5 Torr, and 3.46×10^{4} at 3 Torr, respectively which are the utmost values from neon and nitrogen gases. Significant correlations of pinch radius and duration, effective charge number, and induced voltage with these ion beam properties are noticed and discussed in this paper. The obtained results of this study are compared with those of the NX2 plasma focus device that makes the consistency of the present research work.

Keywords: Spherical Plasma Focus, Lee Code, Plasma Pinch, Ion Beam, Flux, Fluence.

1 Introduction

A dense plasma focus (DPF) device produces super-dense (~1016 - 1019 cm^{-3}), super-hot (~1 keV) plasma by self-generated electromagnetic compression [1]. It is a non-radioactive powerful source of ion beam (~0.01 - 100 MeV), electron beam (~0.01 - 1 MeV), pulsed fusion neutron (~2.45 - 14 MeV), soft (0.1 - 10 keV), and hard (~10 - 1000 keV) X-rays [2]-[3]. The first models of DPF are invented in the 1960s by Mather in the USA [4] and Filippov in USSR [5]-[6]. The operation principles of these two types are the same but differ in the aspect ratio (ratio of anode length to its radius) of their electrode geometry. A spherical plasma focus (SPF) having two concentric spherical electrodes (anode and cathode) is a special combination of the Mather and Filippov type of device.

A plasma focus is enclosed within a chamber, consisting of two co-axial electrodes separated by an insulator, powered by a high voltage capacitor bank. The filling gas starts to discharge across the electrodes due to the breakdown voltage and produces a plasma sheath (PS) over the surface of the insulator. This PS is then liftoff and accelerated by the axial Lorentz force (LF) across the coaxial electrodes. When it reaches at anode end, the radial LF pushes the PS towards the anode top forming a high-temperature, high-dense, very thin, and small shape plasma column known as pinch. This dense and hot plasma into the pinch column during its stagnation in front of the anode top is the source of radiation. Finally, it is collapsed by un-stabilities forming the voltage works to accelerate the electron and ion beam in opposite directions. The emitted high-energy ion and electron beams from pinch plasma in a DPF have been used in different fields such as nano-material and device fabrication [7], thin film deposition [8], surface modification [9], thermal surface treatment [10], ion-assisted coating [11], ion implication, and production of short-lived radioisotopes [12] including plasma processing. Many efforts have been made in experimental studies of applications of fast ion and electron beams from various DPF devices [13]. Most of the experiments in ion beam detection were performed with deuterium to investigate neutron production and deuteron acceleration during plasma focus discharge. The energy transfer mechanism from magnetized plasma to ions and electrons is unclear till today [14]. Therefore, ion beam characterization is not only very important for understanding the production mechanism of high-energy ions but also plays an important role in optimizing, upgrading, and modifying DPF devices for their specific application in different fields [15]-[17].

The Lee code [18]-[20] is one of the famous tools for numerical modeling and experiments [21] of a plasma focus for computing ion beam properties (flux, fluence, density, and energy) [22]-[23]. Ion beam characteristics have been studied in Mather and Flippov type devices using this code. The KPU200 is a spherical plasma focus device which is designed mainly for neutron production [24]-[25]. The electrode (anode & cathode) geometry, static inductance, operating voltage, and pressure change of different gases were studied for neutron and ion production [26]-[27], X-ray emissions (continuum and line radiations) [28]-[30] in this device. So far, no one has computed ion beam properties in this device.

In this paper, I study some characteristics such as peak discharge current (I_{peak}), pinch current (I_{pinch}) and radius (r_p), effective charge number, ion accelerating induced voltage taken as diode voltage which are directly used to calculate ion beam properties with pressure change in various gases including nitrogen (N_2), neon (Ne), and argon (Ar) from the spherical plasma focus device KPU200 SPF using the Lee code.

In section 2, I present a brief description of the operation including the calculating equations of ion beam flux, fluence, and energy in the Lee code, and the method of numerical experiments is given in section 3. In section 4, the results and discussions are presented and finally, conclusions are given in section 4.

2 The Lee Code

Around all of the main phases of discharge in a DPF can be simulated using the five-phase Lee code [31]. The plasma focus

*Corresponding Author Email Address: malek@ku.ac.bd

dynamics, thermodynamics, and radiations are coupled with the electrical circuit by this code. The effects of gas ionization, discharge by shock-wave heating in radial phase just before the formation of stable pinch, plasma heating in pinch column due to the ohmic for Spitzer and anomalous resistivity, and micro-instability development are included in the code. It shows the consistency of mass, energy, charge, and momentum. This code can be used in the experimental interpretation and design of a plasma focus [1]. It couples the radiations (bremsstrahlung, line, and recombination) with the dynamics of plasma pinch compression. In the code, the transition from volumetric to surface emission, self-absorption in plasma, fusion neutron production by beam-target as well as thermonuclear methods are also considered.

The discharge current waveform getting from a DPF operation can be considered a significant indicator of realistic simulation and analyze all of the gross properties of a plasma focus. Using the Lee code, the important information (axial and radial phase dynamics and radiations) of a device can be traced quickly from the current flow through the plasma sheath [19]. However, when the computed discharge current waveform is fitted with the measured one, the computed outputs of the code provide the following realistic data: the dynamics and energy in each phase, the geometry of pinch column, densities and temperatures, radiations, neutron yields, and ion beam.

Therefore, to simulate a specific DPF device by this code, the measured discharge current waveform of the device is to be picked out either from the published article or from a laboratory experiment.

2.1 The Ion Beam Flux, Fluence, and Energy Equations

To study the properties of the emitted ion beam from the pinch plasma in a DPF, the ion beam flux equation has been derived and inserted into the Lee code [19], [32]-[33]. At the time of simulation, the flux of the ion beam is estimated in the code with the following equation [22]:

$$Flux\ (ions\ m^{-2}\ s^{-1}) = 2.75 \times 10^{15} \left(\frac{f_e}{\sqrt{MZ_{eff}}}\right)\left(\frac{ln[b/r_p]}{r_p^2}\right)\frac{I_{pinch}^2}{\sqrt{U}} \quad (1)$$

Here, f_e is the fraction of pinch inductive energy (PIE) converted into the beam kinetic energy (BKE) and it is equivalent to an ion beam energy of (3 - 6) % E_0 (operating energy of plasma focus). To study the pinch dimensional-temporal relationships and the neutron yield data [22]-[23], the value of f_e has been estimated as 0.14 [23], M is the ion mass number, Z_{eff} is the number of effective charge of ion in the pinch, b is the cathode radius, the pinch radius, the pinch current are to be known. The ion accelerating voltage is taken as diode voltage U = $3V_{max}$, which is obtained from data fitting, where V_{max} is the maximum induced voltage of the pre-pinch radial phase. For the case of strong radiative collapse, it generates an additional induced voltage and, in such cases, $U = V_{max}^*$ [22]-[23].

The ion fluence is defined as the number of ions per unit cross-section of the pinch column. Since the beam emits from the focus pinch with slight divergence, fluence is the best way to characterize the ion beam. It is calculated as the flux multiplied by the pulse duration of the ion beam (τ). From considering approximate scaling [23]: $\tau = 10^{-6} z_p$ where, z_p is the pinch column length. Thus:

$$Fluenc\ (ions\ m^{-2}) = 2.75 \times 10^9 \left(\frac{f_e}{\sqrt{MZ_{eff}}}\right)\left(\frac{ln[b/r_p]}{r_p^2}\right) \quad (2)$$

Ion beam energy (E) is estimated by using the following equation:

$$E(J) = Z_{eff} U \times Number\ of\ ion\ in\ beam \quad (3)$$

The code computes the values of Z_{eff}, r_p, pinch duration, I_{pinch}, and U along with the ion beam flux followed by ion beam fluence and energy.

3 Method used in Numerical Experiments

In this work, I use the Spherical Plasma Focus, KPU200 SPF for the numerical studies of the ion beam flux, fluence, and energy in various gases including N_2, Ne, and Ar with pressure variation. The electrode geometry has been obtained by applying the 'equivalent straightened electrode' technique to this SPF device [24]-[25], [34]. The Lee code is configured to conduct the numerical experiments using the following standard parameters of this device [34]-[35]:

1. Bank parameters: Static inductance (L_0) = 36 nH, Bank capacitance (C_0) = 432 µF, and short-circuited resistance of the discharge circuit (r_0) = 1.2 mΩ.
2. Tube parameters: Cathode radius (b) = 15 cm, Anode radius (a) = 8 cm and Anode length (z_0) = 21.3 cm.
3. Operating parameters: Bank charging voltage (V_0) = 25 kV, Deuterium-Tritium (D-T) gas: (MW = 5, A =1 and At-1 mol-2 = 2) and Operating pressure (P_0) = appropriate range of pressure (Torr) in each gas.
4. Model parameters: Mass swept-up factor (f_m) = 0.0635 and plasma current factor (f_c) = 0.7 in the axial phase, Mass swept-up factor (f_{mr}) = 0.14 and plasma current factor (f_{cr}) = 0.7 in the radial phase.

These model parameters have been obtained by fitting the computed current trace with the measured one at 14.3 Torr D-T in KPU200 SPF [33]-[34]. Though, this set of model parameters is expected to vary slightly within a wide range of gases, even in a pressure range for a given gas [36]-[37] these are kept constant in our present numerical experiments for different gases in the pressure range of 0.1 – 19 Torr.

4 Results and Discussion

4.1 Ion beam Flux for Various Gases

The high-energy ions from plasma focus are applied for a different type of material processing. The operating pressure of Ar, Ne, and N_2 gases are varied and the corresponding flux, fluence, and energy of outgoing ion beam from pinch plasma in terms of I_{peak}, I_{pinch}, Z_{eff}, r_p, and U are obtained using the Eqs (1), (2), and (3) through the code. As an example, Table 1 presents the ion beam properties for Ar. This table shows that the peak discharge current (~1962 kA) at maximum pinch current (~773 kA) is found at 3.5 Torr whilst the Ar plasma goes to its 16th ionized state (Z_{eff} = 16) at 0.2 Torr. Also, I notice that the r_p gradually reduces with decreasing pressure up to 3.5 Torr and then gets its minimum value of 3.2 mm at 3.0 Torr. This reduced value remains unchanged up to 0.6 Torr after that it starts to increase again with pressure reduction.

Table 1 Change in ion beam properties with pressure variation of Ar plasma in KPU200 SPF.

P_0 (Torr)	I_{peak} (kA)	I_{pinch} (kA)	Z_{eff}	r_p ($\times 10^{-3}$ m)	U (kV)	Flux ($\times 10^{27}$ ions m^{-2} s^{-1})	Fluence ($\times 10^{20}$ ions.m^{-2})	E ($\times 10^4$ J)
10	1961.80	612.88	8.00	13.10	89.65	0.38	1.57	0.97
9	1943.30	650.79	8.00	11.55	98.20	0.56	2.15	1.13
8	1922.18	690.51	8.21	9.88	109.13	0.86	2.52	1.11
7	1897.70	720.48	8.48	8.53	122.66	1.22	3.28	1.25
6	1868.77	744.57	8.78	7.06	141.47	1.86	4.62	1.44
5	1833.65	762.26	9.10	5.55	170.97	3.03	6.82	1.65
4	1789.46	772.40	9.46	4.14	369.57	4.06	8.26	2.50
3.5	1762.43	772.99	9.66	3.53	558.07	4.71	8.93	3.03
3	1730.73	772.47	9.84	3.20	766.56	4.97	8.9	3.46
2.5	1692.62	766.59	9.91	3.20	661.90	5.25	8.78	2.97
2	1644.81	753.80	9.94	3.20	601.67	**5.31**	8.23	2.54
1.5	1578.03	731.04	9.94	3.20	678.63	4.71	6.43	2.24
1	1476.97	691.70	9.97	3.20	779.51	3.93	4.55	1.82
0.7	1384.71	653.73	10.39	3.20	629.59	3.82	3.97	1.34
0.2	1072.58	519.25	16.00	9.54	320.93	2.19	0.16	0.38
0.1	920.02	453.78	16.00	10.9	301.53	1.25	0.082	0.24

The diode voltage reaches its maximum value of 779.51 kV at 1.0 Torr. The flux curve of ions (m^{-2} s^{-1}) for Ar, Ne, and N_2 gases with pressure change is shown in Fig. 1.

The flux curve of Ar ions gradually increases with an increase in pressure to the maximum value of 5.31 × 1027 at 2 Torr and then reduces with further pressure increase.

The Ne curve has a value of 0.54 × 1027 at 1 Torr, rises sharply to a peak value of 4.78 × 1027 at 2.5 Torr, and then drops gradually. The N_2 curve shows the same trend with a lower peak flux value of 1.67 × 1027 at 4 Torr. During flux calculation, the pinch radii at the corresponding optimum pressure of Ar, Ne, and N_2 are found to be 3.2 mm, 4.69 mm, and 8.81 mm, respectively.

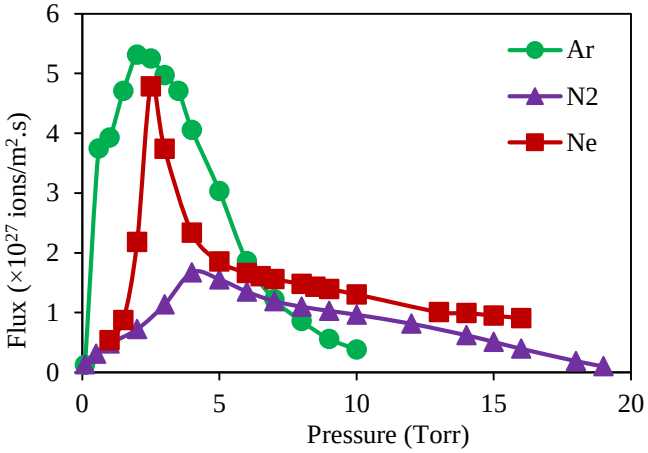

Fig. 1 Change in ion beam flux with pressure variation for Ar, Ne, and N_2 in KPU200 SPF.

This lowest value of pinch radii in Ar and Ne plasmas due to radiative collapse, produce the highest flux of ion beam compared to N_2 gas.

4.2 Ion Beam Fluence for Various Gases

The fluence in ions/m^2 for the various gases with pressure change is shown in Fig. 2. The curve shapes and the changing trend of fluence with pressure variation for various gases are comparable to the flux curves discussed in section 4.1. The peak values of the fluence are obtained as 8.93 ×1020 at 3.5 Torr Ar, 6.44 × 1020 at 2.5 Torr Ne, and 2.97 ×1020 at 4 Torr N_2. Noted, the optimum pressure and hence r_p for Ne and N_2 are similar to that for flux calculation.

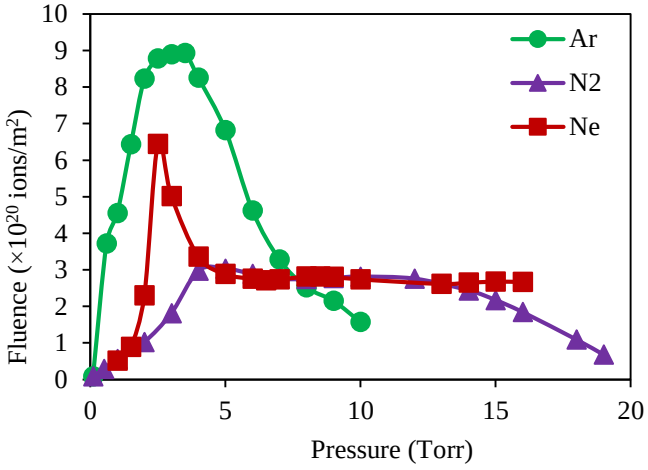

Fig. 2 Change in ion beam fluence with variation for Ar, Ne, and N_2 in KPU200 SPF.

At the optimum pressure, the pinch radius of Ar is found to be 3.53 mm which is quietly smaller than that of other gases. Also, the duration of the pinch (ion beam pulse duration) of Ar, Ne, and N_2 are computed as 190 ns, 144 ns, and 135 ns, respectively at their corresponding optimum pressure. Fluence is the flux multiplied by the estimated ion beam pulse duration. These two factors (the largest pulse duration and smallest pinch radius) enhance the fluence of Ar compared to Ne and N_2.

4.3 Ion Beam Energy for Various Gases

The ion beam energy rises with the increase in pressure until it reaches a high value and then reduces with further pressure increases as shown in Fig. 3.

In our present studies, the number of ions per shot and ion current along with ion beam energy is found in Ar plasma 2.86 ×

1016 and 252 kA with peak 3.46 × 104 J at 3 Torr, in Ne plasma 6.6 × 1016 and 430 kA with peak 1.83× 104 J at 8.5 Torr, and in N_2 plasma 9.14 × 1016 and 393 kA with peak 1.21 × 104 J at 6 Torr. Also, both of the Zeff and U(kV) are found as Ar(9.84 & 767), Ne(8 & 217), and N_2(5.74 & 144). That means the high atomic gases show a higher effective charge number and diode voltage than those of lighter gases. These are the reasons for greater ion beam energy for heavier gasses (reflection of Eq. (3)).

The computed results getting from the present study in KPU200 SPF are compared with those of NX2 [23] at similar pressures of Ar, Ne, and N_2 gases and are given in Table 2. The NX2 is a Mather type DPF device with operating energy of 2.7 kJ whilst its KPU200 SPF is 135 kJ. Due to this higher operating energy of this device, the I_{peak} and consequent I_{pinch} are almost 4-times higher for each of the gases. The variation trend of pinch properties such as z_p, r_p, V_{max}, Z_{eff}, and τ with gas are very similar in both devices.

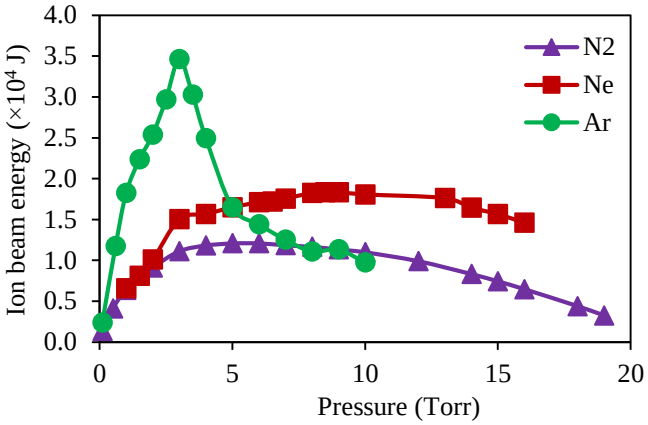

Fig. 3 Change in ion beam energy with variation for Ar, Ne, and N_2 in KPU200 SPF.

Table 2 Comparison of ion beam characteristics in NX2 [23] and KPU200 SPF.

DPF device	NX2	KPU200	NX2	KPU200	NX2	KPU200
Operating gas	Ar	Ar	Ne	Ne	N_2	N_2
P_0(Torr)	2	2	4	4	2	2
I_{peak}(kA)	406	1644.81	406	1644.76	395	1561.53
I_{pinch}(kA)	209	753.8	208	745.83	215	755.59
z_p(cm)	3.4	14.58	2.8	12.29	2.8	11.77
r_p(cm)	0.08	0.32	0.14	0.66	0.24	1.12
V_{max} (kV)	152	601.67	34	262.09	29	200.96
Z_{eff}	11	9.94	8	8	6.4	7
τ (ns)	30	154.87	25.2	144.07	25.6	141.48
Ion flux (×10^{27} ions/m^2 s)	14	**5.23**	6.6	**2.33**	3.2	**0.72**
Ion fluence (×10^{20} ions/m^2)	4.3	**8.23**	1.7	**3.36**	0.8	**1.02**
Ion beam energy (J)	207	**25400**	143	**15700**	13	**9100**

The obtained pinch radii in KPU200 SPF for different gases are very higher than those in NX2. According to Eq. (1), r_p has a strong effect (inversely proportional) on ion flux and this is because it in NX2 is higher than in the present SPF device for each gas whilst ion fluence is higher in KPU200 SPF because of its large pinch duration. The ion beam energy in this device is much higher due to its greater induced voltage than that of NX2. It is also observed that the variation trend of ion beam properties with change in pressure of these gases in both devices is very similar in nature. Finally, it is to be concluded that the obtained numerical results from my present studies are consistent that increasing the validation of this research work.

5 Conclusion

The electrode geometry of the spherical plasma focus device, KPU200 SPF has been obtained by applying the 'equivalent straightened electrode' technique to configure the Lee code. I use this code to characterize the ion beam flux (ions $m^{-2}s^{-1}$), fluence (ions/m^2), and energy (J) for Ar, Ne, and N_2 pinch plasmas with pressure variation in the DPF device. The computed results for each used gas indicate that all of these ion beam properties increase with the increase in pressure until reaching a peak value and then decrease with further pressure increase. The pinch radius of N_2 (8.81 mm) is about two times higher than that for Ar (3.2 mm) and Ne (4.69 mm). The lower values of pinch radii in Ar and Ne pinch plasmas cause radiative collapse and produce a higher ion beam flux in Ar(5.31 × 1027) and Ne(4.78 × 1027 at 2.5 Torr) than N_2 (1.67 × 1027 at 4 Torr). The pulse duration of Ar, Ne, and N_2 are found as 190 ns, 144 ns, and 135 ns, respectively, and the consequent peak fluences are found as 8.93 ×1020, 6.44 ×1020, and 2.97 ×1020, respectively. The Ar beam energy (3.46 × 104 J) is greater than Ne (0.83× 104 J) and N_2 (1.21 × 104 J) because of its higher values of the effective charge (9.84) and induced voltage (767 kV) generated by the collapse of pinch plasma.

The obtained results getting from this study in KPU200 SPF are compared with those of NX2 at similar pressures of Ar, Ne, and N_2. The variation trend of ion beam properties with change in pressure of these gases in both devices is very similar in nature which increases the validation of the results.

6 Acknowledgment

The author acknowledges the Physics discipline and Research cell, Khulna University for giving a sound environment and active support during this research work.

7 Conflict of Interest

The author declares that there is no conflict of interest regarding the publication of this article.

References

[1] Lee, S., Saw, S.H., Soto, L., Springham, S.V. and Moo, S.P., 2009. Numerical experiments on plasma focus neutron yield

versus pressure compared with laboratory experiments. *Plasma Physics and Controlled Fusion*, *51*(7), p.075006.

[2] Liu, M., 1996. *Soft X-rays from compact plasma focus* (Doctoral dissertation).

[3] Habibi, M., Amrollahi, R. and Etaati, G.R., 2010. Experimental study of hard X-ray emission with different anode tips in APF plasma focus device. *Journal of fusion energy*, *29*(1), pp.49-54.

[4] Filippov, N.V., Filippova, T.I. and Vinogradov, V.P., 1962. Dense high-temperature plasma in the region of non-cylindrical cumulation of Z-pinch. *Nucl. Fusion: Suppl*, p.577.

[5] Mather, J.W., 1964. Investigation of the high-energy acceleration mode in the coaxial gun. *The Physics of Fluids*, *7*(11), pp.S28-S34.

[6] Mather, J.W., 1965. Formation of a high-density deuterium plasma focus. *The Physics of Fluids*, *8*(2), pp.366-377.

[7] Saw, S.H., Damideh, V., Chong, P.L., Lee, P., Rawat, R.S. and Lee, S., 2014, August. A 160 kJ dual plasma focus (DuPF) for fusion-relevant materials testing and nano-materials fabrication. In *International Journal of Modern Physics: Conference Series* (Vol. 32, p. 1460322). The Authors.

[8] Hassan, M., Rawat, R.S., Lee, P., Hassan, S.M., Qayyum, A., Ahmad, R., Murtaza, G. and Zakaullah, M., 2008. Synthesis of nanocrystalline multiphase titanium oxycarbide (TiCxOy) thin films by UNU/ICTP and NX2 plasma focus devices. *Applied Physics A*, *90*(4), pp.669-677.

[9] Niranjan, R., Rout, R.K., Srivastava, R., Chakravarthy, Y., Mishra, P., Kaushik, T.C. and Gupta, S.C., 2015. Surface modifications of fusion reactor relevant materials on exposure to fusion grade plasma in plasma focus device. *Applied Surface Science*, *355*, pp.989-998.

[10] Ahmad, M., Al-Hawat, S. and Akel, M., 2013. Porous structure formation on silicon surface treated by plasma focus device. *Journal of Fusion Energy*, *32*(4), pp.471-478.

[11] Bhuyan, M., Mohanty, S.R., Rao, C.V.S., Rayjada, P.A. and Raole, P.M., 2013. Plasma focus assisted damage studies on tungsten. *Applied surface science*, *264*, pp.674-680.

[12] Niranjan, R., Rout, R.K., Tomar, B.S., Ramanjaneyulu, P.S., Paranjape, D.B. and Kaushik, T.C., 2018. Application of medium energy plasma focus device in study of radioisotopes. *Physics Letters A*, *382*(46), pp.3365-3368.

[13] Damideh, V., Chin, O.H., Saw, S.H., Lee, P.C.K., Rawat, R.S. and Lee, S., 2019. Characteristics of Fast ion beam in Neon and Argon filled plasma focus correlated with Lee Model Code. *Vacuum*, *169*, p.108916.

[14] Auluck, S., Kubes, P., Paduch, M., Sadowski, M.J., Krauz, V.I., Lee, S., Soto, L., Scholz, M., Miklaszewski, R., Schmidt, H. and Blagoev, A., 2021. Update on the scientific status of the plasma focus. *Plasma*, *4*(3), pp.450-669.

[15] Szydlowski, A., Banaszak, A., Bienkowska, B., Ivanova-Stanik, I.M., Scholz, M. and Sadowski, M.J., 2004. Measurements of fast ions and neutrons emitted from PF-1000 plasma focus device. *Vacuum*, *76*(2-3), pp.357-360.

[16] Akel, M., Salo, S.A., Saw, S.H. and Lee, S., 2014. Characterization of oxygen ion beams emitted from plasma focus. *Vacuum*, *110*, pp.54-57.

[17] Akel, M., Salo, S.A., Ismael, S., Saw, S.H. and Lee, S., 2017. Comparison of measured and computed beam ion current densities emitted from two 2 kJ plasma focus machines. *Vacuum*, *136*, pp.163-167.

[18] Lee, S., 2022. Radiative Dense Plasma Focus Computation Package: RADPF www.plasmafocus.net

[19] Lee, S., 2014. Plasma focus radiative model: Review of the Lee model code. *Journal of Fusion Energy*, *33*(4), pp.319-335.

[20] Lee, S. and Saw, S.H., 2017. The plasma focus—numerical experiments, insights and applications. In *Plasma Science and Technology for Emerging Economies* (pp. 113-232). Springer, Singapore.

[21] Scholz, M. and Ivanova-Stanik, I.M., 2000. Initial phase in plasma focus device—model and computer simulation. *Vacuum*, *58*(2-3), pp.287-293.

[22] Lee, S. and Saw, S.H., 2012. Plasma focus ion beam fluence and flux—Scaling with stored energy. *Physics of Plasmas*, *19*(11), p.112703.

[23] Lee, S. and Saw, S.H., 2013. Plasma focus ion beam fluence and flux—For various gases. *Physics of Plasmas*, *20*(6), p.062702.

[24] Maslov, V.V., Rumyantsev, V.G., Basmanov, V.F., Budnikov, D.V., Garin, A.V., Drozdov, I.Y., Ershov, D.A., Korkin, D.S., Makeev, N.G., Molodtsev, D.A. and Moskvin, N.I., 2014. A KPU-200 movable capacitor installation. *Instruments and Experimental Techniques*, *57*(2), pp.131-134.

[25] Zavyalov, N.V., Maslov, V.V., Rumyantsev, V.G., Drozdov, I.Y., Ershov, D.A., Korkin, D.S., Molodtsev, D.A., Smerdov, V.I., Falin, A.P. and Yukhimchuk, A.A., 2013. A source with a 1013 DT neutron yield on the basis of a spherical plasma focus chamber. *Plasma Physics Reports*, *39*(3), pp.243-247.

[26] Ay, Y., Al-Halim, M.A.A. and Bourham, M.A., 2016. MHD simulation for neutron yield, radiations and beam-ion properties in the spherical plasma focus. *Journal of Fusion Energy*, *35*(2), pp.407-414.

[27] Yaşar, A.Y., 2020. Neutron and Ion Production with Various Applied Voltages in Spherical Plasma Focus. *Dicle Üniversitesi Mühendislik Fakültesi Mühendislik Dergisi*, *11*(1), pp.135-141.

[28] Ay, Y., 2021. Spherical plasma focus operated with nitrogen and neon gases for soft x-rays (bremsstrahlung radiation, line radiation, and radiative recombination). *Plasma Physics and Controlled Fusion*, *63*(7), p.075011.

[29] Ay, Y., 2019. Effect of the cathode radius on plasma dynamics and radiation emissions in a spherical plasma focus device. *Physics of Plasmas*, *26*(10), p.102506.

[30] Ay, Y., 2021. Neon soft x-ray yield optimization in spherical plasma focus device. *Plasma Physics and Controlled Fusion*, *63*(11), p.115009.

[31] Lee, S., 2014. Radiative Dense Plasma Focus Computation Package: RADPF, 2010 http://www. plasmafocus. net. http://www. plasmafocus. net/IPFS/modelpackage/File1RADPF. htm. http://www. plasma focus. net/IPFS/modelpackage/File2Theory. pdf. http://www. plasma focus. net/IPFS/modelpackage. *UPF. htm*.

[32] Akel, M., Salo, S.A., Saw, S.H. and Lee, S., 2014. Properties of ion beams generated by nitrogen plasma focus. *Journal of Fusion Energy*, *33*(2), pp.189-197.

[33] Akel, M., Salo, S.A., Saw, S.H. and Lee, S., 2014. Ion beam features produced by two plasma focus machines operated with different gases. *IEEE Transactions on Plasma Science*, *42*(9), pp.2202-2206.

[34] Lee, S. and Saw, S.H., 2017. The plasma focus—numerical experiments, insights and applications. In *Plasma Science and Technology for Emerging Economies* (pp. 113-232). Springer, Singapore.

[35] Saw, S. H., 2012. Plasma focus numerical experiments and BORA—2370-6 school and training course on dense magnetized plasma as a source of ionizing radiations, their diagnostics and applications, *Abdus Salam International Centre for theoretical physics*, 8–12 Oct 2012.

[36] Akel, M., Ismael, S., Lee, S., Saw, S.H. and Kunze, H.J., 2017. Numerical experiments on the PF1000 plasma focus device operated with nitrogen and oxygen gases. *Modern Physics Letters B*, *31*(16), p.1750167.

[37] Lee, S., Saw, S.H. and Ali, J., 2013. Numerical experiments on radiative cooling and collapse in plasma focus operated in krypton. *Journal of Fusion Energy*, *32*(1), pp.42-49.

SciEn
Journal of Engineering Advancements Vol. 03(03) 2022, pp 96-103 https://doi.org/10.38032/jea.2022.03.004

A Study of Large-eddy Simulation using Statistical and Machine Learning Techniques

*Mohammed Khalid Hossen**

Department of Computer Science and Engineering, Sylhet Agricultural University, Sylhet, Bangladesh

Received: July 23, 2022, Revised: September 09, 2022, Accepted: September 09, 2022, Available Online: September 26, 2022

ABSTRACT

The numerical solution of Navier-Stokes (N-S) equations has been found useful in various disciplines during its development, especially in recent years. However, a large-eddy simulation method has been developed to model the subgrid-scale dissipation rate by closing the Navier-Stokes equations. Because the instantaneous and time-averaged statistic characteristics of the subgrid-scale turbulent kinetic energy and dissipation have been studied by large eddy simulation. The purpose of this study is to check the statistical and machine learning of the subgrid-scale energy dissipation. As we know that the current turbulence theory states that the vortex stretching mechanism transports energy from large to small scales and leads to a high energy dissipation rate in a turbulent flow. Hence, a vortex-stretching-based subgrid-scale model is considered regarding the square of the velocity gradient to detect the playing role of the vortex stretching mechanism. The study in this article has shown a two-step process. Considering a posteriori statistic of the velocity gradient is analyzed through higher-order statistics and joint probability density function. Secondly, a machine learning approach is studied on the same data. The results of the vortex-stretching-based subgrid-scale model are then compared with the other two dynamic subgrid models, such as the localized dynamic kinetic energy equation model and the TKE-based Deardorff model. The results suggest that the vortex-stretching-based model can detect the significant subgrid-scale dissipation of small-scale motions and predict satisfactory turbulence statistics of the velocity gradient tensor.

Keywords: Navier-Stokes Equations, SGS Models, Vortex Stretching, Subgrid-scale Energy, Subgrid-scale Dissipation, Statistical and Machine Learning, Correlation, JPDF, Gradient Decent Algorithm.

1 Introduction

Over the last few years, the large eddy simulation (LES) technique has increased in popularity, mainly because of advancements in computational resources both in hardware and algorithm. More specifically, recent algorithmic progress in iterative methods, such as multigrid and Krylov solvers on the multiprocessor computing framework, have enabled the LES study of complex engineering flow problems. The main idea of LES is to solve the Navier-Stokes equations (NSE) using a computationally affordable three-dimensional fine grid. It is generally expected that the numerical solution of NSE would account for about 80% of the dominant degrees of freedom of turbulence. The remaining 20% of the information on turbulence is predicted based on the available data from a previous time step through a process called subgrid-scale (SGS) modeling. Smagorinsky initially introduced this idea for real-time weather prediction [1]. Over the years, LES has paved the way to solve many complex engineering problems. More recently, several investigators are advancing LES so that a subgrid model can be built upon available data history.

Another interesting idea of the fluid dynamics research community is to understand whether LES can provide appropriate relevant data that may be used to develop simplified models for studying various complex engineering problems. Turbulence is a high-dimensional dynamical system. It exhibits an average cascade of energy from large to small scales. The resolution large-eddy simulation (LES) approach utilizes subgrid models to understand turbulence energy cascade, which is saving millions of dollars for the automobile and aviation industry. Until recently, following the pioneering work of Taylor [1], there has been a scope on the dominant modern view of whether vortex stretching drives the energy from the largest to the smallest scales of motion. No one has been reached explicitly on how to engage vortex stretching in subgrid models of LES properly. In contrast, Sagaut & Cambon argue that vortex stretching opposes energy dissipation [3],[4]. They considered the Karman-Harwoth equation [5] and the interpretation that the energy flux from large to small scale would balance the viscous dissipation. Indeed, these findings lead to creating an option for more studies on how vortex stretching reduces dissipation while at the same time acting for the down-scale cascade of energy (e.g., see [4],[8]).

The objective of the present investigation is twofold. First, a parallelized LES code is developed that engages vortex stretching in a subgrid model [6]. To estimate whether vortex stretching drives the energy cascade, we consider high-resolution LES data and compare higher-order statistics of isotropic turbulence, and the velocity gradient tensor is used to investigate many universal characteristics by using joint probability density function (JPDF) regarding three subgrid-scale models. In the second part, the performance of SGS models has been studied through statistical and machine learning approaches.

This article is rearranged sequentially. In section 2, the simulation methodology has been discussed. Initial turbulent flow is discussed in section 3. Validation strategies are shown in section 4. Results of SGS models are shown in section 5. In the result section, models are compared regarding their performance. Finally, a conclusion and future scope have been drawn in section 6.

2 Simulation Methodology

In this article, instead of using explicit filtering operation, the second order finite volume discretization of the flow equation is considered the numerical mesh as an implicit filter. In this filter, the turbulent scales smaller than the grid mesh are known

*Corresponding Author Email Address: khalid@sau.ac.bd Published by: SciEn Publishing Group

as unresolved scales, while greater than grid size is called the resolved scales. It is like the operation of a box filter when the filter width is equal to the grid spacing [5],[7].

Now, the filtered equations of continuity and Navier-Stokes equation for incompressible flow can be written as:

$$\frac{\partial \overline{u_i}}{\partial x_i} = 0 \tag{1}$$

$$\frac{\partial \overline{u_i}}{\partial t} + \overline{u_j}\frac{\partial \overline{u_i}}{\partial x_j} = -\frac{1}{\rho}\frac{\partial \bar{P}}{\partial x_i} + \vartheta \frac{\partial^2 \overline{u_i}}{\partial {x_i}^2} - \frac{\partial \tau_{ij}}{\partial x_j} \tag{2}$$

Here, τ_{ij} is the subgrid-scale stresses, where $\tau_{ij} = \overline{u_i u_j} - \overline{u_i}\,\overline{u_j}$. Most of the subgrid-scale models are based on the eddy-viscosity model because of the Boussinesq hypothesis. The models can compute the deviatoric part of the SGS stress as,

$$\tau_{ij} - \frac{1}{3}\tau_{kk}\delta_{ij} = -2\vartheta_\tau S_{ij} \tag{3}$$

Eq. (3) is related to SGS stresses to the large-scale strain rate tensor S_{ij}, which is defined by $S_{ij} = \frac{1}{2}\left(\frac{\partial \overline{u_i}}{\partial x_j} + \frac{\partial \overline{u_j}}{\partial x_i}\right)$ of the resolved turbulence, δ_{ij} is the Kronecker delta, and ϑ_τ is a subgrid-scale viscosity.

The SGS models in this article are the Wall-Adapting viscosity model (SGS-A), localized dynamic kinetic energy equation model (SGS-B), and kinetic energy-based Deardorff model (SGS-C). A brief mathematical detail of three dynamic SGS models is described below.

2.1 Wall-Adapting Viscosity Model (SGS-A)

The eddy viscosity is evaluated in this subgrid-scale model by using the square of the velocity gradient tensor [6]. The turbulent kinetic energy of SGS-A model is estimated by,

$$k_{sgs} = (\Delta_{les})^2 \frac{\left(S_{ij}^d S_{ij}^d\right)^{3/2}}{\left(S_{ij}S_{ij}\right)^{5/2} + \left(S_{ij}^d S_{ij}^d\right)^{5/4}}$$

Where, Δ_{les} is the computational grid size. Now, the eddy viscosity of SGS-A model is defined as,

$$\vartheta_\tau = C_w \Delta_{les}\sqrt{k_{sgs}} \tag{4}$$

The term S_{ij}^d is a deviatoric symmetric part of the square of the velocity gradient tensor, known as $S_{ij}^d = \frac{1}{2}\left(G_{ij} + G_{ij}\right) - \frac{1}{3}\delta_{ij}G_{ii}$. Here, G_{ij} is the velocity gradient tensor. However, the term $S_{ij}^d S_{ij}^d$ is related to vortex stretching and the second invariant of the velocity gradient tensor. The term $S_{ij}^d S_{ij}^d = \frac{1}{2}|S\omega| - \frac{1}{3}Q_G^2$ can detect turbulent structures by the rotation rate, strain rate, and vortex stretching rate, which indicates that it adjusts the value of ϑ_τ dynamically on the strength of the vortex stretching rate [8]. Here, $S\omega$ and Q_G are denoted by vortex stretching and second invariant of the velocity gradient tensor. So, this SGS model is a vortex-stretching-based model, where $C_w = 0.325$ for this study.

2.2 Dynamic *k*-equation Model (SGS-B)

The localized dynamic kinetic energy model was proposed by Kim et. al., which is a kind of similar concept to the dynamic Smagorinsky model [9]. In this model, the eddy viscosity is calculated as $\vartheta_\tau = C_k k_{sgs}^{1/2}\Delta_{les}$. Here C_k is an adjustable model constant, which is calculated dynamically in this subgrid-scale model. In this SGS model, the model coefficients are computed by setting an additional test filter $\tilde{\Delta} = 2\Delta_{les}$ [10]. It is worth mentioning that the local variation of subgrid-scale energy dissipation can be accounted for in the localized dynamic kinetic energy equation via the dynamic variation of C_k, which is important in many engineering applications.

2.3 *k*-equation Model (SGS-C)

In the turbulent kinetic energy (TKE) model, the turbulent kinetic energy is obtained by solving the following transport equation [11].

$$\frac{\partial k_{sgs}}{\partial t} + \overline{u_j}\frac{\partial k_{sgs}}{\partial x_j} = -\tau_{ij}S_{ij} - C_e\frac{k_{sgs}^{\frac{3}{2}}}{\Delta_{les}} + \frac{\partial}{\partial x_j}\left(\vartheta_\tau \frac{\partial k_{sgs}}{\partial x_j}\right) \tag{5}$$

Here, k_{sgs} is the turbulent kinetic energy. The eddy viscosity ϑ_τ is estimated by using k_{sgs} value from Eq. (5) as $\vartheta_\tau = C_k k_{sgs}^{1/2}\Delta_{les}$. Here, the model constant $C_k = 0.094$ and the dissipation constant $C_e = 1.048$ are fixed. This subgrid-scale model is important for LES of atmospheric turbulence.

3 Turbulent Flow Setup

The initialization of the turbulent flow field is based on the kinematic simulation of isotropic turbulence, which is incompressible and consistent with second-order statistics. The given velocity field is generated in the Fourier space based on the following energy spectrum,

$$E(k) = E_a \frac{k^4}{k_0^4}\left(1 + \frac{k^2}{k_0^2}\right)^{\frac{-17}{6}} exp^{-2\frac{k^2}{k_n^2}} \tag{6}$$

Here, E_a is amplitude and k is the wave number. k_0 and k_n are two wave numbers that control the distribution of $E(k)$. Therefore, we have the kinetic energy $E = \frac{1}{2}\int_\Omega u^2 dx = \int_0^\infty E(k)dk$. Thus, we can choose the values of E_a, k_0 and k_n to ensure a distribution of E. The initial wave number is taken $k_0 = 5$ in Eq. (6) in such a way that the initial velocity would be $u_0 = 10$ m/s, and the Reynolds number $R_e = 5 \times 10^5$ in physical space. In the present LES simulations, the N-S equations are solved in a cubic periodic domain $[0, 2\pi]^3$, which is partitioned into $N_x \times N_y \times N_z = N$, here $N_x = N_y = N_z = 128$ nodes in each direction. The mesh size is $\Delta_{les} = \frac{2\pi}{N}$.

To analyze the relationship between the resolved strain $S_{ij} = \frac{1}{2}\left(\frac{\partial \overline{u_i}}{\partial x_j} + \frac{\partial \overline{u_j}}{\partial x_i}\right)$ and the subfilter scale stress $\tau_{ij} = \overline{u_i u_j} - \overline{u_i}\,\overline{u_j}$, this article has implemented three subgrid models, such as SGS-A, SGS-B, and SGS-C within an in-house LES code, which is written in C++ and parallelized via the message passing interface (MPI) library through OpenFOAM.

4 Validation Strategies

In this research, the vortex-stretching-based subgrid model SGS-A is validated with the other two subgrid models, say SGS-B and SGS-C. The validation processes are done by the below strategies,

The subgrid-scale production of turbulence $-\tau_{ij}S_{ij}$ must be correlated with the transfer $\tau_{ij}S_{ij}$ from grid-scale to subgrid-scale. It suggests that the transfer of energy is equal to the dissipation (loss) of energy on a subgrid scale.

Joint probability density function (JPDF) and corresponding statistics of the velocity gradient tensor.

Examine the performance of the three subgrid-scale models through a machine learning algorithm.

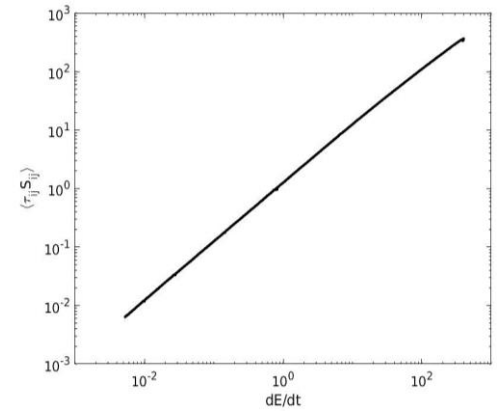

(a) SGS-A

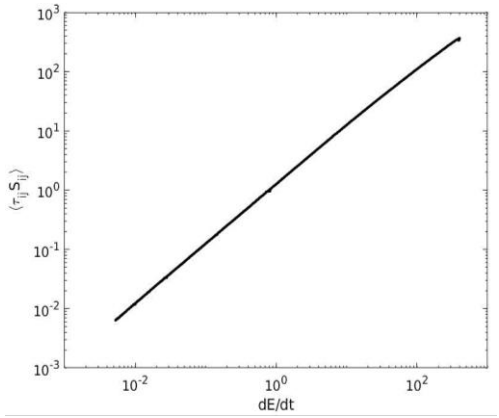

(b) SGS-B

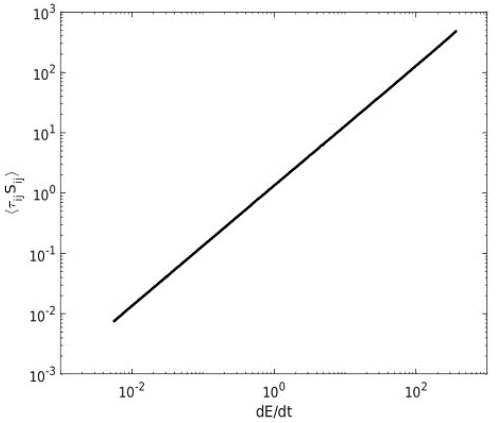

(c) SGS-C

Fig. 1 Plots of production and dissipation of turbulence among the SGS models

5 Result Analyses

5.1 Subgrid-Scale Stress, Resolved Rate of Strain, and Vortex Stretching

Time series of the rate of resolved energy $\frac{dE}{dt}$ is found to be well correlated with the energy flux $< \tau_{ij} S_{ij} >$; Fig. 1 supports the theoretical interpretation regarding the energy flux and viscous dissipation [8]. Indeed, the energy is transferred by large eddies to the subgrid-scale, which is dissipated at a rate of subgrid-scale dissipation, $\varepsilon_{sgs} = 2\vartheta_\tau ||S||$. It is worth mentioning that the most important requirement of turbulence modeling on the statistics of subfilter scale stress τ_{ij} is to reproduce the evolution of turbulence kinetic energy [12]. Thus, the consideration of vortex stretching should correctly reproduce the correlation of a subgrid model τ_{ij}^{sgs} with the strain-rate tensor, i.e., $< \tau_{ij}^{sgs} S_{ij} > = < \tau_{ij} S_{ij} >$. A primary observation is that the consideration of the square of the velocity gradient tensor is an effective way of enforcing scale-adaptivity in ϑ_τ via vortex stretching mechanism. If a vortex tube is stretched, the eddy viscosity grows locally, thereby transferring the energy to the subgrid scale.

5.2 Joint Probability Density Function (JPDF) of SGS Models

In this section, invariants of velocity gradient tensor of isotropic turbulence in LES are analyzed statistically by the proposed three subgrid-scale models. An advanced data-analytics approach is considered to observe some hidden flow topology in subgrid models. Using this approach, five invariants are analyzed to describe the mechanism and dynamics of turbulent flow. Because the invariants are significantly important in the context of visualization of the various flow patterns or coherent structures [13] and detecting the vortical structure of turbulent flow [14]. The datasets of invariants are generated at s fixed dimensionless eddy turn over time, $\frac{t}{T} = 1$. Using the datasets, JPDF of such invariants have been visualized to illustrate the features of small-scale statistics and relevant mechanisms of large energy-containing scales.

The invariants can define the arbitrary points of flow topology by deploying the eigenvalues of the velocity gradient tensor G [15],[16]. Hence, the characteristics equation of the velocity gradient tensor is,

$$\lambda_i^3 + P_G \lambda_i^2 + Q_G \lambda_i + R_G = 0 \tag{7}$$

Here, λ_i is eigenvalues. P_G, Q_G, and R_G are the first, second, and third invariants of G, respectively. However, for incompressible flow, $P_G = 0$.

The JPDF describes the jointly random variables on a probability space. In this article, The JPDF is studied through: (i) between the second invariant (Q_G) and third invariant (R_G), (ii) between the strain rate of the second invariant (Q_S) and the strain rate of the third invariant (R_S), and (iii) between second invariant rate (-Q_S) and rotation rate (R_S).

Now, Mathematical formulas of such invariants are shown here. Using the strain rate (S_{ij}) and rotation rate (R_{ij}), the second and third invariants of G are obtained by,

$$Q_G = \frac{-1}{2}\left(S_{ij}S_{ij} - R_{ij}R_{ij}\right) \tag{8}$$

$$R_G = \frac{-1}{3}\left(S_{ij}S_{jk}S_{ki} + \frac{3}{4}\omega_i\omega_j S_{ij}\right) \tag{9}$$

The strain rate of the tensor of second and third invariants are obtained by,

$$Q_S = \frac{-1}{2}\left(S_{ij}S_{ij}\right) \tag{10}$$

$$R_G = \frac{-1}{3}\left(S_{ij}S_{jk}S_{ki}\right) \tag{11}$$

Finally, the second invariant rotation rate is getting by,

$$Q_R = \frac{1}{2}\left(R_{ij}R_{ij}\right) \tag{12}$$

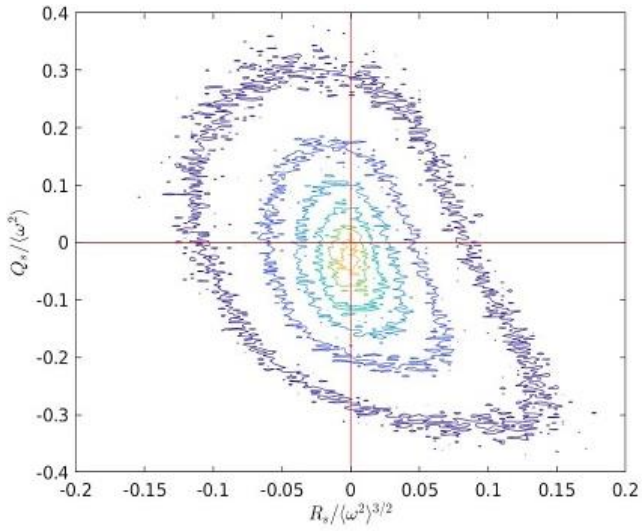

(a) SGS-A

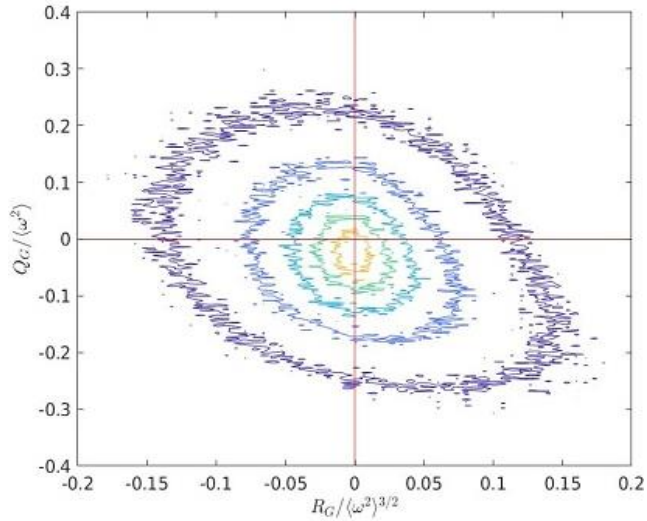

(b) SGS-B

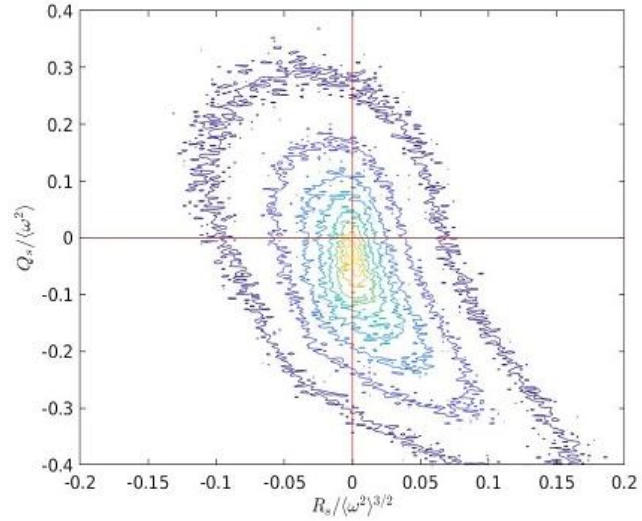

(c) SGS-C

Fig. 2 The JPDF between the second invariant (Q_G) and third invariant (R_G)

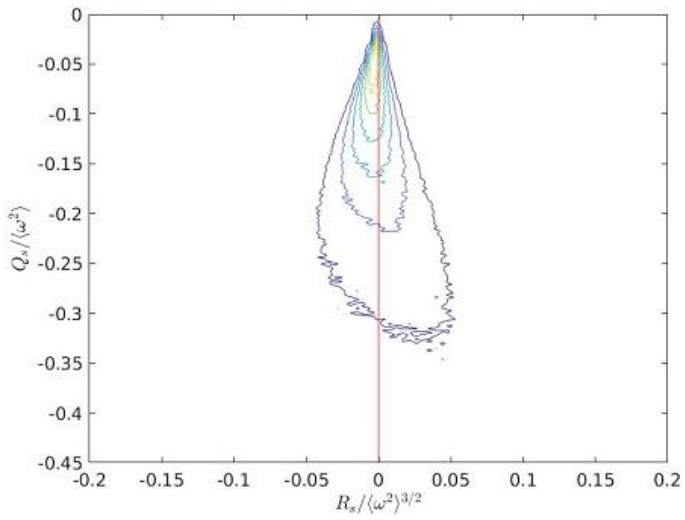

(a) SGS-A

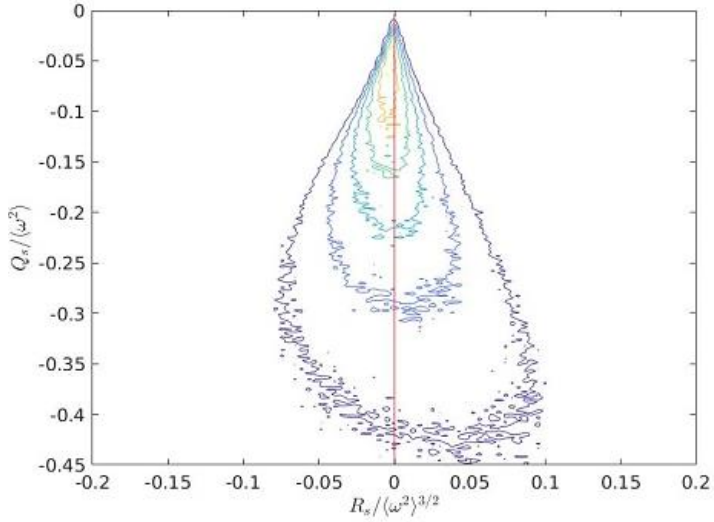

(b) SGS-B

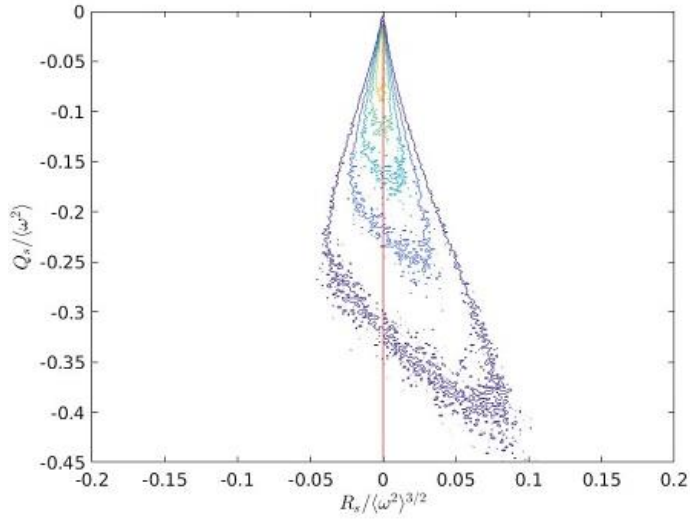

(c) SGS-C

Fig. 3 The JPDF between the second invariant of strain rate (Q_S) and third invariant of strain rate (R_S)

The JPDF map between the second invariant (Q_G) and third invariant (R_G), and topological classification of local flow fields are shown in Fig. 2, see more detailed information [8],[15],[16]. The region of Fig. 2 describe as, (i) the region $R_G < 0$ and $Q_G > 0$ is associated with vortex stretching, (ii) the region $R_G > 0$ and $Q_G > 0$ is associated with vortex compression, (iii) the region $R_G < 0$ and $Q_G < 0$ is associated with tube structures, and (iv) the region $R_G > 0$ and $Q_G > 0$ is associated with sheetlike structures. In Fig. 2, two important characteristic features have been observed in the SGS models.

First, a trend of teardrop shape appears in SGS models. In this region, the fluid flow is controlled by the sheetlike structures, which indicates that the total strain rate $S_{ij}S_{ij}$ is increased over weak vortex stretching. It also indicates a universal feature of turbulence [7],[8]. Secondly, the bulk of data is presented in the upper left quadrant showing intense vortex stretching, $\omega_i\omega_j S_{ij} > 0$ in the subgrid-scale models. Hence, the Q_G and R_G map of SGS models indicates that the $\omega_i\omega_j S_{ij}$ and $S_{ij}S_{ij}$ are playing a role for the energy cascade.

The JPDF map between the second invariant of strain rate (Q_S) and third invariant of strain rate (R_S), and topological classification of local flow fields are shown in Fig. 3, see more detailed information [8],[18]. In order to analyze the geometry of the straining motion of the fluid elements, the JPDF of the second invariant of strain rate (Q_S) and third invariant of strain rate (R_S) of the velocity gradient tensor is studied, see Eqs. (10) and (11). All the three SGS models have shown similar behaviour in which the flow topology for isotropic turbulent flow field is predominated by sheetlike structures. Finally, the region $R_S > 0$ and $Q_S < 0$ indicates the intense kinetic energy dissipation in subgrid models, see Fig. 3.

The JPDF map between the second invariant of strain rate ($-Q_S$) and second invariant of rotation rate (Q_w) is shown in Fig. 4. It is an important investigation to demonstrate the dissipation of kinetic energy through rotation rate and straining rate of G. In Fig. 4, the vertical axis $-Q_S$ is associated to the dissipation of kinetic energy [17],[18]. Thus, the points near the axis $-Q_S$ is dominated by the straining motion over weak enstropy. However, the horizontal axis $Q_w$is linked to high enstrophy over few dissipations. The most interesting physical information is presented by the diagonal axis, $-Q_S = Q_w$, where it demonstrates the points of flow field associated with the high enstropy and high dissipation [8]. As we can see in Fig. 4, a strong correlation between dissipation and enstropy along the diagonal line is presented in SGS models.

5.3 Performance between Subgrid-Scale Models

The correlation is a statistical summary of the relationship between the variables, see for information [19]. This section will focus how on studying the correlation between subgrid-scale model variables. The velocity component U_x of a cell value at $\frac{t}{T} = 1$ eddy turn-over time of the SGS models is considered for this purpose. Approximately 700 samples of U_x are studied in this article see Fig. 5. Specifically, this study will examine how much the velocity component U_x of SGS-A model is associated with U_x of SGS-B and SGS-C models. If we compare the U_x of SGS-A model with the SGS-B and SGS-C models, we get almost similar performance among the subgrid models, see Fig. 6.

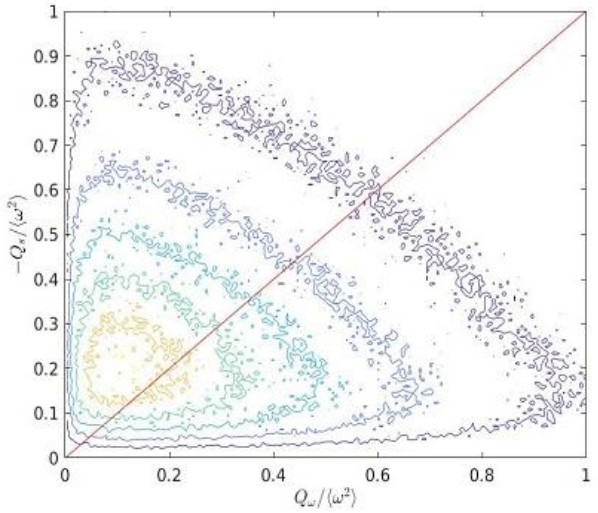

(a) SGS-A

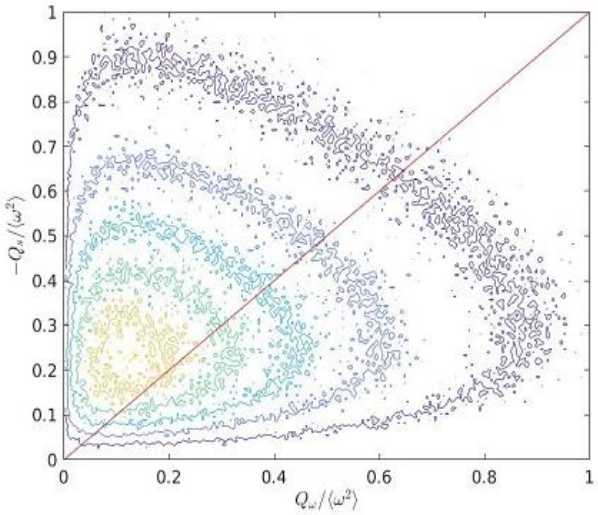

(b) SGS-B

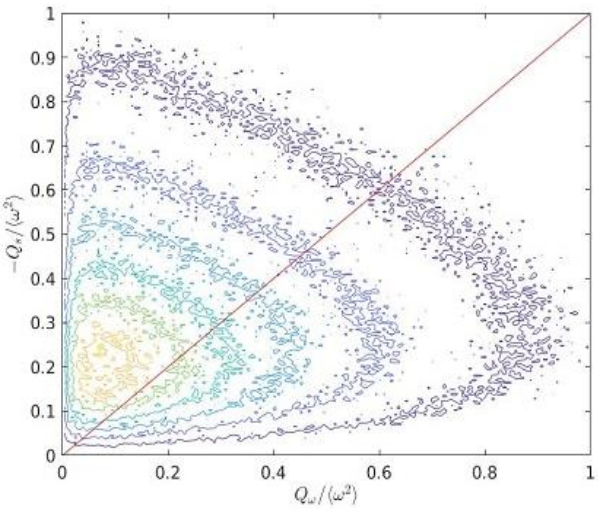

(c) SGS-C

Fig. 4 The JPDF between the second invariant of strain rate ($-Q_S$) and second invariant of rotation rate (Q_w)

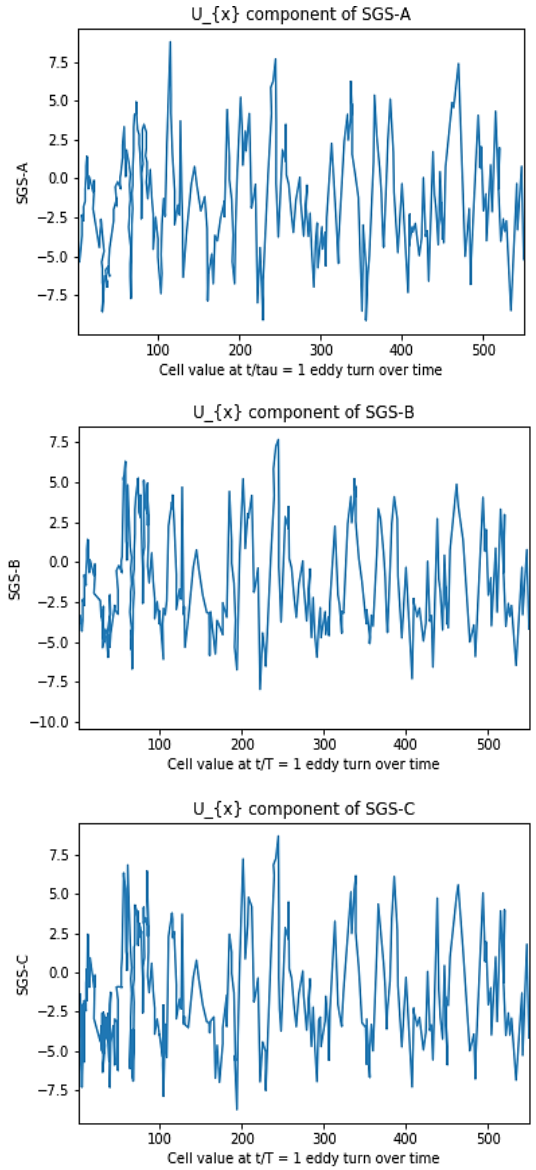

Fig. 5 Cell value of U_x at $\frac{t}{T} = 1$ eddy turn-over time of the SGS models.

Before examining the correlation between the SGS models, this article shows some general statistics and covariance of U_x datasets of the SGS models. Since the covariance (COV) between SGS-A and SGS-B is 10.70 and between SGS-A and SGS-C is 11.03. These are the positive covariance; see Table 1. It indicates that the variables change in the same direction as we expect.

Table 1 Comparing the statistical performance of SGS models for the U_x component.

Models	Mean	25%	50%	75%	STD	COV
SGS-A	-1.36	-3.82	-1.40	0.82	3.46	-
SGS-B	-1.18	-3.63	-1.82	0.86	3.27	-
SGS-C	-1.25	-3.69	-1.78	0.96	3.55	-
SGS-A v/s SGS-B	-	-	-	-	-	10.70
SGS-A v/s SGS-C	-	-	-	-	-	11.03

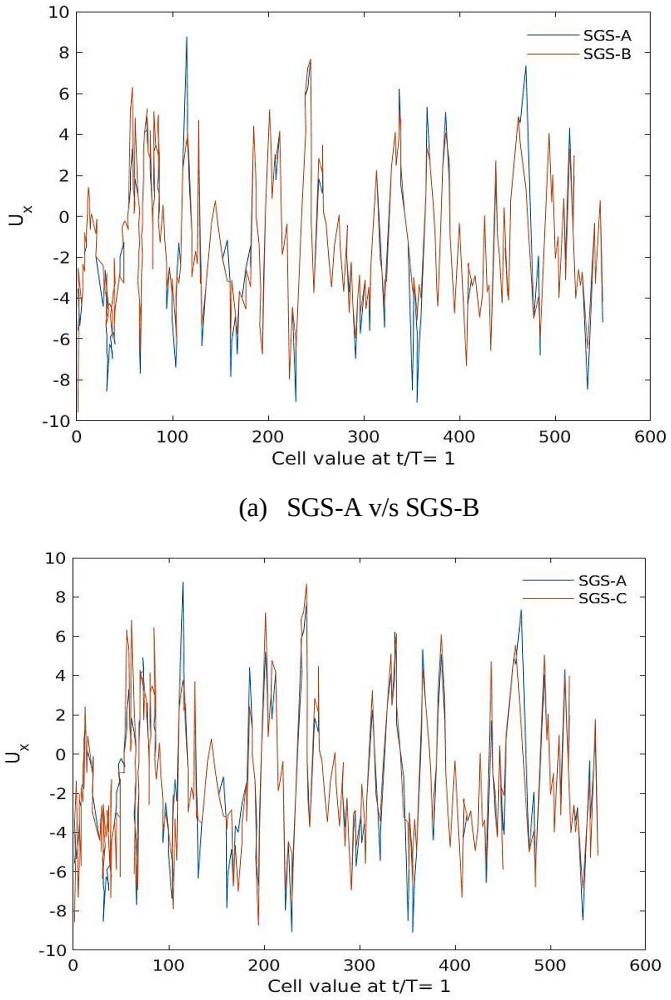

(a) SGS-A v/s SGS-B

(b) SGS-A v/s SGS-C

Fig. 6 Comparing the shape of SGS-A with SGS-B and SGS-C subgrid models.

Now, Pearson's correlation (PC) and Spearson's correlation (SC) have been studied between the subgrid models. The PC and SC are useful to study to summarize the strength of a linear relationship between the datasets. Table 2 and Table 3, clearly state that the velocity component U_x of the SGS models have positive correlations. The Pearson's correlation of SGS-A between SGS-B and SGS-C are 0.9 and 0.8, whereas Spearson's correlation of SGS-A between SGS-B and SGS-C are 0.9 and 0.9, respectively.

Table 2 Comparing the Pearson's correlation of the SGS models

SGS Models	Variable	Pearson's correlation
SGS-A v/s SGS-B	U_x	0.9
SGS-A v/s SGS-C	U_x	0.8

Table 3 Comparing Spearson's correlation of the SGS models

SGS Models	Variable	Spearson's correlation
SGS-A v/s SGS-B	U_x	0.9
SGS-A v/s SGS-C	U_x	0.9

The correlation matrices are plotted regarding three SGS models data in Fig. 7, see more details in [1],[19]. It is showing an excellent performance with Pearson's correlation and Spearson's correlation values. Moreover, all three SGS models are presented like Gaussian distribution in Fig. 7.

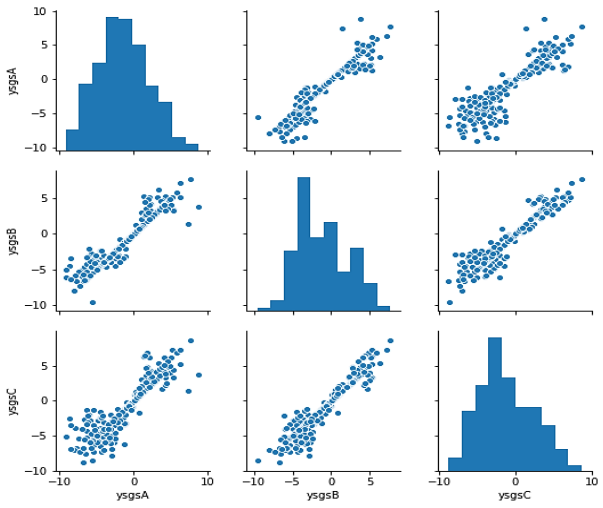

(a)

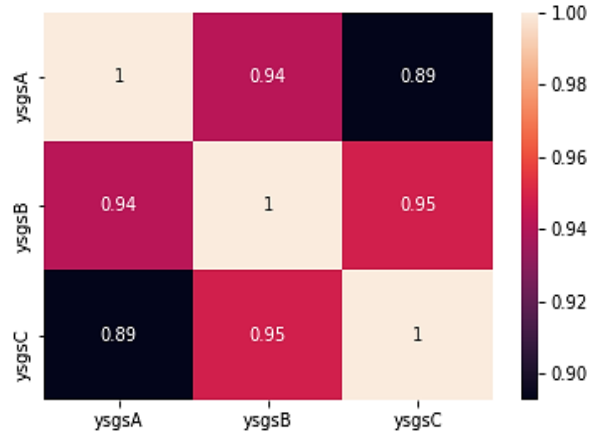

(b)

Fig. 7 (a) Pair plots, and (b) correlation matrix of $U_x$component between the SGS models

Finally, Gradient decent algorithm has been studied to identify the performance of SGS models. So, in order to train the machine learning and deep learning models, gradient decent is one of the most popular iterative optimization algorithms [20]. It is useful in finding the local minimum of a function. The main advantage of using a gradient decent algorithm is to minimize the cost function using iteration. However, the cost function is described as the measurement of the difference or inaccuracy between the current position's actual values and expected values, and it takes the form of a single real integer. In Fig. 8, gradient decent has been shown for the U_x component of SGS-A and SGS-B models.

Similarly, gradient decent has been shown for the $U_x$component of SGS-A and SGS-C models in Fig. 8. Corresponding linear regression plots of $U_x$component for SGS models present well performance by obtaining the minimum bias, see Fig. 8. Both figures are showing similar weights of 0.9, and a minimum cost between SGS-A and SGS-B is 1.22, whereas the minimum cost between SGS-A and SGS-C is 2.5.

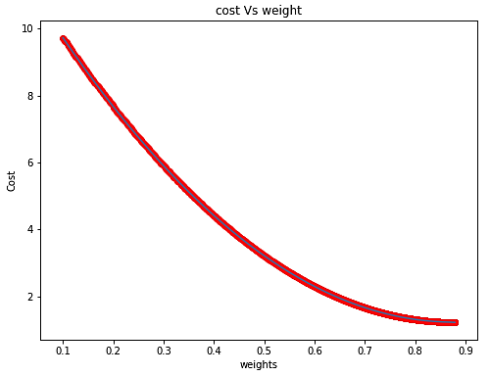

(a) Plot of cost v/s weight of U_x data between SGS-A and SGS B models.

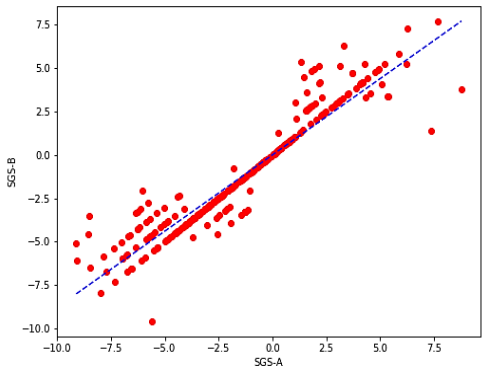

(b) Liner regression plot of U_x between SGS-A and SGS-B models.

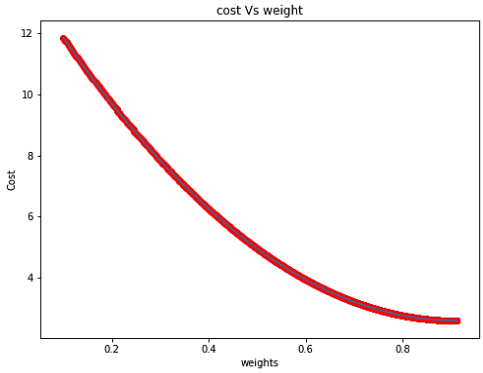

(c) Plot of cost v/s weight of U_x data between SGS-A and SGS-C models.

Fig. 8 Plot of cost v/s weight of U_x data between SGS models

6 Conclusion and Future Scope

The present article is focused on the subgrid-scale dissipation and production of turbulence generation, which is significantly influenced by the potential role of vortex stretching. The concept of this article learns through the statistical and machine learning approaches. For this purpose, the vortex stretching-based model SGS-A is used to demonstrate the SGS dissipation and validated with other two dynamic SGS models, such as SGS-B and SGS-C. The performance of the SGS-A model is well agreed with SGS-B and SGS-C models. Specifically, the loss of turbulence is more correlated to the turbulence production in the SGS-A model compared with the other SGS models. The JPDF of SGS model is presented the vortex stretching and sheetlike dissipation in the models and

indicates a playing role in a turbulent flow. Hence, this study suggests that the vortex stretching mechanism cascades energy.

These findings suggest that a turbulence model can effectively learn about the SGS dissipation from singular values of the velocity gradient tensor. The findings of JPDF of invariants of the velocity gradient tensor suggest that we may further learn about JPDF for higher resolution of LES data. Other possible further applications can include, such as magneto hydrodynamics, Ocean atmosphere, aerodynamics, fluid-solid interactions, etc.

References

[1] Smagorinsky, J., 1963. General circulation experiments with the primitive equations: I. The basic experiment. *Monthly Weather Review*, *91*(3), pp.99-164.

[2] Taylor, G.I., 1938. Production and dissipation of vorticity in a turbulent fluid. *Proceedings of the Royal Society of London. Series A-Mathematical and Physical Sciences*, *164*(916), pp.15-23.

[3] Carbone, M. and Bragg, A.D., 2020. Is vortex stretching the main cause of the turbulent energy cascade?. *Journal of Fluid Mechanics*, *883*.

[4] Sagaut, P. and Cambon, C., 2008. *Homogeneous turbulence dynamics* (Vol. 10). Cambridge: Cambridge University Press.

[5] Pope, S.B. and Pope, S.B., 2000. *Turbulent flows*. Cambridge university press.

[6] Nicoud, F. and Ducros, F., 1999. Subgrid-scale stress modelling based on the square of the velocity gradient tensor. *Flow, turbulence and Combustion*, *62*(3), pp.183-200..

[7] Davidson, P. (2004). Turbulence: an introduction for scientists and engineers. Oxford University Press.

[8] Hossen, M.K., Mulayath Variyath, A. and Alam, J.M., 2021. Statistical Analysis of Dynamic Subgrid Modeling Approaches in Large Eddy Simulation. *Aerospace*, *8*(12), p.375.

[9] Kim, W.W. and Menon, S., 1995. A new dynamic one-equation subgrid-scale model for large eddy simulations. In *33rd Aerospace Sciences Meeting and Exhibit* (p. 356).

[10] Meneveau, C., 2010. Turbulence: Subgrid-scale modeling. *Scholarpedia*, *5*(1), p.9489.

[11] Deardorff, J.W., 1972. Numerical investigation of neutral and unseq planetary boundary layers. *Journal of Atmospheric Sciences*, *29*(1), pp.91-115.

[12] Hossen, M. K., Variyath, A., & Alam, J., 2021. Statistical analysis of the role of vortex stretching in large eddy simulation. *Proceedings of the 29th Annual Conference of the Computational Fluid Dynamics Society of Canada. CFDSC2021*. July 27-29, Online.

[13] Martın, J., Ooi, A., Chong, M.S. and Soria, J., 1998. Dynamics of the velocity gradient tensor invariants in isotropic turbulence. *Physics of Fluids*, *10*(9), pp.2336-2346.

[14] Jeong, J. and Hussain, F., 1995. On the identification of a vortex. *Journal of Fluid Mechanics*, *285*, pp.69-94.

[15] Perry, A.E. and Chong, M.S., 1994. Topology of flow patterns in vortex motions and turbulence. *Applied Scientific Research*, *53*(3), pp.357-374.

[16] Martın, J., Ooi, A., Chong, M.S. and Soria, J., 1998. Dynamics of the velocity gradient tensor invariants in isotropic turbulence. *Physics of Fluids*, *10*(9), pp.2336-2346.

[17] Dallas, V. and Alexakis, A., 2013. Structures and dynamics of small scales in decaying magnetohydrodynamic turbulence. *Physics of Fluids*, *25*(10), p.105106.

[18] da Silva, C.B. and Pereira, J.C., 2008. Invariants of the velocity-gradient, rate-of-strain, and rate-of-rotation tensors across the turbulent/nonturbulent interface in jets. *Physics of Fluids*, *20*(5), p.055101.

[19] Hossen, M.K., 2022. Heart Disease Prediction Using Machine Learning Techniques. *American Journal of Computer Science and Technology*, *5*(3), pp.146-154.

[20] Wikipedia contributors. (2022, June 28). Gradient descent. In Wikipedia, The Free Encyclopedia. Retrieved 05:31, July 23, 2022, from https://en.wikipedia.org/w/index.php?title=Gradient_descent&oldid=1095507248.

SciEn
Journal of Engineering Advancements Vol. 03(03) 2022, pp 104-111 https://doi.org/10.38032/jea.2022.03.005

An Efficient Computational Technique for the Analysis of Telegraph Equation

Selim Hussen[1], Mahtab Uddin[2,] and Md. Rezaul Karim[3]*

[1]Department of Mathematics, Chittagong University of Engineering and Technology, Chattogram-4349, Bangladesh
[2]Institute of Natural Sciences, United International University, Dhaka-1212, Bangladesh
[3]Department of Mathematics, Jagannath University, Dhaka-1100, Bangladesh

Received: June 28, 2022, Revised: September 16, 2022, Accepted: September 18, 2022, Available Online: September 27, 2022

ABSTRACT

The Telegraph equation has drawn much attention due to its recent variety of applications in different areas of the communication system. Various methods have been developed to solve the Telegraph equation so far. In this research paper, we have formulated a derivation mathematically for the Telegraph equation for the section of a line of transmission concerning the voltage associated and the current. Therefore, obtained mathematical equation has been solved numerically by COMSOL Multiphysics. We have then numerically analyzed the parametric behavior of the Telegraph equation. The analysis first starts with allowing both the damping coefficients to vary, keeping the transmission velocity fixed, and observing the pulse shape at different time slots. We have then investigated the deformation of the pulse caused due to the gradual increase of transmission velocity for varying damping coefficients at the intended discrete time slots. Finally, we analyzed the behavior of the associated voltage pattern for those variations due to the corresponding distance of the Telegraph wire. We have observed that changes in the damping coefficients have a gradual impact on the associated voltage of the Telegraph equation, which is more conspicuous for the higher time slots. Transmission velocity is found as the most influential parameter of the Telegraph equation that controls the deformation of the pulse height, which is the cardinal part of the inquiry.

Keywords: Damping Coefficients, Transmission Velocity, Time Propagation, Voltage Drop, Pulse Height, COMSOL Multiphysics, Numerical Simulation.

1 Introduction

In this modern age, we need a high-frequency communication system and this system needs transmission media for transferring a signal from one point to another. We can categorize the transmission media into two groups, viz. guided and unguided media. Signals through the guided medium are transferred through the transmission line or the coaxial cable. But in the case of unguided media, the signals partly or entirely through the path of communication are carried by electromagnetic waves and are carried through the radio frequencies (RF) and microwaves (MW) communication channels. Transmission and reception of electromagnetic waves are done through the antenna. For addressing the problem of efficiency of telegraphic transmission in the case of guided medium, we investigate the cable transmission medium specifically. Since all the systems incur losses, optimizing the system of communication with guided, therefore the determination or power of the project along with the losses of signals is essential. For the determination of loss and finally for ensuring the output with maximum value, we need the determination of the losses, and these losses are to be calculated with some equations which are to be formulated essentially.

1.1 Historical Background of Telegrapher's Equations

The Telegraph equations are comprised of differential equations in linear pairs. These equations express the voltage and current through a line of transmission with electricity based on the distance covered and the time spent. These equations had been followed since Oliver Heaviside developed the model of the line of transmission in the 1880s, and that is what is described in this paper [1]. The objective model is to demonstrate the waves related to electromagnetic that can have reflection through the wire. Also, these patterns of waves may have their appearance along these lines [2]. This concept may apply to the lines of transmission regardless of frequency that is for lines of transmission with frequency in high (for example, wires of the telegraph, conductors corresponding to frequency of radio), frequency of audio (e.g., lines of telephone), and frequency is low (e.g., lines of power). And it is also applicable for direct current (DC) [3].

S. A. Yousefi applied a numerical method based upon Legendre multiwavelet approximations for solving the one-dimensional hyperbolic telegraph equation. He utilized the properties of the Legendre multiwavelet along with the Galerkin method to reduce the telegraph equation to the solution of algebraic equations [4]. M. Lakestani and B. N. Saray solved the Telegraph equation using interpolating scaling functions and reduced the equations to a set of algebraic equations using the operational matrix of derivatives [5]. M. Dehghan and A. Ghesmati developed a new method based on the unification of fictitious time integration (FTI) and group preserving (GP) methods and applied it to solve the Telegraph equation [6]. V. K. Srivastava *et al.* deduced the exact solution or a close to the exact solution of the differential equations by the reduced differential transform method and applied it to the Telegraph equation too (RDTM) [7]. R.C. Mittal and R. Bhatia numerically solved the one-dimensional hyperbolic telegraph equation by the B-spline collocation method. The method is based on the collocation of modified cubic B-spline basis functions over finite elements [8]. R. C. Tautz and I. Lerche introduced a closed-form analytical technique for solving the three-dimensional Telegraph equation

*Corresponding Author Email Address: mahtab@ins.uiu.ac.bd Published by: SciEn Publishing Group

and implemented it for cosmic-ray transport [9]. G. Arora and V. Joshi obtained the approximate solution of the telegraph equation with two different modified spline basis functions by the differential quadrature method and computed the weighting coefficients to transform the equation into a set of first-order conventional differential equations that were again solved by the SSP-RK43 method and compared the convenience of the methods applied [10]. S. N. Hussen numerically solved the one-dimensional hyperbolic telegraph equation by using the q-homotopy analysis method (q-HAM) and obtained greater convergence compared to the homotopy analysis method (HAM) [11]. Z. Stojanović and E. Čajić observed the phenomena occurring in one part of the electromagnetic spectrum in the frequency range of 1 GHz-100 GHz as an aggravating factor in signal transmission by telecommunication water [12]. H. Khan et al. implemented a decomposition method-based analytic approach utilizing the natural transformation. Caputo operator is incorporated for the fractional derivative and applied for the analytical treatment of the solution of fractional-order hyperbolic Telegraph equation. Some practical examples are assigned for the justification of their work [13]. M. S. Hashemi applied the technique of Shape functions extracted from the moving Kriging (MK) interpolation to the weak form of the telegraph equation (TE) in space coordinates and got a system of second-order ordinary differential equations concerning the time variable. The resultant system was solved by the group preserving scheme (GPS) [14]. Y. Zhou et al. derived a hybrid meshless method for solving the second-order telegraph equation in two-space dimensions incorporating the Dirichlet or mixed boundary conditions. They successfully applied and validated their work for a meshless finite difference method for solving and analyzing the second-order Telegraph equation [15].

In this work, we have analyzed the behavior of the voltage pattern of the Telegraph wire due to the variations of the corresponding parameters, namely, damping coefficients and transmission velocity for several discrete time slots. The solution of the Telegraph equation is not aimed but rather the impact of the parametric variations. The investigation is incorporated numerical simulation, graphical representation, and narrative analysis. A case-by-case discussion is conferred at the end of the work.

1.2 Distributed Components

The Telegraph equation, like other equations that describe phenomena in electrical, is resulted from Maxwell's equations [16]. In the practical application of engineering fields, it is assumed about the conductors that they comprise components with two-port and a series of infinite elementarily and each component represents a segment that is short and very infinitesimal to the line of transmission [17]. For the convenience of the description of the components and attributes of the Telegraph equation, Table 1 is indispensable, which includes the interpretations of various symbols and notations that are associated with this work.

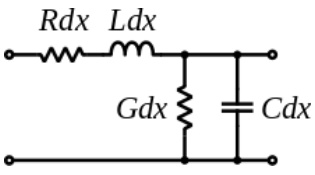

Fig. 1 Schematic depiction of the distributed components of a line of transmission [18].

Fig. 2 Schematic depiction of the wave flowing through a transmission line [18].

In Fig. 1, the distributed resistance R for conductors has been represented with series of resistor which expresses length per unit in terms of ohms. The inductance of distribution L for the field of magnetic around the wire, self-inductance, etc.) has been represented with series of inductor (Henries of length for per unit). The capacitance C has been illustrated with a capacitor (farads of length per unit) of the shunt that is between conductors and two in numbers. The conductance G of dielectric materials that separate conductors has been represented with a resistor of a shunt between a wire of signal and a wire of return (siemens of length per unit). Resistor associated with the resistance $\frac{1}{G}$ ohms [19]-[21].

Table 1 Nomenclature of the symbols and notations.

Symbol/Notation	Name of the component/parameter
R	Distributed resistance for the conductors
L	The inductance of the distribution
C	The capacitance of the dielectric materials
G	Conductance of the dielectric materials
v	Associated voltage in the cable
i	Associated current in the cable
x	Distance corresponding to the end from where the cable sends
t	Time for current flow
p q	Partial differential equation coefficients or the damping coefficients
r	Transmission velocity
dx	Increment in distance
v_x	The first-order partial derivative of v concerning x
v_t	The first-order partial derivative of v concerning t
v_{xx}	The second-order partial derivative of v concerning x
v_{tt}	The second-order partial derivative of v concerning t

Fig. 2 depicts the wave flowing from the rightward direction to downward through a lossless line of transmission where the black dot represents electrons. The field of electricity is shown by drawing arrows. The components with their role based on the animation can be visualized on the right side.

The model that we have proposed is consisting of components of elements that are infinitesimal and with a series of infinite series of the infinite are depicted in Fig. 1. Also, we have specified their values by the length of the unit. Also, we treat the mentioned quantities as primary line constants so that they can be distinguished from secondary line constants, all of them are impedance of characteristic, constant of propagation, constant of attenuation, and constant of phase. They are the constants concerning current, voltage, and time. These can be treated as the frequency of functions that are not constants.

1.3 Role of Different Components

The inductance L happens interestingly that the electrons seem to have inertia, which means that the flow of current cannot be increased or decreased easily with a large inductance for any points given. Inductance with a large amount causes waves to move even much slowly, same as that wave can travel much slowly downward a rope with a heavy size than that of one with light size which can give it larger impedance (relatively current with a lower amount for identical voltage). Capacitance C has control over the bunched-up electrons of bunched-up on the point that how much they repel each other, and also on the point of attraction of the spread-out electrons that how much they attract each other conversely. Attraction and repulsion for the capacitance of large value become less due to another line that usually contains the charge of opposite character and balances partly the force of attraction or repulsion. Alternatively, it can be said that the identical charge build-up causes less amount of voltage for the larger capacitance (i.e., the force of weak restoring), which causes waves to move slowly and give the impedance of a lower amount (i.e., the voltage of lower amount for the current of the same value). R is corresponding to the resistances within lines whereas G allows the current to flow to and from one line to another. Fig. 1 shows the lossless line of transmission, whereas both R and G taken to be zero.

2 Numerical Investigations of the Attributes of Telegraph Equation

In this section, numerical analysis of the behavior of the Telegraph equation is observed. Model setup along with the initialization of the parameters and the boundary conditions with the initial condition for the desired Telegraph equation is discussed.

2.1 Model Setup

We have assumed a wire piece with cable of the Telegraph has infinitesimal and also assumed it to be a circuit of electricity which is demonstrated in Fig. 3. Furthermore, we assumed this cable to be insulated imperfectly for which the existence of capacitance along with the leakage of current to the ground is observed [22].

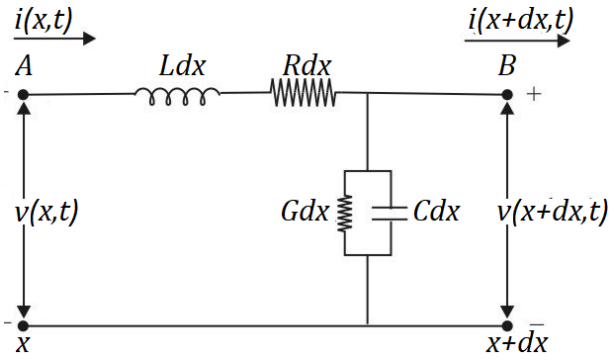

Fig. 3 Schematic depiction of telegraphic transmission line involving leakage [23],[24].

In Fig. 3 assume that x be the distance corresponding to the end from where the cable sends; $v(x,t)$ be the associated voltage with time t for points; $i(x,t)$ be the associated current on the cable with time for points, also R be the cable's resistance; C be the capacitance that is associated to the ground; L be the cable's inductance, and G be the conductance that is associated to ground.

Therefore, the voltage using the laws of Ohm across the resistor can be written as

$$v = iR. \tag{1}$$

Now, the drop of voltage across the inductor is the following

$$v = L\frac{di}{dt}. \tag{2}$$

Across the capacitor, the drop of voltage is given by

$$v = \frac{1}{C}\int idt. \tag{3}$$

Now, the voltage at the terminal B equals the voltage of the terminal at A, subtraction the voltage drop along considered element AB, therefore combining Eqs. (1), (2), and (3) together, it can be written as

$$v(x+dx,t) - v(x,t) = -[Rdx]i - [Ldx]\frac{\partial i}{\partial t}. \tag{4}$$

Let $dx \to 0$ then partial differentiation of Eq. (4) concerning x yields

$$\frac{\partial v}{\partial x} = -Ri - L\frac{\partial i}{\partial t}. \tag{5}$$

Likewise, the current at the terminal B equals to current at the terminal A subtraction current throughout the leakage to the ground, then it is found that

$$i(x+dx,t) = i(x,t) - [Gdx]u - i_c dx. \tag{6}$$

Now, the current throughout the capacitor can be written as

$$i_C = C\frac{\partial u}{\partial t}. \tag{7}$$

Now, differentiating Eqs. (4) and (7) concerning x and t, respectively. We eliminate the derivatives of v. Finally, we get the followings

$$r^2\frac{\partial^2 i}{\partial x^2} = \frac{\partial^2 i}{\partial t^2} + (p+q)\frac{\partial i}{\partial t} + (pq)i, \tag{8}$$

$$r^2\frac{\partial^2 v}{\partial x^2} = \frac{\partial^2 v}{\partial t^2} + (p+q)\frac{\partial v}{\partial t} + (pq)v, \tag{9}$$

where $p = \frac{G}{C}$ and $q = \frac{R}{L}$ are positive constants and are known as damping coefficients, $r = \frac{1}{\sqrt{LC}}$.

Equations (8) and (9) comprise the aimed one-dimensional hyperbolic second-order Telegraph equation [25].

2.2 Parameter Setup

We can use this model of the Telegraph equation to investigate how pulses of voltage are transmitted through the Telegraph wires. This model of the Telegraph equation can model mixtures between the diffusion and the propagation of a wave that can introduce the term which causes the standard heat or equation of transport of mass for effects of finite velocity [26]. This example is modeled for a Telegraph wire of a small section and it involves the study of the pulse's voltage while it moves along it. The results that cause the varying damping coefficients are sketched with the shape of the pulse and are provided by a parametric sweep.

It is very simple to define the model where the geometry consists of a line of length 1 which is one-dimensional. The

initial condition is taken as a voltage distribution that is bell-shaped and thus the pulse is modeled. The conditions corresponding to the boundary define flux at both ends for the section of the wire and these conditions allow freely varying the voltage.

The Telegraph equation (Eq. (9)) can be written in a more compact form as

$$v_{tt} + (p+q)v_t + pqv = r^2 v_{xx}. \tag{10}$$

Here, v, the dependent variable denotes the voltage, whereas x, the independent variable denotes the distance from the initial position of the Telegraph wire. The model has been initiated for some fixed parameters that are for $p = 0.5 = q$ and $r = 1$.

2.3 Boundary Conditions and Initial Condition

At both ends, the boundary conditions are Neumann conditions and are also homogeneous as

$$v_x(t,0) = 0, \quad v_x(t,1) = 0. \tag{11}$$

The initial condition consists of the following equations which are describing a bell-shaped pulse and has the highest point at 0.2 and also a base width of 0.4.

$$v(0,x) = e^{-3\left(\frac{x}{0.2}-1\right)^2}, \; v_t(0,x) = 0. \tag{12}$$

3 Results and Discussion

This section investigates the important mathematical properties of the Telegraph equation. The following is aimed to provide insight into the behavior of the Telegraph equation. In particular, we analyze the characteristic structure of the Telegraph equation. We will interpret graphically in one-dimensional space. Here, we applied COMSOL Multiphysics (version 4.3) for the numerical computation in a Windows machine having an Intel i5-6200U CPU with 2.30 GHz clock speed, 2 cores each, and 8 GB of total RAM.

We have studied the effect of the variations of the partial differential equation coefficients (damping coefficients) p and q, and the transmission velocity r on the pulse's shape (length vs voltage graph) for several discrete time slots. In Eq. (10), it is observed that the co-efficient of voltage and its rate of change about the time both are symmetric. They exhibit the variations attributes for the changes of the $p+q$ and pq, not the individual changes of p and/or q. But there are significant variations found for the changes in transmission velocity r over time specified time slots.

In this section, we are investigating the effect of the changes in the transmission velocity r for some discrete time slots with some particularized values of damping coefficients p and q. We are exploring the deformation of the pulse shape of the Telegraph equation due to the desired variations.

In the following case studies, we are scrutinizing the variation of voltage (v) for the damping coefficients p and q, ranging $p+q = 1, 2, 3, 4$ for the transmission velocity $r = 1, 2, 3$ and discrete time slots ranging $t = 0.25, 0.5, 0.75, 1$. These observations are attained from numerical simulations and analyzed graphically.

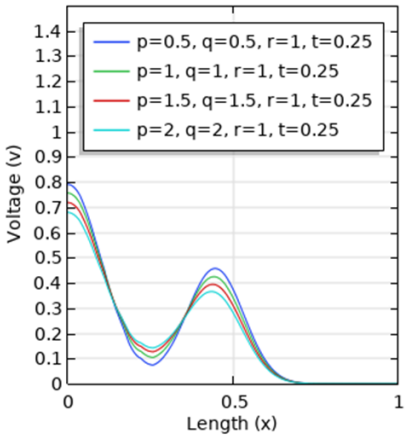

(a) Transmission velocity $r = 1$ and time $t = 0.25$

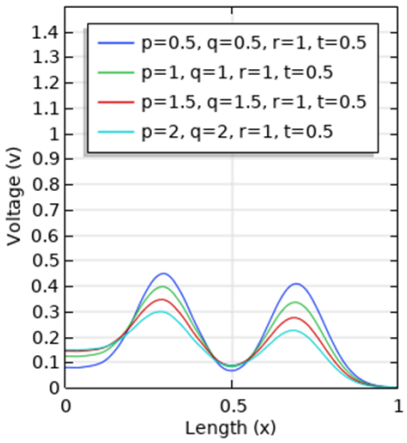

(b) Transmission velocity $r = 1$ and time $t = 0.5$

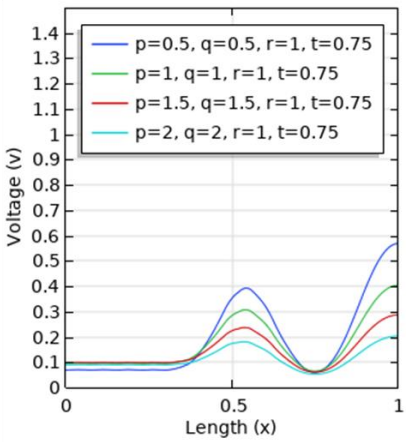

(c) Transmission velocity $r = 1$ and time $t = 0.75$

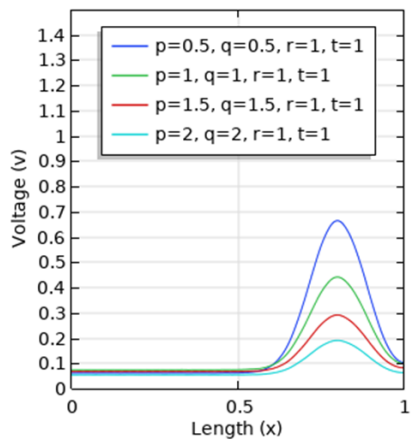

(d) Transmission velocity $r = 1$ and time $t = 1$

Fig. 4 Different pulse shape for $r = 1$ and $t = 0.25, 0.5, 0.75, 1$.

3.1 **Case-1:** Transmission Velocity $r = 1$ and Time Slot $t = 0.25, 0.5, 0.75, 1$

We have investigated the voltage variation for the damping factors i.e. $p + q$, ranging from 1 to 4 for the transmission velocity $r = 1$, and time slots ranging from $t = 0.25$ to $t = 1$. Our curiosity was to observe how the changes are increasingly occurring at several times for the same value of r and intentionally allowed the damping factor to vary. The consequences observed are numerically sketched in Fig. 4.

In Fig. 4(a), we have depicted the pulse shape for a specific time slot $t = 0.25$, $r = 1$, the damping coefficients starting from $p = 0.5 = q$ to $p = 2 = q$ with evenly spaced and enhanced. A significant variation of decrease of pulse height was observed at nearly quarter length of the propagation of the transmission. The increase in damping coefficients caused the pulse to increase again for a small length of the transmission line and then with a dramatic decrease in the height of the pulse height.

The increase of time for the same transmission velocity and the gradual variation of p and q causes an interesting observation as shown in Fig. 4(b). For the time slot $t = 0.5$, we observed a symmetric up and down of the pulse with the symmetric variation in between the damping factors themselves. A smooth variation with the fashion of increase and decrease of pulse with the propagation of the transmission makes a sensation in the observation. Exactly at the middle of the propagation of the length of the wire, there is a significant variation of the down of the pulse, and an evenly spaced increased pulse was observed. The pulse has applied the same ratio of height for the varying damping factors. A smooth sequence of observations enhanced the curiosity to increase the time with the fashion of varying damping coefficients and with the fixed transmission velocity.

With the enhancement of time, we observed that the deformations are quickly occurring in the pulse shape. Transmission velocity $r = 1$ and time $t = 0.75$ with the gradual enhancement of damping coefficients in an evenly spaced manner causes deformation pronounced significantly at the initial point of the graph. It seemed that there is a coincidence with more than two pulse heights coming from different damping parameters and as the transmission propagates along the wire, the pulse height starts increasing at nearly the middle of the length. The height then went down again and seemed to intersect at a certain point. And the interesting matter happens later when the height of the pulse increases to a greater extent with the varying parameters of the values of p and q. These variations and insight attributes have been analyzed in Fig. 4(c).

While quite eye-catching variations were noticed in Fig. 4(d) for the time slot $t = 1$. Here, the deformation is observed at a quite distance length of the transmission. We interestingly observed the very nearest coincidence of the propagation of the transmission of all the damping factors although were varying at a value of $p = 0.5 = q$ for the fixed time slot and fixed transmission velocity up to a very wide length of the wire. The pulse increased later maintaining a ratio among the factors occurring for different curves and then damped down again.

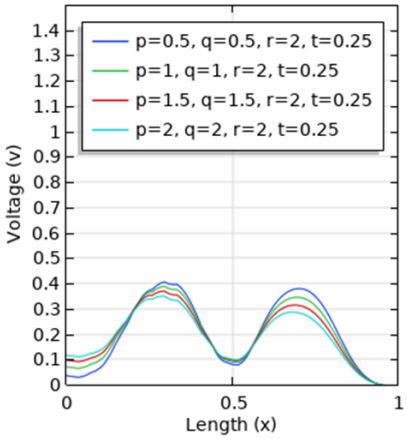

(a) Transmission velocity $r = 2$ and time $t = 0.25$

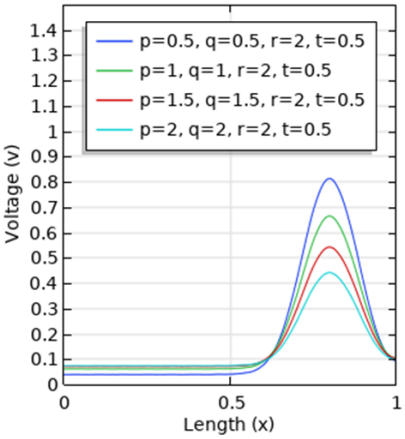

(b) Transmission velocity $r = 2$ and time $t = 0.5$

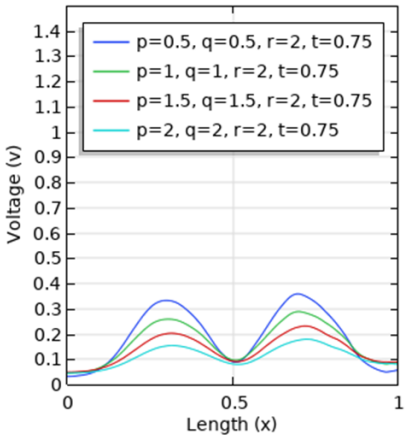

(c) Transmission velocity $r = 2$ and time $t = 0.75$

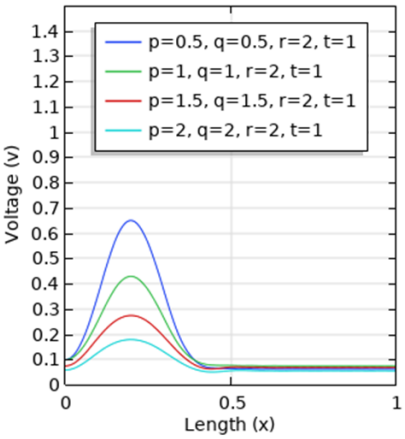

(d) Transmission velocity $r = 2$ and time $t = 1$

Fig. 5 Different pulse shape for $r = 2$ and $t = 0.25, 0.5, 0.75, 1$.

3.2 **Case-2:** Transmission Velocity $r = 2$ and Time Slot $t = 0.25, 0.5, 0.75, 1$

Our first observation for the time slot $t = 0.25$ for the earlier stated case-2 parameters variation is found in Fig. 5(a). A massive variation was observed at the beginning. Pulses emerging at a specific ratio with increasing pattern cause damping up symmetric behave and similar damping down symmetric exactly at the middle length propagation of the wire. It produced a similar increasing smooth pulse later with the propagation of time. A massive sensation of the pulse was observed in this case. A variation quite different from Fig. 5(a) is observed in Fig. 5(b) due to the increase of time and specified time slot $t = 0.5$. A constant pulse height happened more than halfway through propagation. A sudden and significant pulse height was observed for the damping varying factors later and damping down height smoothly. At time slot $t = 0.75$, a comprehensive observation followed in Fig. 5(c). There observed a symmetry shape of pulse height in the neighborhood of the middle length of propagation and the converging of the height at a point when the transmission propagates the half-wire length. The smoothness of the curve was also observed more soundly. Fig. 5(d) depicts the pulse shape for case-2 for the time slot $t = 1$. We observed a scattered shape at the beginning and a coincidence emerging from the half-length propagation.

3.3 **Case-3:** Transmission Velocity $r = 3$ and Time Slot $t = 0.25, 0.50, 0.75, 1.00$

Likewise, in case-1 and case-2, for the fixed time slots and variation of damping coefficients with a high velocity of transmission $r = 3$ was numerically observed and is described in Fig. 6. The increase of transmission velocity and a gradual increase of damping factors occurring with the desired time slots caused the scattered pulse height as shown in Fig. 6. It is kept mild for $t = 0.25$ and $t = 0.5$, and then a more scattering pulse heigh is found for $t = 0.75$. The highly scattering pulse height is seen in Fig. 6(d) at the propagation for the time slot $t = 1$. An interesting matter happened in the time slot $t = 0.5$ as shown in Fig. 6(b), and a scatter pulse with a smooth and symmetric deformation is observed.

We curiously continued the simulation for the increasing time and observed the pulse height was scattering significantly with the significant increase of the damping factors along with the desired time slots for high transmission velocity. The scattering phenomenon is widened with time.

Now, it is evident that the transmission velocity plays a significant role in the analysis of variation of damping coefficients over the pulse height for the propagation along the Telegraph wire.

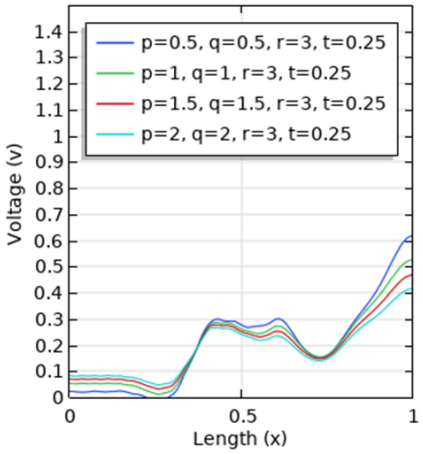

(a) Transmission velocity $r = 3$ and time $t = 0.25$

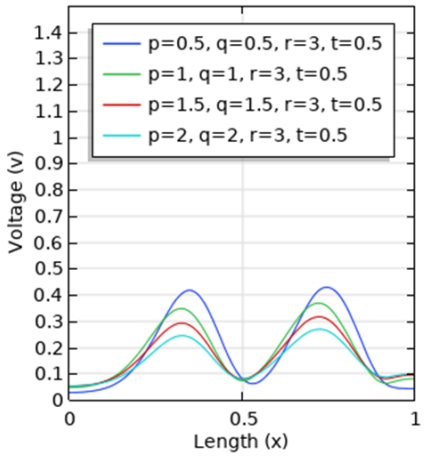

(b) Transmission velocity $r = 3$ and time $t = 0.5$

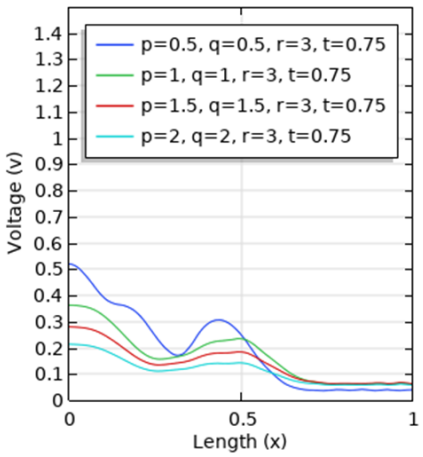

(c) Transmission velocity $r = 3$ and time $t = 0.75$

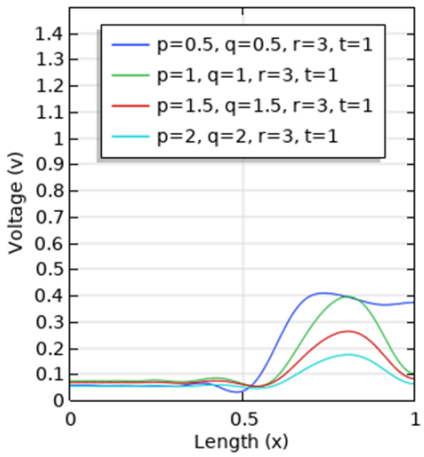

(d) Transmission velocity $r = 3$ and time $t = 1$

Fig. 6 Different pulse shape for $r = 3$ and $t = 0.25, 0.5, 0.75, 1$.

4 Findings

A comprehensive numeral simulation of the Telegraph equation based on the variations in the corresponding parameters resulted in some momentous outcomes. The damping coefficients reflect the pulse height up and down with their gradual shifting points. The time effects for stretching and compression of the pulses from left and right and vice versa for the regular shape of the pulse with lower transmission velocity. The effect of transmission velocity causes the pulses to regular for their smaller values and a quite irregular shape with the increasing values and finally, a scattered occurring while the transmission velocity reaches $r = 3$. For $r > 3$, a very scattered and complete irregular shape of the pulse heights will be forthcoming. Of all the reflections played over the pulse height, the effect of transmission velocity is quite remarkable and sounding.

5 Comparative Discussion

Since we comprised the current work with an unorthodox vision, it is arduous to compare it with the other works. Most of the works referenced in the introductory section are analytical or semi-analytical, some of the works include numerical simulations with so-called numeric calculations and manual or user-defined sketching techniques. In contrast, the approach implemented in this work is completely machine-based simulations incorporating automated graphing integrity with a programmable interface, which is computationally efficient. As we have aimed to investigate the impact of parametric variations on the pulse height (associated voltage), no solution function of explicit evaluation is required. So, the numerical approach embedded in this work is efficient for time-saving ability, which can be applied with the minimum memory requirement of the computing machine. Moreover, for different initial and boundary conditions, analytical methods need to be restarted, on the contrary, Comsol Multiphysics-based numerical simulations need to change the conditions expediently. So, the Telegraph equations with volatile features can be efficiently analyzed with the numerical simulations discussed in this work.

6 Conclusion

In this paper, we have investigated the parametric behavior of the Telegraph equation. The numerical solution has been manipulated using COMSOL Multiphysics. We analyzed a Telegraph wire of a small section and studied the pulse of voltage while moving along it. We used the parametric sweep method that gives results and shows the shape of the pulse for varying damping coefficients over several discrete time slots. We observed the changes occurring in the variation of transmission velocity. We allowed the damping coefficients to vary and kept the transmission velocity remain fixed for some specific cases then gradually increased the time slots. Then we allowed the transmission velocity to increase and kept it fixed as before and allowed the parameters p and q increasing and observed the changes at different time slots. Although the damping coefficients increased at several discrete time slots, the pulse height was smooth, symmetric, and regular for the smaller transmission velocity, for instance, $r = 1$ and $r = 2$. But the greater transmission velocity caused the pulse height to be irregular and highly scattered. A dramatic change was observed in the pulse shape for $r = 3$ which was throughout the transmission line. It is observed that pulse height is smooth, with a regular up and down for the smaller values of r irrespective of the enhancement of the damping coefficients at the different time slots. The scattered shape of the pulse height appears as the transmission velocity increases irrespective of the enhancement of the damping coefficients at the different time slots. We hope the parametric behavioral observations are intended to be used in our further research.

References

[1] Talib, E., Shin, J.H., Kwak, M.K. and Koo, J.R., 2019. Dynamic modeling and simulation for transmission line galloping. *Journal of Mechanical Science and Technology*, *33*(9), pp.4173-4181.

[2] Bhattacharya, J. and Maity, S., 2021. Investigating metallic rectangular waveguide using conformal mapping technique. *Journal of Electromagnetic Waves and Applications*, *35*(12), pp.1553-1563.

[3] Zhang, K. and Li, D., 2008. Transmission-Line Theory and Network Theory for Electromagnetic Waves. *Electromagnetic Theory for Microwaves and Optoelectronics*, pp.117-178.

[4] Yousefi, S.A., 2010. Legendre multiwavelet Galerkin method for solving the hyperbolic telegraph equation. *Numerical Methods for Partial Differential Equations: An International Journal*, *26*(3), pp.535-543.

[5] Lakestani, M. and Saray, B.N., 2010. Numerical solution of telegraph equation using interpolating scaling functions. *Computers & Mathematics with Applications*, *60*(7), pp.1964-1972.

[6] Dehghan, M. and Ghesmati, A., 2010. Solution of the second-order one-dimensional hyperbolic telegraph equation by using the dual reciprocity boundary integral equation (DRBIE) method. *Engineering Analysis with Boundary Elements*, *34*(1), pp.51-59.

[7] Srivastava, V.K., Awasthi, M.K., Chaurasia, R.K. and Tamsir, M., 2013. The telegraph equation and its solution by reduced differential transform method. *Modelling and Simulation in Engineering*, *2013*.

[8] Mittal, R.C. and Bhatia, R., 2013. Numerical solution of second order one dimensional hyperbolic telegraph equation by cubic B-spline collocation method. *Applied Mathematics and Computation*, *220*, pp.496-506.

[9] Tautz, R.C. and Lerche, I., 2016. Application of the three-dimensional telegraph equation to cosmic-ray transport. *Research in Astronomy and Astrophysics*, *16*(10), p.162.

[10] Arora, G. and Joshi, V., 2016. Comparison of numerical solution of 1D hyperbolic telegraph equation using B-spline and trigonometric B-spline by differential quadrature method. *Indian Journal of Science and Technology*, *9*(45), pp.1-8.

[11] Huseen, S.N., 2017. A numerical study of one-dimensional hyperbolic telegraph equation. *Journal of Mathematics and System Science*, *7*, pp.62-72.

[12] Stojanović, Z. and Čajić, E., 2019, November. Application of Telegraph Equation Soluton Telecommunication Signal Trasmission and Visualization in Matlab. In *2019 27th Telecommunications Forum (TELFOR)* (pp. 1-4). IEEE.

[13] Khan, H., Shah, R., Baleanu, D., Kumam, P. and Arif, M., 2019. Analytical solution of fractional-order hyperbolic

telegraph equation, using natural transform decomposition method. *Electronics*, *8*(9), p.1015.

[14] Hashemi, M.S., 2019. Numerical solution to the telegraph equation via the geometric moving Kriging meshfree method. *The European Physical Journal Plus*, *134*(8), pp.1-8.

[15] Zhou, Y., Qu, W., Gu, Y. and Gao, H., 2020. A hybrid meshless method for the solution of the second order hyperbolic telegraph equation in two space dimensions. *Engineering Analysis with Boundary Elements*, *115*, pp.21-27.

[16] Maystre, D., 2014. Maxwell: A new vision of the world. *Comptes Rendus Physique*, *15*(5), pp.387-392.

[17] Alias, R., 2014. Multilayer glass–ceramic composites for microelectronics: processing and properties. In *Advances in Ceramic Matrix Composites* (pp. 587-610). Woodhead Publishing.

[18] https://en.wikipedia.org/wiki/Transmission_line. Accessed on 20th June 2022.

[19] Wagner, J.M., Rißland, S., Schütt, A., Carstensen, J. and Adelung, R., 2017. Distributed series resistance in a one-dimensional two-diode model revisited. *Energy Procedia*, *124*, pp.197-206.

[20] Breit, G., 1921. The distributed capacity of inductance coils. *Physical Review*, *17*(6), p.649.

[21] Abedini, M., Davarpanah, M., Sepehr, A. and Ajaei, F.B., 2020. Shunt capacitor bank: Transient issues and analytical solutions. *International Journal of Electrical Power & Energy Systems*, *120*, p.106025.

[22] Srivastava, V.K., Awasthi, M.K., Chaurasia, R.K. and Tamsir, M., 2013. The telegraph equation and its solution by reduced differential transform method. *Modelling and Simulation in Engineering*, *2013*.

[23] Mollahasani, N., Moghadam, M.M.M., and Afrooz, K., 2016. A new treatment based on hybrid functions to the solution of telegraph equations of fractional order. *Applied Mathematical Modelling*, *40*(4), pp.2804-2814.

[24] Kumar, D., Sing, J. and Kumar, S., 2014. Analytic and approximate solutions of space-time fractional telegraph equations via Laplace transform. *Walailak Journal of Science and Technology (WJST)*, *11*(8), pp.711-728.

[25] Partohaghighi, M., Akinlar, M.A. and Weber, G.W., 2021. New solutions of hyperbolic telegraph equation. *Journal of Dynamics & Games*, *8*(2), p.129.

[26] Saadatmandi, A. and Dehghan, M., 2010. Numerical solution of hyperbolic telegraph equation using the Chebyshev tau method. *Numerical Methods for Partial Differential Equations: An International Journal*, *26*(1), pp.239-252.

SciEn
Journal of Engineering Advancements Vol. 03(03) 2022, pp 112-130 https://doi.org/10.38032/jea.2022.03.006

Prioritization of Effective Lean Tools for Reliability Analysis and Maintenance Strategy

*Sadia Tamanna** *and M. Mishkatur Rahman*

Department of Industrial Engineering and Management, Khulna University of Engineering & Technology, Khulna-9203, Bangladesh.

Received: March 25, 2022, Revised: August 16, 2022, Accepted: August 17, 2022, Available Online: September 28, 2022

ABSTRACT

Asset or equipment reliability and availability have occupied extensive attention because of an emerging competitive environment and the overall operating and production cost. The main focus of this manuscript is to prioritize the lean tool and select an appropriate maintenance strategy for the repairable assets in the maintenance shop of the SIMGA[1] shipyard. Five (5) assets of that maintenance shop such as an air compressor machine, 500-ton press machine, overhead crane machine, VDF lathe machine, and Roller machine were under breakdown maintenance. Due to the continuous degradation of those assets, attempts should be taken to enhance the reliability parameters by predicting upcoming failure events for each equipment or asset. QFD-AHP is a rapid tool in which quality function deployment is integrated with AHP to make an optimal selection. Firstly, the integrated QFD-AHP method is employed to prioritize the lean tools for that maintenance shop. 5S and KPI are the best fit for that shop among ten lean tools. Non Homogenous Poisson Process (NHPP) is a model which represents the no. of failure experienced up to time (t). NHPP and Weibull analysis are utilized to predict future failure events and analyzed the nature of the failure accordingly. From the results of the Weibull analysis and NHPP analysis, it is shown that the slope (β) of the failure rate is greater than 1 for all assets. Overhead crane m/c and 500-ton press m/c are the most critical m/c according to equipment criticality analysis. Finally, a decision diagram is utilized to extract the most congruent maintenance strategies based on the reliability parameter of five (5) assets. The approach employed in this study helps maintenance practitioners to achieve lean maintenance.

Keywords: Reliability, Availability, Weibull Analysis, Non-homogenous Poisson Process, QFD-AHP, Maintenance Excellence, MTBF.

1 Introduction

Maintenance is defined as the activity obtained to confirm that an asset or equipment performs its intended function and maintains the actual production requirement. Moreover, the reduction of cost and the enhancement of the asset or asset reliability and performance will be acquired by the execution of a standard maintenance policy. The longevity of the asset might be expended with a huge profit on investment by the execution of little changes in the strategy for maintenance. Several factors must be optimized which affect the reliability and availability. To get good profitability the level of reliability and availability of machinery should be high. The availability and reliability of the machine may influence the effectiveness of the asset. As the size and equipment complexity is increasing, the implications indication of equipment failure has become more critical. Equipment or facility failure turns not only productivity loss but also quality loss. Since it is not possible to prevent failure entirely, the probability of occurrence as well as failure impact can be minimized by a maintenance strategy. It is considered one of the important roles of reliability analysis and maintenance.

Quality function deployment-Analytic Hierarchy Process (QFD-AHP) that gains wide acceptance for using the Analytic Hierarchy Process with associated techniques as Quality Function Deployment in multiple decision-making problems. This approach is pursued to enhance the effectiveness of the decision-making process. Sometimes, it is applied to deal with subjective linguistic judgments in location problems and to evaluate the effectiveness of the hardware. QFD-AHP approach is used in the area of lean thinking, particularly in the maintenance environment [1].

In reliability application, the Weibull distribution is ordinarily applied as a longevity distribution. It describes a constant, decreasing, or increasing failure rate. The three parameters of this distribution are β, η, and ϒ which are known as the shape parameter, the scale parameter, and the location parameters accordingly. A Weibull distribution having two parameters can be expressed as W (β, η). The Probability density function with time is represented by it [2]. In three-parameters Weibull distribution, eta (η) represents characteristic life at which it is assumed that 63.2% of the sample failed. Beta (β) determines what the Weibull probability density function looks like. It is also positive Gamma (ϒ) is a location parameter. It is called failure-free time or a guaranteed time. The recognition of the mode of failure for an asset is exhibited by the beta value. It is necessary for choosing the appropriate maintenance strategy. By the use of Weibull analysis software, it is checked whether the data follows a distribution of Weibull or not. This can be determined by the use of the Weibull probability plot where data is manually plotted. If the data is conforming to a Weibull distribution, a plot gives a straight line. Different beta values represent the following Weibull parameter and reliability matrix conditions [2].

1) $\beta < 1$, it represents infant mortality. A new part is not acceptable. An old part is better than a new part because the failure rate is lower as weak units have been eliminated from the population.

*Corresponding Author Email Address: sadiasony@baust.edu.bd

2) $\beta = 1$, it represents chance failures. An old part has the same failure rate as a new part. Thus, nothing is gained by a replacement strategy that throws away unused life until the failure mode changes to a wear-out mode.
3) If $\beta=1$, there must have an optimum replacement strategy if the cost or safety consequences have a very high-cost ratio for an unplanned failure compared to a planned replacement cost which then drives a preventive replacement strategy.

Non-homogenous Poisson process is a process along with a simple parametric model used to represent events with a failure recurrence that are not constant [3]. It does not require stationary increments, which means that failures may be more likely to occur at certain times. NHPP describes the cumulative number of failures up to time (t) and it follows a Poisson distribution with parameter λ (t) for a counting process. NHPP model works when the occurrence rate depends only on time and stationary increment is not required. Data acquisition is simpler for C-A plots than for Weibull plots. For C-A plots, chronological time is on the x-axis. It is also named the cumulative number and the y-axis is named as cumulative events, reliability is made visible by them. When plotted, this data usually provides results in a straight line [4]. After plotting, this data gives information about two statistics. These are line slope β, and y-axis intercept at time t=1, λ. The slope β for the trend line is a potential indicator that gives information about increasing or decreasing. The y-axis provides the failure rate at a time equal to 1, which is some kind of hypothetical value by that it is easy to forecast future failure. For plotting cumulative mean time vs. cumulative time, Y-axis is converted which is simple and easy to understand. When the line slope (β) is going upward and to the right, it indicates that reliability is improving; when it is downward and to the right, it indicates that reliability is decreasing.

A maintenance strategy guides the maintenance activity. A maintenance strategy is divided into three categories. These are preventive maintenance, design out maintenance as well as corrective maintenance. Design out maintenance which aims at altering the design of the asset or product for reducing the requirement for maintenance in the period of the life cycle. Preventive maintenance is considered as maintenance which is carried out at scheduled intervals by the prescribed criteria. It is intended to minimize the probability of degradation or failure of an item. This maintenance is further divided into two maintenance those are time-based maintenance as well as condition-based maintenance [4]. Preventive maintenance is an appropriate choice if the component has a progressive failure rate which indicates the failure rate and the cost of the preventive maintenance action should be less than the total cost of corrective maintenance. Condition-based maintenance is called prediction-based maintenance which is applied to an item where failure occurs accidentally. The inspection period must be presented to enhance the reliability of facilities by using MTF. Corrective maintenance can be defined as the maintenance which is carried out after identifying a fault. It is intended to keep an item in such a state in which it may perform a required function.

In this study, a survey was carried out in the maintenance shop of the SIGMA shipyard. The foundation of the study was the survey result. In the QFD model, survey results were the input. Another set of input was necessary for developing the model which was obtained from the lean thinking literature study. Another endeavor was taken to determine the asset reliability by using the Weibull distribution & PTC Wind-chill Quality Solutions 11.0 Tryout “software. The reliability model from the NHPP analysis predicts the future failure events that will occur. The purpose of this study is to describe the method of reliability and availability analysis of a repairable asset and explore the method for improving asset availability by managing the effort using availability importance measures of each component. This analysis will also be studying the criticality of the asset for continuous improvement

The main objectives of this study are:

1. To prioritize the lean tool to achieve lean maintenance.
2. To predict upcoming failure events for each asset by using reliability analysis.
3. To develop a decision diagram and select an appropriate maintenance strategy for each asset by using reliability analysis and equipment criticality analysis.

The Limitation of the Study-

The limitations of the manuscript are given below, which are

1. Only the repairable assets are analyzed.
2. A limited number of failure data are available for the analyzed assets.
3. Data censoring and truncation are not considered.

2 Literature Review

2.1 Lean Maintenance

Maintenance, a significant function, helps an organization for achieving its strategic objectives. It serves the production facility with a guarantee of high productivity. Several maintenances have been introduced to meet specific maintenance needs. Integrating lean tools into maintenance functions can improve maintenance efficiency resulting in increasing reliability, safety, quality, and availability of equipment’s production. Maintenance constitutes a significant share of operating costs in the industry. They proposed a road map to use lean thinking in maintenance functions [5]. Eight types of wastes, a scheme of lean maintenance practices and maintenance, and value stream mapping, were the scope of their work. To collect the recent maintenance philosophies and functions, lean tools, and principles in maintenance, they conducted an exhaustive literature review. Lean maintenance philosophy was driven for thriving maintenance efficiency in Thermoelectric Power Plants. The experience gathered from their approach was presented in two projects in that thermoelectric power plants. The lean techniques were constructed using a previously developed decision-making process in which the variation of the criteria was diverse that applied the Fuzzy AHP methodology to perform diagnosis and prescription tasks. This procedure permitted the application of the most appropriate lean tools to solve deficiencies in maintenance tasks. The results indicated that the maintenance function might be made more efficient and lean by using a lean technique [6]. A framework was provided to detect and calculate the usefulness of the maintenance policy embedded in the lean thinking approach for ratings of the various components of the maintenance department. DEMATEL layout on maintenance strategy was used as a guideline to develop the framework [7].

2.2 Quality Function Deployment (QFD)

The method of QFD was first exhibited in 1966 in Japan to transform the customer requirements into engineering requirements of a product. QFD is composed of two fundamental parts that are applied to the design process. A case was carried out a case study in the canning industry by relating lean attributes with lean enablers. They employed QFD to determine key LEs

to enhance the leanness of the food chain. To deal with linguistic judgments needed in QFD, they used Fuzzy logic. An illustration of the practicality of this approach was exemplified with the help of a case study [8]. An approach was developed to identify the most suited enablers to be implemented by linking agile attributes and agile enablers. The approach was dependent on the quality function deployment (QFD) methodology, especially on the house of quality (HOQ). Fuzzy logic was used to transform linguistic judgments [3].

2.3 Analytic Hierarchy Approach

AHP, a structured technique, is a tool for analyzing complicated decisions with the help of mathematics and psychology. It is widely used throughout the world for prioritizing complex decisions. It provides a framework for constructing decision problems and quantifying their elements. A decision-making approach, AHP was first developed by Thomas L. Saaty. Detailed literature was provided to review versatile applications of AHP highlighting how broadly the process had been used. The study showed that AHP had been used in engineering, study, government, industry, and so on [9]. A brand-new procedure was proposed for rank preservation based on the judgment matrix consistency [4].

2.4 QFD-AHP Approach

The combined QFD-AHP approach is a useful tool for the selection and prioritization of organizational objectives. It can be extensively used in the maintenance context for selecting the appropriate lean tools and comparing them. It facilitates the acceptance of the decision-making process that provides a suitable option to select. A combined AHP-QFD was used for analyzing decision alternatives for a facility location problem rather than using a standalone AHP approach [10]. QFD-AHP method was applied for a new facility location problem where AHP was used to evaluate the relative importance of every location requirement. QFD-AHP approach was applied for the evaluation of different hardware of a mobile station. It was found that the QFD-AHP approach is better than the quality or price ranking method [2]. Many instances had provided where the QFD-AHP had been used successfully such as improving the quality, project selection, determining the composition, and also in new product development [11]. Quality Function Deployment (QFD) and Analytical Hierarchy Process (AHP) was used to enhance the decision-making processes in the maintenance function [1]. Before this, the approach was rarely used in lean thinking, especially in a maintenance environment. Their work enriched the application of this approach by using it to determine the importance of ME and how they were related to lean thinking. A survey was conducted on a maintenance department in the railway environment. The output of their effort resulted in a group of prioritized lean tools addressing a group of prioritized maintenance excellence.

2.5 Reliability Analysis

Among all other statistical models, the Weibull distribution and Crow-Army Material Systems Analysis Activity (AMSAA) are applied to prophesy the failure events of a component or an asset. The Weibull distribution is a strong tool for single mode failure whereas the Crow-AMSAA works well with the mixed failure modes. Two analyses (Weibull distribution and NHPP) are compared in this paper. These are applied to examine the cable joint failures. The methods of applying models to investigate the data of failure and to forecast upcoming failures were discussed in the preliminary section of their research. The data were collected from a local power supply company and included 16 failures and 1126 suspensions. This outcome of this manuscript claimed that the outcome of the Weibull distribution is more reliable [12]. NHPP was employed to forecast the failures of the upcoming future by using Microsoft Excel. The outcome of the study concluded that this template assisted a user to know about the upcoming degradation events that result in an increase in MTBF by adopting the correct action timely. A case study was conducted in this manuscript to illustrate the function of NHPP plots for centrifugal pumps using MS Excel. The outcome depicted that failure events for the next could be calculated successfully [13]. The Weibull and Crow-AMSAA model are statistical models used extensively in reliability analysis. The two models were compared and used in their work for the analysis of the cable failure data obtaining the prediction of the failures in the future. This study concluded that the outcome of the Weibull model gives a more reliable outcome than the Weibull and NHPP model whereas the amount of failure data is small [14].

2.6 Maintenance Strategy

A reliability-based case study was carried out in a crushing plant. The Weibull ++ was used to estimate the parameter. The failure pattern was analyzed for the improvement of the machine. A reliability-based maintenance policy was developed. The study indicated that the analysis of reliability plays a significant role in deciding on maintenance policy. A maintenance schedule was developed. They identified the characteristics of the parameter of the asset. They also suggested a maintenance policy [3]. The Distribution feeder was prioritized by a new model for RCM. They presented a reliability index model in their manuscript. This was done by determining critical components for deciding the asset performance. For the enhancement of cost-effectiveness. A Maintenance schedule was proposed for the offshore wind asset. They determined optimal individuals and grouped various maintenance schedules and various parameters were considered for this purpose [15]. A maintenance policy was selected policy by applying a fuzzy ANP approach [16].

3 Methodology

The methodology started with the analysis of the QFD-AHP approach for prioritizing the lean tool, then reliability analysis was performed on five assets discussed in the analysis section. It began with a questionnaire which was the foundation of our study. A flow chart is given in Fig. 1.

3.1 Prepare a Survey Question based on Maintenance Excellence Criteria

A survey question is prepared based on maintenance excellence criteria [1]. Maintenance excellence criteria are listed in the analysis section. This qualitative questionnaire consists of 10 questions. Each question has 5 options and these are excellent, good, average, poor, and bad (See Appendix A). The results of the survey are used to compare ME.

3.2 Rank Lean Tool for Maintenance using QFD-AHP

Maintenance lean tools are listed in the next section based on the literature survey. A relationship matrix was developed by the ME and a lean tool by the QFD approach. A rating was given to each relation between ME and the lean tool. The Analytic

hierarchy approach was used to determine the importance rating of each ME. The detailed QFD–AHP approach is described in the analysis section. A flow chart of the QFD–AHP approach is given in Fig. 2.

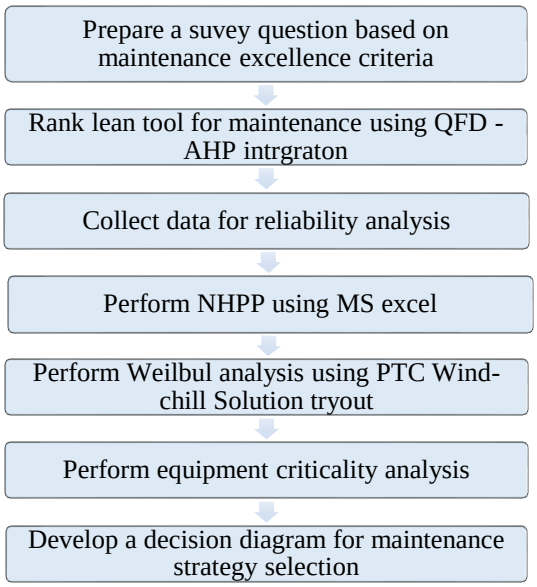

Fig. 1 Methodology of the study.

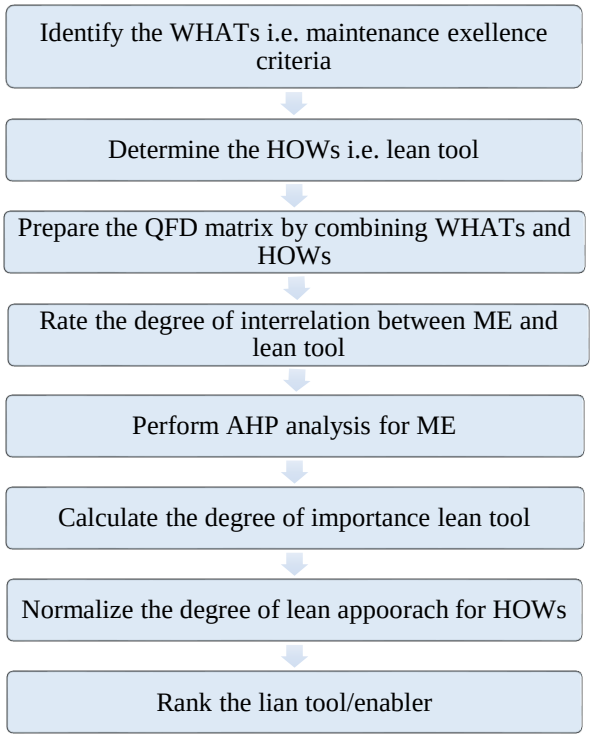

Fig. 2 An integration of QFD-AHP analysis

3.3 Collect Data for Reliability Analysis

After performing QFD–AHP analysis, reliability analysis was performed to measure the asset's availability and reliability. Data was gathered from the SIGMA shipyard. The data was collected for 10 assets. These were the air compressor machine, 500-ton press machine, overhead crane machine, VDF lathe machine, roller machine, planer machine, shaper machine, mixer machine, mixer machine, bearing machine, and paramak generator which were under breakdown maintenance. The date of failure and mean time to repair (MMTR) were collected from the logbook. Due to the lack of data, the reliability analysis was performed on five assets which are an air compressor machine, 500 press machine, overhead crane machine, VDF lathe machine, and roller machine. The historical data on those machines are given in Appendix B.

3.4 Perform NHPP analysis

NHPP analysis was performed to predict future failure events. Microsoft Excel was used for this purpose. In detailed analysis is described in a later section.

3.5 Perform Weibull Analysis

Weibull analysis was performed to determine in which state of the life cycle of equipment when failure has occurred. The results of this study were useful to choose the appropriate strategy for maintenance. The Weibull parameter was determined by the PTC Wind-chill Quality Solutions 11.0. This analysis is also described in a later section.

3.6 Perform Equipment Criticality Analysis

Equipment criticality analysis was performed to determine to what extent the equipment was critical in terms of production, safety, cost, and availability measures.

3.7 Develop a Conceptual Model for Maintenance Strategy Selection

A developed conceptual model was modified to select an appropriate maintenance strategy for each asset. This model was developed by the Weibull parameter and equipment criticality.

4 Data Analysis

This study was started with a survey in the machine shop of the SIMGA1 shipyard. A survey questionnaire was prepared based on maintenance excellence criteria [1]. This qualitative questionnaire has 10 questions. Each question has 5 options and these are excellent, good, average, poor, and bad (See Appendix A). The response to that questionnaire was collected from the experts of the machine shop of the shipyard.

Maintenance Excellence criteria: Step 1 was to define ME for the asset. By the theoretical evidence, the criteria for ME were approved. Then AHP had been employed to rank the ME. The list of ME selected for the study is given below -.

1. Spare Parts and Material Availability(SP)
2. Performance Indicators(KPI)
3. Policy and Strategy(PS)
4. Comprehensive Work Orders(CWO)
5. Organization clean up and tiding of work field areas(OCT)
6. Reduction in intervention number(RIN)
7. Reduction in process variability(RPV)
8. Implementation of preventive maintenance(PM)
9. Continuous controlling and monitoring of procedure and improving efficiency(CMPANDIE)

Lean tool selection: Step 2 was to extract a lean tool that fits maintenance standards. These lean tools were recognized from the literature. These are the input of the QFD diagram. The list of lean tool for maintenance obtained from the paper are given below:

1. Total productive management
2. Standard operating procedure

3. Single-minute exchange dice
4. Kaizen
5. Kanban
6. 5S
7. VSM (value stream mapping)
8. Key performance indicator
9. Statistical process control
10. Visual management

Rank lean tool for maintenance using QFD – AHP: The maintenance lean tool was listed based on the literature survey. A relationship matrix was developed by the ME and lean tool. AHP was used to determine the importance rating of each ME. Then the importance weighting was multiplied by rating to determine the importance degree of the lean approach. A relation matrix was developed where weak relationships, medium, and strong relationships were indicated by a white circle, rectangle, and black circle. The weak, medium and strong relationships were quantified by 1, 3, and 9 respectively. Using AHP analysis, the improvement weight of each maintenance excellence was calculated. The final QFD-AHP analysis is shown in Table 1 and the consistency ratio was also calculated for the validation of the AHP analysis shown in Table 2.

Table 1 Final ranking matrix by QFD-AHP analysis

○ Weak relationship ▭ Medium relationship ● Strong relationship	TPM (Total Productive Maintenance)	Standard Operating Procedure	SMED (Single minute exchange dice)	Kaizen	Kanban	5S	VSM (Value Stream mapping)	KPI (Key Performance Indicator)	SPC (statistical Quality Control)	Poka-yoke	Visual management	Improvement weight
Spare parts and Material availability	▭			○	●	▭						0.046
Performance indicators				●		▭		●		▭	●	0.031
Policy and strategy				▭		●		●			●	0.078
Comprehensive work orders				○	▭	●					▭	0.118
Organization clean up and tiding of work field areas	▭					●	○					0.387
Reduction in intervention number	▭		●		▭			●		▭		0.119
Reduction in process variability	▭	●							●			0.126
Implementation of preventive maintenance	●	●						▭				0.024
Continuous controlling and monitoring of procedures and enhancing efficiency			●			○	▭	▭	▭	▭		0.07
Importance degree of the lean approach	1.87	1.35	1.70	.68	1.13	5.5	.59	2.33	1.34	0.66	1.14	=18.3
Normalized importance degree	0.10	0.07	0.09	0.03	0.06	0.3	0.03	0.12	0.07	0.04	0.06	
Rank	3	5	4	8	6	1	8	2	5	7	6	

Table 2 Consistency ratio calculation

	SP	KPI	PS	CWO	OCT	RIN	RRV	PM	CMPANDIE	**Priority weight**
SP	1	1/3	1/3	1	1/7	1	1	3	1	0.050
KPI	3	1	1	1/3	1/7	1/3	1/3	3	1/3	0.031
PS	3	1	1	1/3	1/7	1/3	1/3	3	3	0.078
CWO	1	3	3	1	1/3	1	1	3	1	0.118
OCT	7	7	7	3	1	5	3	7	3	0.387
RIN	1	3	3	1	1/5	1	1	5	1	0.119
RPV	1	3	3	1	1/3	1	1	5	1	0.126
PM	1/3	1/3	1/3	1/3	1/7	1/5	1/5	1	1/5	0.024
CMPAN DIE	1	3	1/3	1	1/3	1	1	5	1	0.070
Total	18 1/3	21 2/3	19	9	2 7/9	10 6/7	8 7/8	35	11 1/2	
SUM PV	1	2/3	1 1/2	1	1	1 2/7	1 1/9	5/6	4/5	
λ_{max}	9 1/5									
CI	0.03									
CR	0.02									

Table 3 Data input section and result table for the overhead crane machine

Overhead Crane Machine								
Result Section			**Data Input Section**					
Input data			No of failures	Time between failure	Cum. Failure time	Cum MTBF	ln (Cum. Failure Time)	MTTR
No. of failure (n)		10						
End of observation time (T)		1134 days	1	145	145	145.00	4.98	6
Availability		0.9399	2	130	275	137.50	5.62	7
Sum ln(Cum. Failure time)		63.51	3	80	355	118.33	5.87	8.5
Estimated parameters			4	169	524	131.00	6.26	8
Slope (β)		1.46610	5	191	715	143.00	6.57	6
Lambda (λ)		0.000332/day	6	91	806	134.33	6.69	5
Calculations			7	79	885	126.43	6.79	5
Failure rate (instantaneous)	1200 days	0.0133	8	58	943	117.88	6.85	4
Instantaneous MTBF, 1/u(t)		75.34	9	86	1029	114.33	6.94	4
Cumulative failure N (t)	1200 days	10.865	10	16	1045	104.50	6.95	7
Cum. failure rate		0.0091	11	83	1128	102.55	7.03	3
Cum MTBF		110.449	12	70	1198	95.73	7.09	5
Prediction to next failure			13	43	1241	87.82	7.12	6
Next failure occurrence (t)	n=11	1210.17 days	14	15	1256	81.91	7.14	3
Time to next failure (t)		76.1696 days	15	19	1275	68.27	7.15	4
						Sum	99.04	81.5

4.1 NHPP Analysis

NHPP modeling was performed to predict future failure events. Microsoft Excel was used for this purpose. NHPP plots were illustrated with the help of various software like Fulton 2006, WIN smith software, Blockish, and Weibull. The cost of this software is pretty high and very difficult to use. Microsoft Excel was very advantageous and common software used by nearly every organization for various purposes. A reliability model constructed using MS excel was simple to use and understand. It was a very simple way to predict upcoming failures with the help of this software. By this template, cumulative failure time was entered, and then it was automatically to find out what is the value of β. Some equations were used to determine the failure rate and the slope for the maximum likelihood equation:

For failure terminated test,

$$\beta = \frac{n}{(n-1)\, ln\, Tn - \sum_{i=1}^{n} ln\, Ti} \quad (1)$$

For failure terminated test,

$$\beta = \frac{n}{n\, ln\, Tn - \sum_{i=1}^{n} ln\, Ti} \quad (2)$$

$$\lambda = \frac{n}{T} \qquad (Hence,\ T=total\ test\ time) \quad (3)$$

From the λ and β values, the instantaneous failure rate can be calculated by Eq. (4)**.** The Instantaneous failure rate,

$$\rho(t) = t^{(\beta-1)}\lambda\beta \quad (4)$$

The cumulative failure rate,

$$c(t) = t^{\beta-1}\,\lambda \quad (5)$$

The prediction of failure events,

$$N = \left(t_n{}^{\beta}\right) * \lambda \quad (6)$$

The events expected,

$$N=n\text{- }actual\ failures\ number \quad (7)$$

Table 3 shows the data input and result section of the air compressor machine. It was the first part in which cumulative failure time was given in a yellow shaded area. The other parameters were calculated by the use of a simple arithmetic equation. The result section is depicted in Table 3. After entering the observation, λ and β were calculated by using Eqs. (2) and (3). By Eq. (6), the next failure occurrence time was calculated. The instantaneous failure and cumulative failure times were calculated by this template at the given time. As in Table 3, the instantaneous failure rate was 0.0133 at a time 1210.17 days later. The slope (β) and failure rate (λ) of the rest of the machine were calculated similarly. The data input section with the result section for the rest of the machines (Air compressor machine, 500-ton press machine, VDF lathe machine, and Roller machine) are shown in Table B2-Table B5 accordingly.

4.2 Weibull Analysis

Weibull analysis was performed to determine the stage of the life cycle of mentioned assets in which failure occurred. The results of this study were useful to choose the appropriate strategy for maintenance. The Weibull parameter was determined by the PTC wind-chill solution tryout 11.

Reliability can be determined by the following equations

$$\text{Reliability, R (t)} = e^{(-\frac{t}{\eta})^{\beta}} \quad (8)$$

In two-parameter Weibull distribution, the failure rate function is described as the number of failures per unit of time. It is given as.

$$\text{Failure rate, } \lambda(t) = \frac{\beta}{\lambda} \times \left(\frac{t}{\lambda}\right)^{(\beta-1)} \quad (9)$$

The two-parameter Weibull probability density function f (t) is given as:

$$PDF = f(t) = \frac{\beta}{\eta} * \left(\frac{t}{\eta}\right)^{\beta-1} * e^{-\left(\frac{t}{\eta}\right)^{\beta}} \quad (10)$$

$$CDF = F(t) = 1 - e^{-(\frac{t}{\eta})^{\beta}} \quad (11)$$

The mean time of degradation-free operation till a failure event can be defined as MTTF for non-repairable systems and MTBF for the repairable system. The MTTF or MTBF of the Weibull PDF is given as

$$MTBF = E(T) = \Upsilon + \eta * \Gamma(\frac{1}{\beta} + 1) \quad (12)$$

Using the wind-chill quality solution 10.1 tryout software, the β, η, ρ is obtained and given in Table 4.

4.3 Equipment Criticality Analysis

Equipment criticality analysis was performed to determine to what extent the equipment was critical in the perspective of production, safety, cost, and availability of the asset. Criticality analysis is a tool that may be used to evaluate the impact of equipment failures on organizational performance. Three ratings (1, 2, and 3) were used where 1 indicates less impact, 2 indicates more impact and 3 indicates a strong impact on organizational performance. Ratings were given by the expert of that machine shown in Table 5. Hence, the equipment criticality for the overhead crane machine, 500-ton press machine, air compressor machine, VDF lathe machine, and roller machine is determined and given in Table 5.

The equation for calculating EC is given below

$$EC = (30P + 30S + 25A + 15V)/3 \quad (13)$$

where EC is the equipment criticality.

5 Maintenance Strategy Selection

There were several objectives of this study. But one of the objectives was to trace a maintenance technique. This might be manifested with the help of reliability analysis. Equipment criticality was another measure that was included in the decision diagram along with reliability measures. If equipment criticality was less than 40, then fixed maintenance was used according to the decision diagram. Because the cost of the fixed maintenance was less. If equipment criticality was less than or equal to 60% and 80%, then corrective-based maintenance and major overhaul (MHO) were selected respectively. Condition-based maintenance was a very costly maintenance plan among all the maintenance plans. A decision diagram was developed by using the value of β [3]. This decision diagram is modified by combining the value of equipment criticality. This decision diagram is shown in Fig. 3.

Table 4 Weibull analysis results

Machine Name	β	η	MTBF, days	Reliability, R (t)	Cumulative density function, CDF	Failure rate, λ (t)	Probability density function, PDF
Overhead crane machine	1.35	102.78	94.231	41.09%	49.00%	0.0127/day	0.005207
500-ton press machine	1.21	41.29	42.23	35.80%	64.20%	0.029 /day	0.01005
Air compressor machine	1.39	69.36	70.36	36.81%	63.10%	0.020/day	0 .0073
VDF lathe machine	3.16	86.23	87.12	35.6%	64.44%	0.037/day	0.0133
Roller machine	2.19	81.27	82.16	35.9%	64.10%	0.027/day	0.0098

Table 5 Equipment Criticality Analysis

Machine name	Impact on production(P)	Impact on safety(S)	Availability of standby (A)	Cost(V)	Machine's Criticality
Overhead crane machine	3	1	3	3	80.00%
500-ton press machine	2	1	3	2	65.00%
Air compressor machine	3	1	2	3	71.67%
VDF lathe machine	1	1	1	1	33.33%
Roller machine	1	1	1	1	33.33%

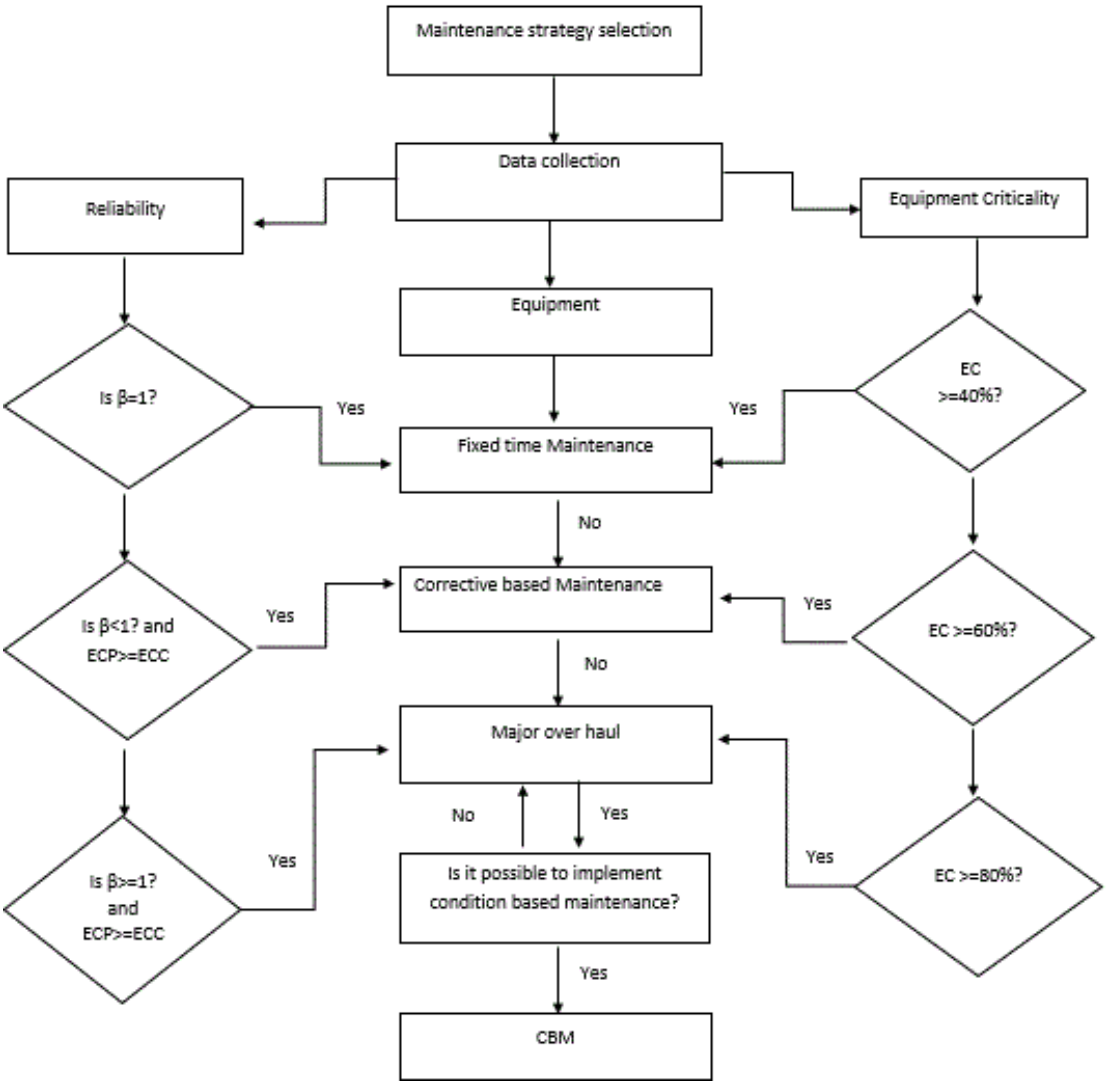

Fig. 3 A decision diagram

Hence, the value of β obtained from the Weibull analysis was greater than 1, so it was high time to replace the old one with the new one. It was also considered that the cost of equipment correction was greater than equipment preventive cost. As a result, a major overhaul was selected for all the assets. But according to the equipment criticality, a major overhaul was selected for the overhead crane machine 500-ton press machine, and air compressor machine but FTM is selected for the VDF lathe machine and roller machine. As equipment criticality was less and the cost of fixed time maintenance was less, it was the best maintenance strategy for the VDF lathe machine and roller machine.

6 Results and Discussion

The lean tools were ranked based on descending importance rating derived from the combined QFD-AHP analysis which is represented in Fig. 4. The results of NHPP analysis and Weibull analysis are given in Table 6 and Table 7 respectively. The maintenance strategy of each machine is shown in Table 8.

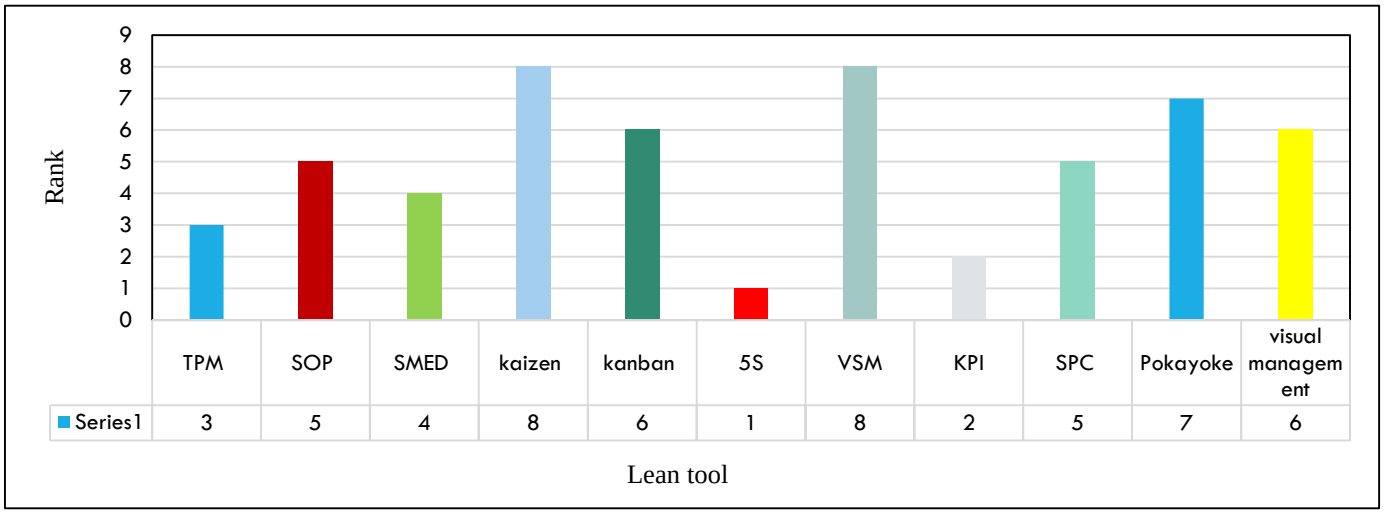

Fig. 4 Rank vs. Lean tool

Table 6 Results of the NHPP analysis

Machine no	Machine name	β	Prediction of next failure(day)	Time to failure (historical data)
1	Overhead crane machine	1.46	1210.17	1128
2	500-ton press machine	1.43	328.30	343
3	Air compressor machine	1.77	598.45	628
4	VDF lathe machine	1.59	588.32	615
5	Roller machine	1.194	638.95	740

Table 7 Results of the Weibull analysis

Machine no.	Machine name	β	λ/day	Reliability (%)
1	Overhead crane machine	1.35	0.012	41.1
2	500-ton press machine	1.21	0.039	35.8
3	Air compressor machine	1.39	0.020	36.81
4	VDF lathe machine	3.16	0.037	35.6
5	Roller machine	2.18	0.027	25.9

Table 8 Maintenance strategy of each machine

Machine name	MTBF(days)	MMTR(days)	Criticality score (%)	Maintenance strategy
Overhead crane machine	102.78	81.5	80	MOH
500-ton press machine	41.29	83.5	65	MOH
Air compressor machine	69.36	88.7	71.67	MOH
VDF lathe machine	86.23	60.5	33.33	FTM
Roller machine	81.27	50	33.33	FTM

Table 9 Importance of weighting of the ME

Importance weighting (c)	0.046	0.031	0.078	0.118	0.387	0.119	0.126	0.024	0.07

6.1 Discussion

The combined QFD –AHP was used to rank the lean maintenance tool. A survey was conducted based on ME. These survey results were used to compare the two ME and develop a pairwise comparison matrix. The important weighting of ME is listed in Table 9. Consistency ratio was calculated and from the Saaty table, m is equal to 11 for nine 9 ME criteria. The result of the consistency ratio is 0.023 which was less than 0.1. So, it was indicated that the result of the QFD –AHP approach was quite acceptable. The rank obtained from the QFD –AHP analysis shown in Fig. 4 will guide the way to which lean tool is useful for the shipyard and what tool was used to enhance the performance of the asset.

The historical failure date of the machine was collected from the maintenance logbook of the SIGMA shipyard. The machine was under a breakdown maintenance strategy and these machine data were collected from the logbook for analyzing the reliability study. The machines selected were the overhead crane machine, air compressor machine, 500-ton press machine, VDF lathe machine, and roller machine. After collecting the failure data, the time to failure was calculated. Then the cumulative time and cumulative MTBF were determined. Then NHPP modeling by Microsoft excel was used for calculating the slope (β) and failure rate (λ) of each machine. The instantaneous failure and the instantaneous failure rate were determined. The value of beta (β) and lambda (λ) from NHPP and Weibull analysis are listed in Table 6 and Table 7 respectively. Cumulative no of failure vs. cumulative failure time was plotted in Fig. 5. From this plotting, it could be easily shown that the failure rate was increasing. Moreover, it might be easily understood by the value of slope (β). The plot was drawn using historical data and predicted data for the next failure obtained from NHPP in Microsoft excel. Another plot was drawn by using the failure data of this machine. The amount of failure data was used for overhead crane m/c, 500-ton press machine, air compressor m/c, VDF lathe m/c, and roller m/c which were 11, 10, 9, 8, 10 accordingly. The result that got from the reliability model is correct or not, this may be verified by the historical data. The next failure event for the overhead crane machine was expected 1210 days later by the calculation of the historical data. In reality, the failure occurred 1128 days later which indicated that the error was minor. Whereas the value of β was larger than 1, which confirms that the failure rate of the machine was increasing.

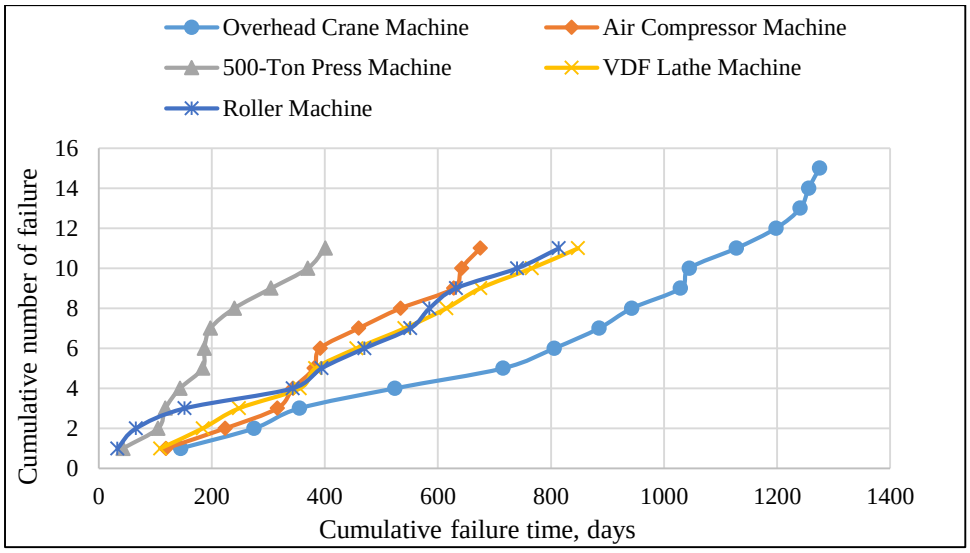

Fig. 5 Cumulative failure time vs. Cumulative no of failure

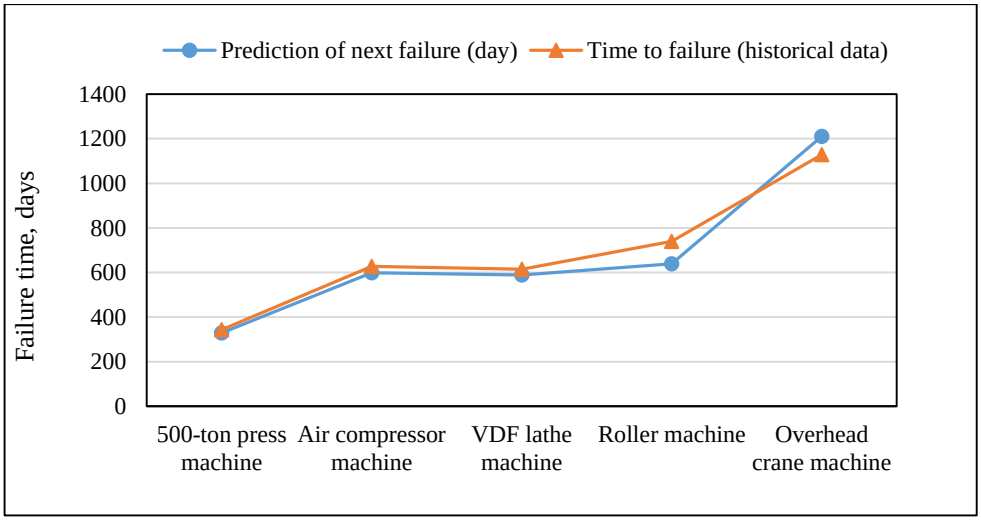

Fig. 6 Machine vs. predicted failure data

Another plot was drawn in Fig. 6 by using historical failure data and predicted failure data. If the prediction line is analyzed thoroughly in Fig. 6, it can be seen that the prediction data point were very close to the actual data points of the failure events. In the same way, the next failure air compressor machine was expected 598.45 days later and the actual failure happened 401 days later. Hence, the value of beta was larger than 1 so the rate of degradation was increased. The next failure events for the 500-ton lathe machine, VDF lathe machine, and roller machine were expected at 328, 588, and 638 days later accordingly and the actual time to failure of this machine was 343, 615, and 740 days later respectively. For the 500-ton press machine, the deviation between the prediction of failure and actual failure was more. This might be occurred due to missing data. Because the collected data of SIGMA shipyard are not computerized. This data was collected from the maintenance logbook so it was possible to miss out on recording any failure data. The graph shown in Fig. 7 was obtained using the "PTC Wind-chill Quality Solutions 11.0 Tryout" for an overhead crane. For Weibull results for the overhead crane machine shown in Fig. 7, the slope of the shape parameter is 1.35 which represents the wear-out hazard rate and it followed the Rayleigh distribution. Replacement of schedules would be effective for the overhead crane machine. The reliability curve decreases moderately and this assent was entering the wear-out phase. The variation of data was less as shown in the figure of the CDF plot so it asserts the low variation of the failure time. The characteristics of life and mean time to failure is 102.78 days.

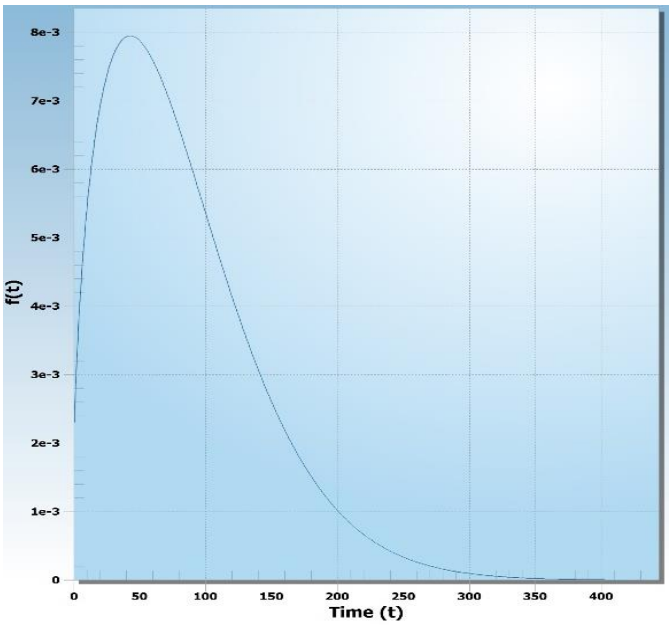

PDF vs Time

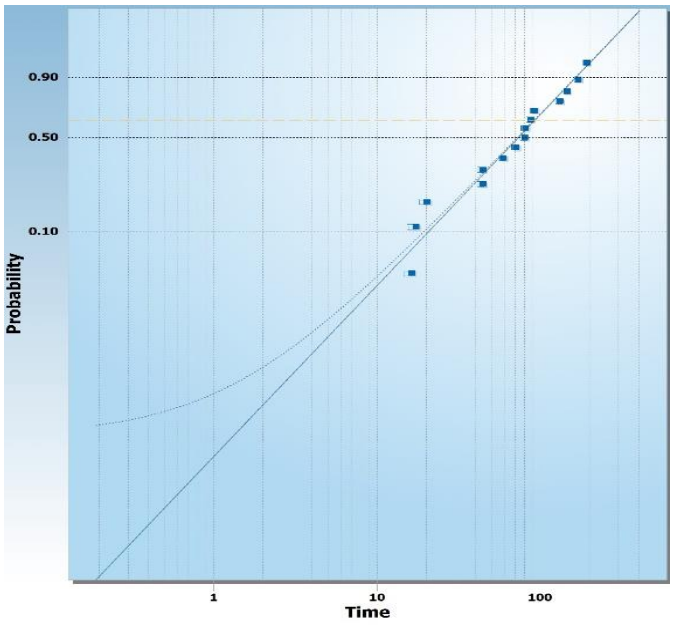

Probability vs Time

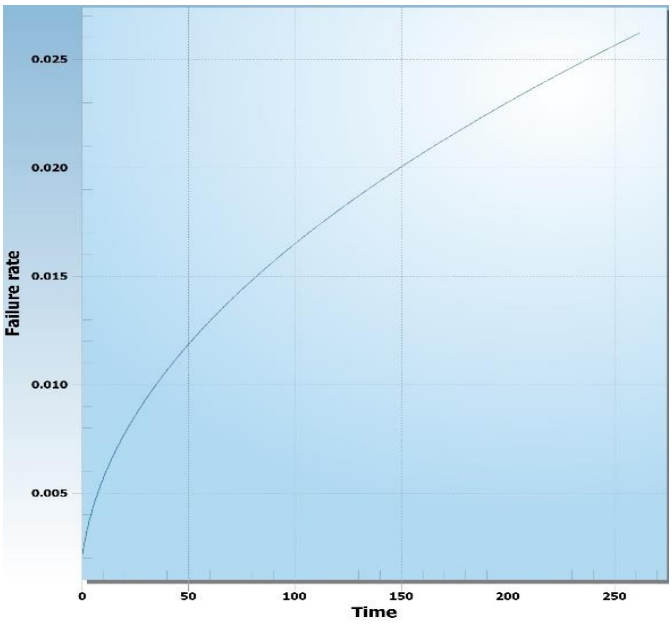

Failure Rate vs Time

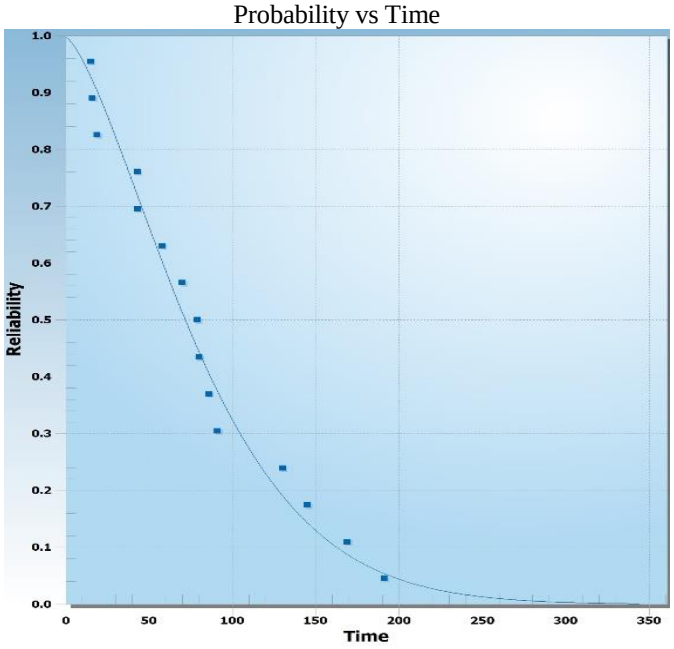

Reliability vs Time

Fig. 7 Weibull result for overhead crane machine (β = 1.4848; η = 93.4681; γ = -1.3293; ρ = 0.9762; ρ^2 = 0.9529).

Weibull results for the 500-ton press machine and air compressor machine are shown in Fig. B1 and Fig. B2 in Appendix B accordingly. The value of the slope was 1.21 and 1.39 respectively. As β>1, the hazard rate was increased and it followed the Rayleigh distribution also. From the CDF plot, it was concluded that the variation of failure time was more than

the overhead crane machine. The characteristics of the life of the machine were 41.29 and 69.36 days respectively. The percentage of failure at the end of the observation time is 64.2% and 63.9% accordingly.

Weibull results for the VDF machine are shown in Fig. B3 in Appendix B. The value of the slope is 3.16. As β>1, the hazard rate was increasing and the graph of the PDF looked like a normal distribution. The variation of data was moderate. The reliability with time was decreasing slowly. The mean lifetime of the machine and cumulative density function was 87.12 days and 64.4% accordingly.

Weibull results for the Roller machine are shown in Fig. B4 in Appendix B. The value of the slope was 2.18. As β>1, the hazard rate was increasing and the equipment's entered the early wear phase and the graph of the PDF followed the Rayleigh distribution. The failure data were more scattered than other equipment. The reliability with time was decreasing slowly. The mean lifetime of the machine was 82.16 days and the cumulative density function was 64.1%. The goodness of data fit was 89%.

Reliability parameter (β) from the Weibull analysis and availability and machine criticality were considered to select the appropriate maintenance strategy. Hence, the value of β obtained from the Weibull analysis was greater than 1 so it was high time to replace the old one with the new one. It was also considered that the cost for repair was greater than the equipment preventive cost. As a result, a major overhaul was selected for all the assets. But according to the equipment criticality, a major overhaul was selected for the overhead crane machine 500-ton press machine, and air compressor machine but FTM was selected for the VDF lathe machine and roller machine.

7 Conclusion

The implementation of lean tools and the selection of an effective maintenance strategy can make the maintenance function dynamic and effective. The study proposed appropriate lean tools to be implemented among ten (10) lean tools in the maintenance department of the SIGMA shipyard. 5S and KPI are the two lean tools having the maximum importance degree of 5.5 and 2.33 respectively. According to NHPP analysis and Weibull analyses, predicted next failure events (11th) were estimated after 76.16 days, 23.30 days, 38.45 days, 47.32 days, and 53.95 days respectively and the failure rate (β) was 1.35, 1.21, 1.39, 3.16, and 2.81 for Overhead crane machine, 500-ton press machine, Air compressor machine, VDF lathe machine, Roller machine accordingly. Based on the reliability analysis, a major overhaul was selected for the overhead crane machine 500-ton press machine, and air compressor machine. As equipment criticality and the cost of fixed maintenance were less, FTM was the best maintenance strategy for the VDF lathe machine and roller machine. The method employed in the study was used as a generalized method for various forms of repairable assets. The QFD-AHP approach employed in this study helps maintenance practitioners to prioritize the lean tool to achieve lean maintenance. NHPP modeling created by using excel can be used as a template for identifying upcoming failure events. A decision diagram is applied for choosing the best strategy that may be used as a decision model for any repairable asset. The decision conceptual model might be improved by adding maintenance costs. Reliability analysis can be investigated for the entire maintenance department as a whole.

References

[1] Tendayi, T.G., 2013. *An investigation into the applicability of lean thinking in an operational maintenance environment* (Doctoral dissertation, Stellenbosch: Stellenbosch University).

[2] Chuang, P.T., 2001. Combining the analytic hierarchy process and quality function deployment for a location decision from a requirement perspective. *The International Journal of Advanced Manufacturing Technology*, *18*(11), pp.842-849.

[3] Barabady, J., 2005. *Improvement of system availability using reliability and maintainability analysis* (Doctoral dissertation, Luleå tekniska universitet).

[4] Ruan, A. and Shangguan, J., 2010, August. Study on a new approach of rank preservation in Analytic Hierarchy Process. In *2010 International Conference on Intelligent Control and Information Processing* (pp. 73-77). IEEE.

[5] Mostafa, S., Dumrak, J. and Soltan, H., 2015. Lean maintenance roadmap. *Procedia Manufacturing*, *2*, pp.434-444.

[6] Duran, O., Capaldo, A., & Acevedo, P. A. D. (2017). Lean maintenance applied to improve maintenance efficiency in thermoelectric power plants. *Energies*, *10*(10), 1–21.

[7] Irajpour, A., Fallahian-Najafabadi, A., Mahbod, M.A. and Karimi, M., 2014. A framework to determine the effectiveness of maintenance strategies lean thinking approach. *Mathematical Problems in Engineering*, *2014*.

[8] Zarei, M., Fakhrzad, M.B. and Paghaleh, M.J., 2011. Food supply chain leanness using a developed QFD model. *Journal of food engineering*, *102*(1), pp.25-33.

[9] Vaidya, O.S. and Kumar, S., 2006. Analytic hierarchy process: An overview of applications. *European Journal of operational research*, *169*(1), pp.1-29.

[10] Partovi, F.Y., 2006. An analytic model for locating facilities strategically. *Omega*, *34*(1), pp.41-55.

[11] Ho, W., 2008. Integrated analytic hierarchy process and its applications–A literature review. *European Journal of Operational Research*, *186*(1), pp.211-228.

[12] Tang, Z., Zhou, W., Zhao, J., Wang, D., Zhang, L., Liu, H., Yang, Y. and Zhou, C., 2015. Comparison of the Weibull and the crow-AMSAA model in prediction of early cable joint failures. *IEEE Transactions on Power Delivery*, *30*(6), pp.2410-2418.

[13] Muhammad, M.B., Raza, T. and Abd Majid, M.A., 2016. Prediction Of Failures By Using Crow/AMSAA Model In Microsoft Excel.

[14] Tang, Z., Zhou, W., Zhao, J., Wang, D., Zhang, L., Liu, H., Yang, Y. and Zhou, C., 2015. Comparison of the Weibull and the crow-AMSAA model in prediction of early cable joint failures. *IEEE Transactions on Power Delivery*, *30*(6), pp.2410-2418.

[15] Afzali, P., Keynia, F. and Rashidinejad, M., 2019. A new model for reliability-centered maintenance prioritisation of distribution feeders. *Energy*, *171*, pp.701-709.

[16] Hemmati, N., Galankashi, M.R., Imani, D.M. and Farughi, H., 2018. Maintenance policy selection: a fuzzy-ANP approach. *Journal of Manufacturing Technology Management*.

Appendix A

Maintenance excellence criteria survey for AHP Analysis

1. Spare parts availability:

Are the materials and parts ordered and delivered on time so as to avoid stock out during planned outs and during planned maintenance activities and emergency breakdowns?

2. Key performance indicator:

Do all key performance processes have KPIs and are these KPIs regularly reviewed for decision-making process?

3. Policy and strategy:

Are the current maintenance policies and strategies are well understood by all maintenance workers?

4. Comprehensive work order:

Are work orders and job cards containing clear comments that can be used for future reference?

5. Organization cleaning, tiding of work areas:

To what extent is the organization in ongoing efforts for cleaning and tiding work areas?

6. Reduction in intervention number:

To what extent is the organization engaged in ongoing effort to reduce breakdown of a machine?

6. Reduction in process variability:

To what extent are the current SAP systems helping the organization do its work more effectively?

7. Preventive maintenance implemented in the organization:

Is maintenance work generally complemented according to schedule?

8. Continuous monitoring of procedure and increasing efficiency:

To what extent is the organization engaged in ongoing effort to improve maintenance efficiency?

Five options for each questionnaire

- Excellent
- Good
- Average
- Poor
- Bad

Appendix B

Table B1 Data required for reliability analysis

Equipment no.	Equipment name	Failure date	Repair time (months)	Failure date	Repair time (months)
1.	Overhead crane machine	24.9.14	6	15.10.17	7
		02.05.15	7	1.11.17	3
		12.8.15	8.5	3.8.18	5
		02.11.15	8	24.3.18	6
		17.02.16	6	4.5.18	3
		21.05.16	5	17.5.18	4
		02.12.16	5	2.5.18	4
		03.02.17	4	12.6.18	4
		19.7.17	4		
2	500 ton press machine	30.1.17	7	14.08.17	5
		13.3.17	2	13.10.17	4
		11.5.17	12	5.12.17	8
		24.5.17	7	13.3.18	4
		20.6.17	5	15.4.18	5
		30.7.17	3	16.5.18	3
		03.08.17	6		
3	Air compressor machine	25.04.16	8.5	18.7.17	6
		24.10.16	8.5	06.10.17	8.2
		11.02.17	8.5	20.12.17	8.5
		13.05.17	16	24.03.18	8.5
		11.06.17	4	07.0618	6
		17.7.17	6	10.07.18	8.5
5	VDF lathe machine	29.02.16	5	25.04.17	4
		18.06.16	4	19.07.17	5.5
		03.08.16	6	3.10.17	7
		07.10.16	7	3.1.18	6
		15.01.17	4	4.4.18	6
		12.02.17	6	26.6.18	4
6	Roller machine	25.3.16	3	24.03.17	6
		28.04.16	4.5	15.06.17	3
		11.06.16	6	19.07.17	4.5
		07.09.16	6	05.09.17	3
		18.11.16	4.5	23.12.17	4.50
		08.01.17	5	07.03.18	4.50

Table B2 Data input section and result table for an air compressor machine

Air Compressor Machine								
Result Section			**Data Input Section**					
Input data			No of failures	Time between failure	Cum. Failure time	Cum. MTBF	ln (Cum. Failure Time)	MTTR
No. of failure (n)		8	1	119	119	119.00	4.78	8.5
End of observation time (T)		560 days	2	105	224	112.00	5.41	8.5
Availability		0.8839	3	92	316	105.33	5.76	16.0
Sum ln(Cum. failure time)		46.11	4	28	344	86.00	5.84	4.0
Estimated parameters			5	37	381	76.00	5.94	6.0
Slope (β)		1.77	6	11	392	65.33	5.97	6.0
Lamda (λ)		0.000107/day	7	68	460	65.71	6.13	8.2
Calculations			8	74	534	66.75	6.28	8.5
Failure rate (instantaneous)	1200 days	0.0267	9	94	628	69.78	6.44	8.5
Instantaneous MTBF, 1/u(t)		37.42	10	14	642	64.20	6.46	6.0
Cumulative failure N (t)	1200 days	9.041	11	33	675	61.36	6.71	8.5
Cum. failure rate		0.0151				**Sum**	65.53	88.7
Cum MTBF		66.362						
Prediction to next failure								
Next failure occurrence (t)	n=11	598.45 days						
Time to next failure (t)		38.45 days						

Table B3 Data input section and result table for 500-ton press machine

500-Ton Press Machine								
Result Section			**Data Input Section**					
Input data			No of failures	Time between failure	Cum. Failure time	Cum. MTBF	ln (Cum. Failure Time)	MTTR
No. of failure (n)		9	1	43.00	43.00	43.00	3.76	7.00
End of observation time (T)		305 days	2	62.00	105.00	52.50	4.65	2.00
Availability		0.8188687	3	13.00	118.00	39.33	4.77	12.00
Sum ln(Cum. failure time)		45.19	4	26.00	144.00	36.00	4.97	7.00
Estimated parameters			5	40.00	184.00	36.80	5.21	5.00
Slope (β)		1.431036	6	3.00	187.00	31.17	5.23	3.00
Lamda (λ)		0.0025/day	7	11.00	198.00	28.29	5.29	6.00
Calculations			8	42.00	240.00	30.00	5.48	5.00
Failure rate (instantaneous)	1200 days	0.0522545	9	65.00	305.00	33.89	5.72	4.00
Instantaneous MTBF, 1/u(t)		19.137111	10	65.00	370.00	37.00	5.91	8.00
Cumulative failure N (t)	1200 days	18.257578	11	31.00	401.00	36.45	5.99	4.00
Cum. failure rate		0.0365152				**Sum**	57.00	63.00
Cum MTBF		27.385888						
Prediction to next failure								
Next failure occurrence (t)	n=11	328.30 days						
Time to next failure (t)		23.30 days						

Table B4 Data input section and result table for VDF lathe machine

VDF Lathe Machine								
Result Section			**Data Input Section**					
Input data			No of failures	Time between failure	Cum. Failure time	Cum MTBF	ln (Cum. Failure Time)	MTTR
No. of failure (n)		7	1	109.00	109.00	109.00	4.69	5.00
End of observation time (T)		541 days	2	75.00	184.00	92.00	5.21	4.00
Availability		0.9334067	3	64.00	248.00	82.67	5.51	6.00
Sum ln(Cum. failure time)		39.66	4	108.00	356.00	89.00	5.87	7.00
Estimated parameters			5	27.00	383.00	76.60	5.95	4.00
Slope (β)		1.59	6	73.00	456.00	76.00	6.12	6.00
Lamda (λ)		0.00031/day	7	85.00	541.00	77.29	6.29	4.00
Calculations			8	74.00	615.00	76.88	6.42	5.50
Failure rate (instantaneous)	1200 days	0.0219	9	60.00	675.00	75.00	6.51	7.00
Instantaneous MTBF, 1/u(t)		45.64	10	91.00	766.00	76.60	6.64	6.00
Cumulative failure N (t)	1200 days	8.255	11	82.00	848.00	77.09	6.74	6.00
Cum. failure rate		0.0138			**Sum**		65.98	60.50
Cum MTBF		72.688						
Prediction to next failure								
Next failure occurrence (t)	n=11	588.32 days						
Time to next failure (t)		47.32 days						

Table B5 Data input section and result table for roller machine

Roller Machine								
Result Section			**Data Input Section**					
Input data			No of failures	Time between failure	Cum. Failure time	Cum MTBF	ln (Cum. Failure Time)	MTTR
No. of failure (n)		8	1	33.00	33.00	33.00	3.50	3.00
End of observation time (T)		585 days	2	33.00	66.00	33.00	4.19	4.50
Availability		0.9421296	3	86.00	152.00	50.67	5.02	6.00
Sum ln(Cum. failure time)		49.81	4	191.00	343.00	85.75	5.84	6.00
Estimated parameters			5	51.00	394.00	78.80	5.98	4.50
Slope (β)		1.19436	6	76.00	470.00	78.33	6.15	5.00
Lamda (λ)		0.004459/day	7	81.00	551.00	78.71	6.31	6.00
Calculations			8	34.00	585.00	73.13	6.37	3.00
Failure rate (instantaneous)	1200 days	0.0195273	9	47.00	632.00	70.22	6.45	4.50
Instantaneous MTBF, 1/u(t)		51.210349	10	108.00	740.00	74.00	6.61	3.00
Cumulative failure N (t),	1200 days	13.079672	11	74.00	814.00	74.00	6.70	4.50
Cum. failure rate		0.0163496				**Sum**	63.12	50.00
Cum MTBF		61.163614						
Prediction to next failure								
Next failure occurrence (t)	n=11	638.95 days						
Time to next failure (t)		53.95days						

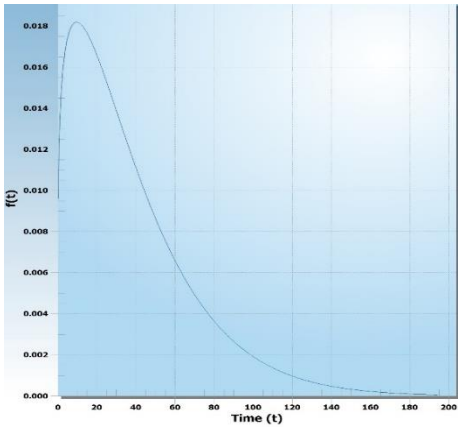

PDF vs Time

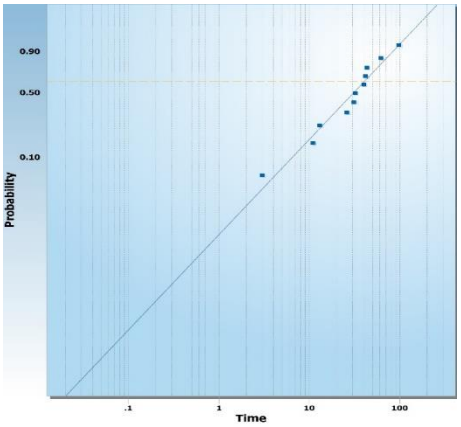

Probability vs Time

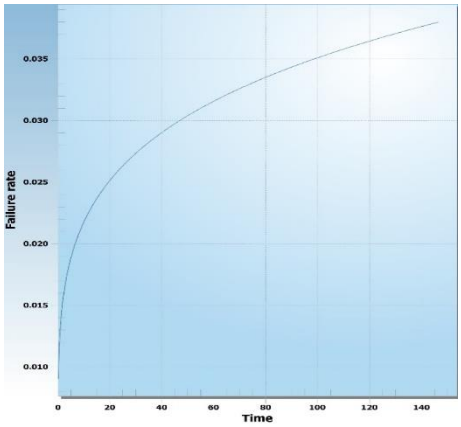

Failure Rate vs Time

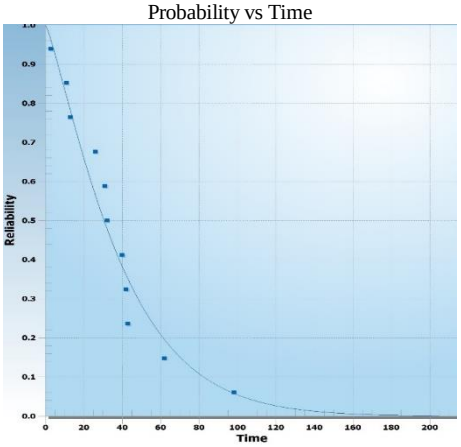

Reliability vs Time

Fig. B1 Weibull result for 500-ton press machine (β = 1.2072; η = 41.2906; ρ = 0.9774; ρ^2 = 0.9552).

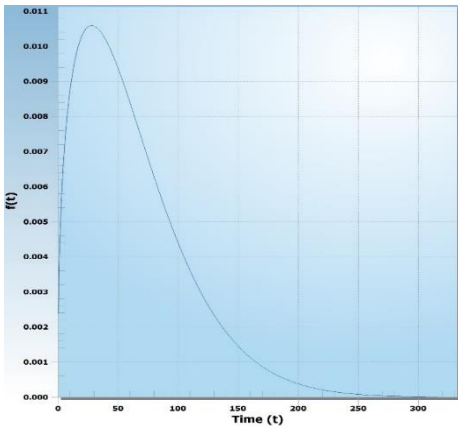

PDF vs Time

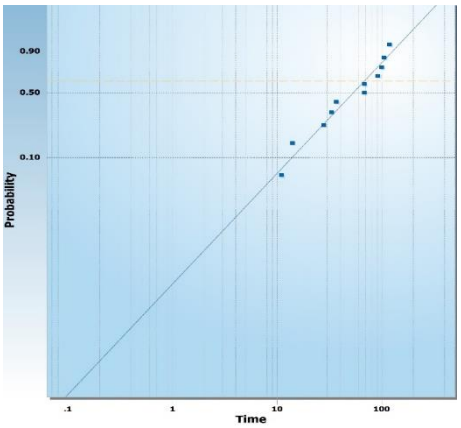

Probability vs Time

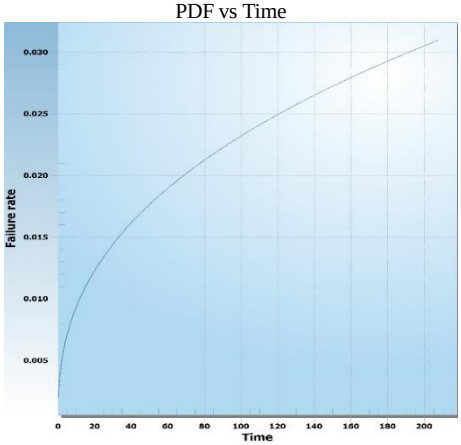

Failure Rate vs Time

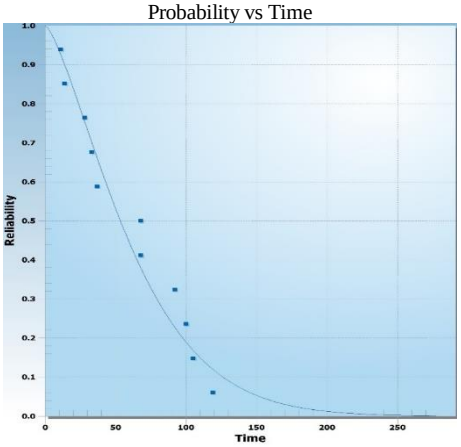

Reliability vs Time

Fig. B2 Weibull result for an air compressor machine (β = 1.3949; η = 69.3860; ρ = 0.9784; ρ^2 = 0.9572).

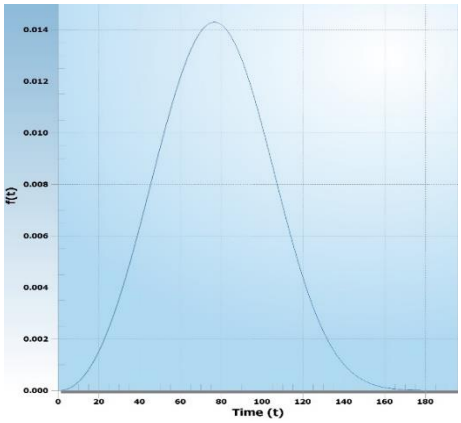

PDF vs Time

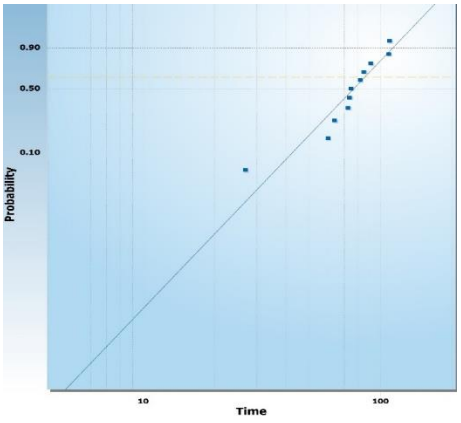

Probability vs Time

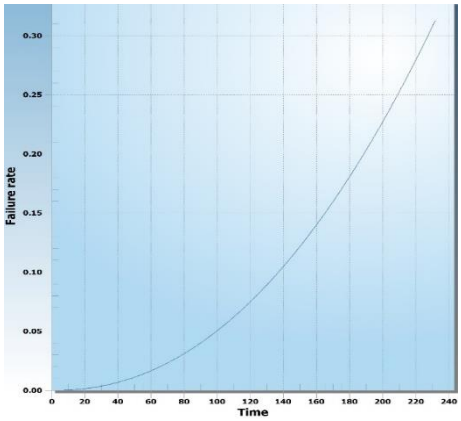

Failure Rate vs Time

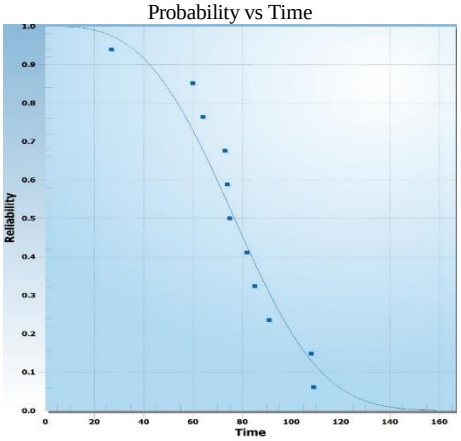

Reliability vs Time

Fig. B3 Weibull result for VDF machine ($\beta = 3.1679$; $\eta = 86.2276$; $\rho = 0.9363$; $\rho^2 = 0.8767$).

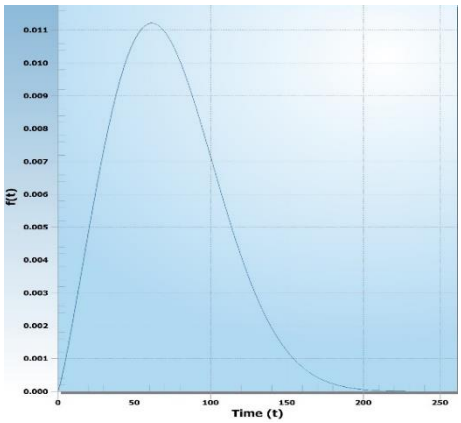

PDF vs Time

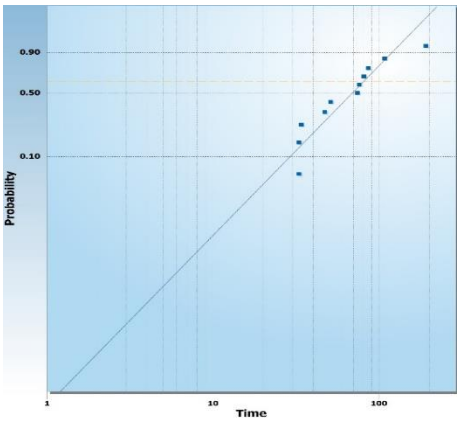

Probability vs Time

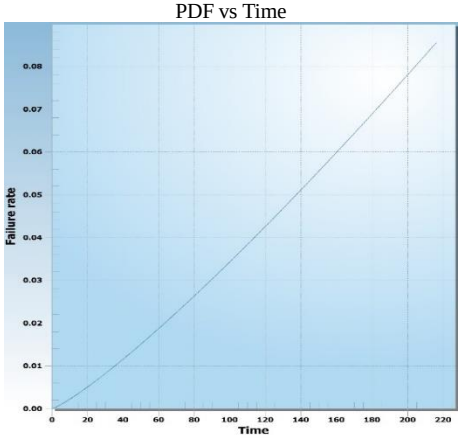

Failure Rate vs Time

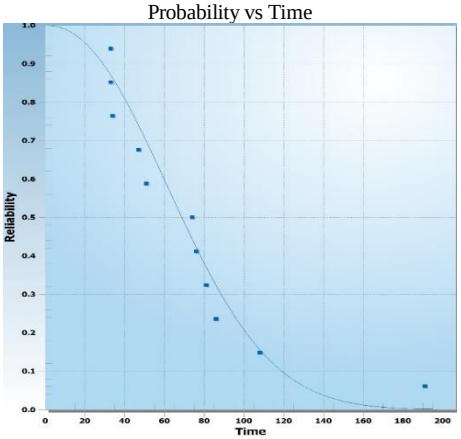

Reliability vs Time

Fig. B4 Weibull result for Roller machine ($\beta = 2.1850$; $\eta = 81.2703$; $\rho = 0.9289$; $\rho^2 = 0.8628$).

Appendix C

Table C1 Abbreviation of ME

SP	Spare sparts and material availability
KPI	Key performance indicators
PS	Policy and strategy
CWO	Comprehensive work order
OCT	Organization cleaning and tiding of work areas
RIN	Reduction in intervention number
RPV	Reduction in process variability
PM	Preventive maintenance
CMPANDIE	Continuous monitoring of procedure and increasing efficiency

Table C2 Pairwise Comparison matrix developed by experts

	SP	KPI	PS	CWO	OCT	RIN	RPV	PM	CMPANDIE
SP	1	1/3	1/3	1	1/7	1	1	3	1
KPI	3	1	1	1/3	1/7	1/3	1/3	3	1/3
PS	3	1	1	1/3	1/7	1/3	1/3	3	3
CWO	1	3	3	1	1/3	1	1	3	1
OCT	7	7	7	3	1	5	3	7	3
RIN	1	3	3	1	1/5	1	1	5	1
RPV	1	3	3	1	1/3	1	1	5	1
PM	1/3	1/3	1/3	1/3	1/7	1/5	1/5	1	1/5
CMPANDIE	1	3	1/3	1	1/3	1	1	5	1

Table C3 Fuzzification matrix

	SPMA			KPI				PS			CWO				OCT			RIN			RPV			PM			CMPANDIE		
	L	M	U	L	M	U	L	M	U	L	M	U	L	M	U	L	M	U	L	M	U	L	M	U	L	M	U	L	M	U
SP	1	1	1	1/5	1/3	1/2	1	1/3	1	1	1	1	1/8	1/7	1/6	1	1	1	1	1	1	2	3	4	1	1	1			
KPI	2	3	4	1	1	1	1	1	1	1/5	1/3	1/2	1/8	1/7	1/6	1/5	1/3	1/2	1/5	1/3	1/2	2	3	4		1/3				
PS	2	3	4	1	1	1	1	1	1	1/5	1/3	1/2	1/8	1/7	1/6	1/5	1/3	1/2	1/5	1/3	1/2	2	3	4	2	3	4			
CWO	1	1	1	2	3	4	2	3	4	1	1	1	1/5	1/3	1/2	1	1	1	1	1	1	2	3	4		1				
OCT	6	7	8	6	7	8	6	7	8	2	3	4	1	1	1	4	5	6	2	3	4	6	7	8	2	3	4			
RIN	1	1	1	2	3	4	2	3	4	1	1	1	1/6	1/5	1/4	1	1	1	1	1	1	4	5	6	1	1	1			
RPV	1	1	1	2	3	4	2	3	4	1	1	1	1/5	1/3	1/4	1	1	1	1	1	1	4	5	6	1	1	1			
PM	1/5	1/3	1/2	1/5	1/3	1/2	1/5	1/3	1/2	1/5	1/3	1/2	1/6	1/7	1/4	1/6	1/5	1/4	1/6	1/5	1/7	1	1	1		1/5				
CMPANDIE	1	1	1	2	3	4		1/3		1	1	1	1/5	1/3	1/2	1	1	1	1	1	1	4	5	6	1	1	1			
	15.20	18.33	21.50	16.40	21.67	27.00	15.20	19.00	23.50	7.60	9.00	10.50	2.31	2.77	3.25	9.57	10.87	12.25	7.57	8.87	10.14	27.00	35.00	43.00	8.00	11.53	12.00			

Table C4 Geometric Mean Value of Each ME

	Geometric mean value		
	Lower value	Middle value	Upper value
SPMA	0.526	0.557	0.65
KPI	0.5	0.63	0.88
PS	0.629	0.885	1.032
CWO	1.08	1.27	1.46
OCT	3.25	4.01	4.88
RIN	1.11	1.27	1.42
RPV	1.16	1.35	1.53
PM	0.23	0.28	0.37
CMPANDIE	0.65	0.74	0.45
TOTAL	**9.135**	**10.992**	**12.672**
INVERSE	**0.077**	**0.09**	**0.1094**

Table C5 Weight of Each ME

	Weight of each value		
	Lower value	Middle value	Upper value
SPMA	0.04	0.05	0.07
KPI	0.0385	0.0567	0.096
PS	0.0484	0.072	0.112
CWO	0.083	0.114	0.1531
OCT	0.25	0.3601	0.5338
RIN	0.085	0.1143	0.1553
RPV	0.089	0.1215	0.1673
PM	0.018	0.0252	0.029
CMPANDIE	0.05005	0.0666	0.092

Table C6 Normalized Weight of Each ME

	Defuzzied weight	Normalized weight
SPMA	0.05	0.050
KPI	0.031	0.031
PS	0.077	0.077
CWO	0.1167	0.117
OCT	0.3839	0.386
RIN	0.1182	0.119
RPV	0.125	0.126
PM	0.024	0.024
CMPANDIE	0.0693	0.070
Total	0.9951	1.000

This page is left intentionally blank

Journal of Engineering Advancements (JEA)

DOI: https://doi.org/10.38032/jea

Indexed by:

Google Scholar Crossref

Scilit

Volume 03 Issue 03

DOI: https://doi.org/10.38032/jea.2022.03

Published by: SciEn Publishing Group

Website: www.scienpg.com